Improving the Capabilities of Therapeutic Ultrasound in the Brain

By

Thomas Joseph Manuel

Dissertation

Submitted to the Faculty of the

Graduate School of Vanderbilt University

in partial fulfillment of the requirements

for the degree of

DOCTOR OF PHILOSOPHY

In

Biomedical Engineering

May 12th, 2023

Nashville, Tennessee

Approved:

Charles F. Caskey, Ph.D.

Li Min Chen, Ph.D.

John C. Gore, Ph.D.

William Grissom, Ph.D.

Brett Byram, Ph.D.

To Joseph Otto Manuel, Jr.

ACKNOWLEDGMENTS

I would like to thank my advisor, Charles F. Caskey, for granting me the opportunity to work under his mentorship and especially for believing in me after my challenging first year at Vanderbilt. Working for you has been a tremendous learning experience and a pleasure. I would like to thank my wife, Kelli Manuel, for loving support throughout my time in graduate school. I would like to thank my parents, Tom and Phyllis Manuel, for being the best parents one could hope for. I would like to thank my talented and friendly labmates Tony Phipps, Jiro Kusunose, Michelle Sigona, Aparna Singh, Adrienne Hawkes, Malachy Newman, Andy Xia, and Allie Dockum for making the lab culture relaxing and enjoyable. I would like to thank Pai-Feng Yang, Chaohui Tang, Jamie Reed, Allen Newton, and Li Min Chen for making the blood-brain barrier opening experiments possible. I would like to thank John Gore and the Vanderbilt University Institute of Imaging Science for gathering such a powerful and diverse assembly of scientists and tools which made my research projects possible. Lastly, I would like to acknowledge the grants S10ODO21771-01 and UG3-MH120102 (NIH) for funding this work.

LIST OF TABLES

LIST OF FIGURES

TABLE OF CONTENTS

Chapter 1

1.1 Synopsis

There are two primary reasons for developing tools which non-invasively manipulate brain tissue: probing of neurologic processes and treatment of brain related disorders. Currently, several tools are available to neuroscientists for probing neurological processes. Microstimulation, optogenetics, and injection of pharmacologic agents provide neural manipulation with high spatial precision. While unmatched in precision, each of these requires either brain surgery or genetic manipulation and are limited in application by their invasiveness (Terranova et al. 2019). Non-invasive brain stimulation techniques are being developed with the aim of probing neurological processes without invasive procedures. Transcranial electric stimulation (TES) delivers weak currents into the brain through electrodes coupled to the scalp. This is non-invasive and directly modulates neural activity through electro-chemical coupling but has low spatial precision and penetration depth (Faria, Hallett, and Miranda 2011). Transcranial magnetic stimulation (TMS) uses magnetic coils to produce electric currents inside the brain via electromagnetic induction (Walsh and Cowey 2000). TMS improves upon the spatial precision of TES and can target volumes on the order of several cm^3, but this is limited to cortical targets and is still greater than functional brain target sizes. The limitations of the available tools highlight a need for a non-invasive brain stimulation techniques with high spatial precision.

The second motivating factor behind developing brain therapy tools is for the treatment of brain related disorders. Depression, chronic pain, and addiction may affect a combined 40% of the adult population in the United States (Volkow, Benveniste, and McLellan 2018; Brody, Pratt, and Hughes 2018). Although staggering in number, treatment options for these diseases are largely limited to oral drugs which have limited efficacy and risks of addiction and toxicity. The effectiveness of available treatments is limited in

part by difficulty accessing brain regions without prohibitively invasive surgical procedures as well as the blood-brain barrier which restricts drug delivery into the brain for all but a small subset of candidate drugs. Brain surgery is used routinely for glioblastoma, Parkinson's disease, and other disorders with life-threatening or severely debilitating symptoms because the trade-off between procedural risk and invasiveness is outweighed by the gain of patient outcome. However, with depression, addiction, and a subset of chronic pain patients, the debilitation is not sufficient to warrant brain surgery. Systemically administered drugs are an obvious alternative, but only small molecule lipophilic drugs can reach brain tissue at relevant doses due to the blood-brain barrier (Pardridge 2005). Advanced drugs which leverage molecular transport phenomena or nanoparticle vehicles to cross the blood-brain barrier are being explored but have yet to reach clinical adoption. Non-invasive tools which can safely manipulate brain tissue either by directly modulating neurons or by increasing drug delivery to the brain with high spatial precision will be key to improving patient outcomes in these disorders. Therapeutic ultrasound provides both capabilities.

The overall goal of the work described in this dissertation is to improve the capabilities of therapeutic ultrasound in the brain with specific focus on neuromodulation and drug-delivery applications. Low intensity ultrasound has modulatory effects on neurons and neural circuits. Moreover, ultrasound can be focused to spot sizes smaller than 1 cm^3 through the skull, a dramatic improvement on TES and TMS spatial capabilities. As the neuroscience surrounding depression, chronic pain, and addiction is better understood and the link between ultrasound and neuromodulation is strengthened by mechanistic insight, therapeutic ultrasound may emerge as a low cost, low intervention threshold (i.e. level of debilitation required to warrant a procedure) option to accompany or replace existing pharmacological treatments. Chapter 3 of this dissertation, *Ultrasound neuromodulation depends on pulse repetition frequency and can modulate inhibitory effects of tetrodotoxin*, focuses on the mechanisms of ultrasound neuromodulation and the relationship between parameters and outcomes. We developed a mouse brain slice model with neurons fluorescently labeled by calcium indicators and subjected it to ultrasound while monitoring with a fluorescent confocal microscope. This model provided a means for investigating the effectiveness of

different ultrasound parameters as well as the effect of introducing several concentrations of tetrodotoxin, a Na^{2+} channel blocker. This work was published in *Scientific Reports*.

Low intensity pulsed ultrasound in combination with circulating microbubbles can temporarily increase the permeability of the BBB. This expands the size and chemical makeup of drug options which can reach the brain parenchyma at relevant doses. This approach has been most broadly adopted in conjunction with tumor resection procedures for glioblastoma (Carpentier et al. 2016). In these clinical trials, ultrasound is used repeatedly to open the blood-brain barrier following tumor resection to increase the concentration of an agent (typically chemotherapeutic) around the tumor resection margin. However, a fundamental limitation of this approach is that the procedure must be repeated for each drug administration, which is made even more burdensome by the need for magnetic resonance imaging (MRI) guidance and evaluation in most cases. For this reason, researchers are exploring ways to either perform the procedures without MRI guidance or in a manner which has a permanent effect.

One way to leverage ultrasound BBB opening in a permanent manor is to deliver gene-therapy agents through the permeabilized zone. With gene-therapy, the affected neurons are permanently modified to transcribe artificially encoded proteins. The encoded proteomic shift can result in a permanent effect on the neurons or an effect which can be switched on an off by an orally administered compound (Szablowski et al. 2018). The work in chapters 4 and 5 enables this approach by designing and validating a transducer for BBB opening for gene therapy in non-human primates. A key feature of these efforts is to limit the size of BBB opening to improve the spatial specificity of the gene therapy. In Chapter 4, *Design of a 1-MHz therapeutic ultrasound array for small volume blood-brain barrier opening at cortical targets in macaques*, we design an array transducer for this purpose. The design leverages transcranial simulations to guide transducer feature selection. Our simulations revealed unexpected benefits with inward steering for transcranial focusing to cortical targets. This work also describes the calibration of the array and its integration into an MRI guided and optically tracked workflow. The design process developed in this work

takes advantages of recent advancements in GPU capabilities and advanced acoustic simulation techniques to fully incorporate information from transcranial simulations in four subjects and a large set of transducer models. This work is under review *IEEE Transactions on Ultrasonics, Ferroelectrics, and Frequency Control.*

In chapter 5, *Small volume blood-brain barrier opening in macaques with a 1 MHz phased array*, we test the array and guidance system in *in vivo* procedures in non-human primates. We use MRI to evaluate the BBB opening performance and provide safety measurements. We also develop and test a cavitation monitoring system for real-time pressure feedback in phantoms and evaluate its performance *in vivo.* This effort takes full advantage of the excellent staff and facilities at the Vanderbilt University Institute of Imaging Science (VUIIS) to develop and evaluate a state-of-the-art BBB opening system. This system will be deployed in the future for gene therapy in non-human primates.

These efforts constitute a push on multiple fronts to improve the capabilities of therapeutic ultrasound in the brain. We focus specifically on low intensity therapeutic ultrasound for neuromodulation and gene-therapy which have potential for treating depression, chronic pain, and addiction with minimally invasive, non-destructive procedures. In these efforts, we strengthened the link between mechanism and outcome for ultrasound neuromodulation. We also designed and validated a system for small volume blood-brain barrier opening which enables precise, non-invasive, transcranial gene-therapy in non-human primates. This transducer could also be used for precise neuromodulation.

Chapter 2

Overview of Focused Ultrasound

2.1 Physical Basics

2.1.1 Propagation through tissue

2.1.1.1 Basics of ultrasound waves

Sound above the audible range of humans (20 kHz) is referred to as ultrasound. Ultrasound exists as a pressure wave traveling through a medium, typically generated by applying a time varying voltage across a piezoelectric crystal. Particles in the medium are subject to oscillating displacement along the direction of the wave's travel. The dynamic and balanced interplay of displacement and pressure give rises to the wave nature of sound. This interplay can be described as a series of coupled, first-order differential equations governing momentum conservation, mass conservation, and a pressure-density relation:

$$\frac{\partial \boldsymbol{u}}{\partial t} = -\frac{1}{\rho_0}\nabla p \tag{2.1}$$

$$\frac{\partial \rho}{\partial t} = -\rho_0 \nabla \cdot \boldsymbol{u} \tag{2.2}$$

$$p = c_0^2 \rho \tag{2.3}$$

where **u** is the acoustic particle velocity, p is scalar pressure deviation from ambient pressure, c_0 is the speed of sound, t is time, ρ is the density, and ρ_0 is the equilibrium density (Pierce and Beyer 1990). These can also be combined into the classic second order wave equation:

$$\nabla^2 p - \frac{1}{c_0^2}\frac{\partial^2 p}{\partial t^2} = 0 \tag{2.4}$$

This equation shares form with that governing electromagnetic waves, and indeed properties of light like reflection, scattering, refraction, and aberration are also shared by sound waves. In one spatial dimension the equation reduces to:

$$\frac{\partial^2 p}{\partial x^2} - \frac{1}{c_0^2}\frac{\partial^2 p}{\partial t^2} = 0 \tag{2.5}$$

By leveraging these phenomena, we can understand and control ultrasound's interaction with tissue.

2.1.1.2 Sound transmission at an interface

In fluids, ultrasound propagates as a longitudinal wave producing sinusoidal displacement oscillations in the wave propagation direction which in turn yield pressure oscillations. A solution to equation 2.5 describes the pressure oscillations:

$$p(x,t) = A\cos(kx - \omega t) \tag{2.6}$$

where A is the pressure amplitude, x is distance, k is the wave number ($k = \frac{2\pi}{\lambda}$) where λ is the wavelength), and ω is the angular frequency ($\omega = 2\pi f$ where f in the frequency in Hz) (Szabo 2004). Positive pressure changes are compressional while negative changes are rarefactional.

All materials have an acoustic impedance (Z) given by:

$$Z = \rho c = \frac{p}{u} = \sqrt{B\rho} \tag{2.7}$$

Where Z has units of Rayl (1 Rayl = 1 $\frac{kg}{m^2 \cdot s}$), and B is the bulk modulus. Acoustic impedance governs the behaviors of sound at the boundary of two materials specifically through reflection, transmission, and refraction. The relative proportion of energy reflected at the boundary of two materials with impedances Z_1 and Z_2 is given by the reflection coefficient (R):

$$R = \frac{Z_2 - Z_1}{Z_2 + Z_1} \tag{2.8}$$

This is illustrated in figure 2.1 which shows the relationship between the incident wave amplitude and the amplitudes of the transmitted and reflected waves.

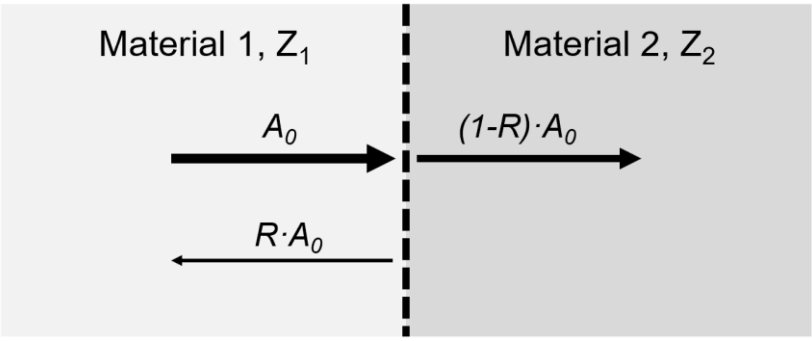

Fig. 2.1 Illustration of normal incidence reflection. A_0: amplitude of incident wave. R: reflection coefficient (eq. 2.8).

The reflection coefficient can be extended for non-normal incidence cases arriving with an angle, θ_i, relative to the surface normal:

$$R = \frac{Z_2 \cos\theta_i - Z_1 cos\theta_t}{Z_2 \cos\theta_i + Z_1 cos\theta_t} \tag{2.9}$$

Where θ_i and θ_t represent the incident and transmitted angle respectively. Transmitted angle can be computed given incident angle according to Snell's law given the speed of sound of the two materials, c_1 and c_2:

$$\frac{\sin\theta_i}{c_1} = \frac{\sin\theta_t}{c_2} \tag{2.10}$$

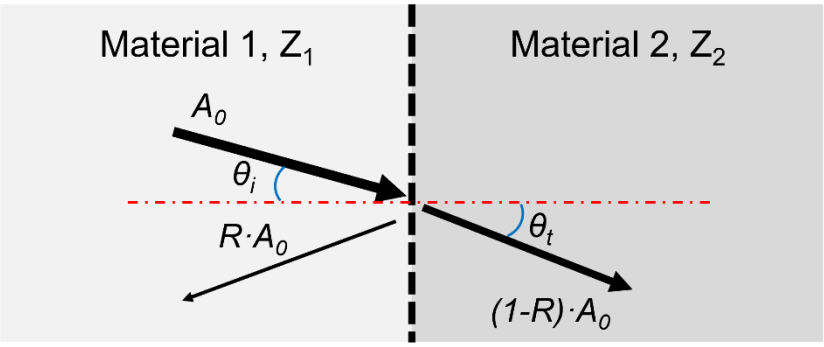

Fig. 2.2 Illustration of non-normal incident reflection. A_0: amplitude of incident wave. R: reflection coefficient. θ_i: incidence angle, θ_t: transmission angle. (eq. 2.9 and eq. 2.10).

This is illustrated in figure 2.2. The change in wave propagation angle at material boundaries is known as refraction. The critical angle is the incidence angle beyond which no sound is transmitted. At interfaces and in absorbing media, a portion of the longitudinal wave is converted into a shear wave. Shear waves are transverse waves which propagate orthogonally to the incident wave. At incidence angles beyond the critical angle, the amount of mode conversion into shear waves increases (White, Clement, and Hynynen 2006).

Scattering is a special case of reflection typically reserved to describe small zones of impedance differences within a medium as opposed to large boundaries. Biological tissues typically exhibit scattering due to the heterogenous compositions down to subwavelength ultrasound scales (Jensen 1991). Scattering is key to enabling ultrasound imaging because it provides the necessary reflection points in tissue to form an image.

Scattering results in attenuation proportional to the length of tissue traveled through and the scattering characteristics of the tissue.

2.1.1.3 Absorption based effects

Acoustic waves propagating through media are subject to attenuation which reduces pressure, p, with distance x according to:

$$p(x) = p_0 e^{-\alpha x} \tag{2.11}$$

Where the absorption factor α is proportional to frequency and has additional coefficients, a, b, which relate to the sound frequency, f, such that:

$$\alpha = a\, f^b \tag{2.12}$$

The tissue-specific attenuation coefficient a typically ranges from 0.1 to 0.7 dB cm^{-1} MHz^{-1} for soft tissue. The power law parameter, b, is close to 1 for most biological tissues (Duck 2013). Scattering and absorption can be lumped into this term for therapeutic modeling purposes where total attenuation is of primary concern (Pinton et al. 2012). Absorption in this case is the process of conversion of vibrational energy into heat. With classical absorption, frictional forces acting on particle motion can cause the density cycle of tissue to dephase with the propagating ultrasound which results in viscous heating (P. N. T. Wells 1975).

2.1.2 Acoustic mechanisms for tissue interactions

2.1.2.1 Heating

Heating from ultrasound due to absorption can be mapped directly to heating through Pennes' bioheat equations which in addition to diffusive heating also account for cooling from blood flow and heat deposition from metabolic flux (Pennes 1945). If the pressure field p is known, the volumetric rate of heat deposition $\dot{Q}$ from ultrasound is: (Nyborg 1981)

$$\dot{Q} = \frac{\alpha p^2}{\rho c} \tag{2.13}$$

Here the dot accent denotes the time derivative. An example showing predicted thermal rise due to a pressure field from a transcranial ultrasound neuromodulation procedure is shown in figure 2.3. Predicting heat deposition and diffusion from ultrasound absorption is useful for hyperthermia procedures as well as procedures like neuromodulation seeking to minimize heating.

High intensity ultrasound deposits sufficient heat for tissue ablation, particularly when the energy deposition rate exceeds the cooling rate from diffusion and circulating blood (F. Wu et al. 2003). Furthermore, by focusing the ultrasound beam, ultrasound can ablate deep tissue without ablating tissue along the path from the transducer to lesion. With phased arrays, the focal pattern can be optimized to distribute this ablation to a range of volumes and geometries (E.S. Ebbini and Cain 1989). A major challenge with thermal applications of ultrasound is delivering heat exclusively to the region of interest (Payne et al. 2011). Because different tissues are more absorbing than others, highly absorbing tissue adjacent to the therapy target such as bone in transcranial therapies are often subject to heating by proxy. The skin boundary is also a common site of excess heating. Tissue heating can be monitored with MRI using MR-thermometry, discussed in more detail in section 2.3.2.

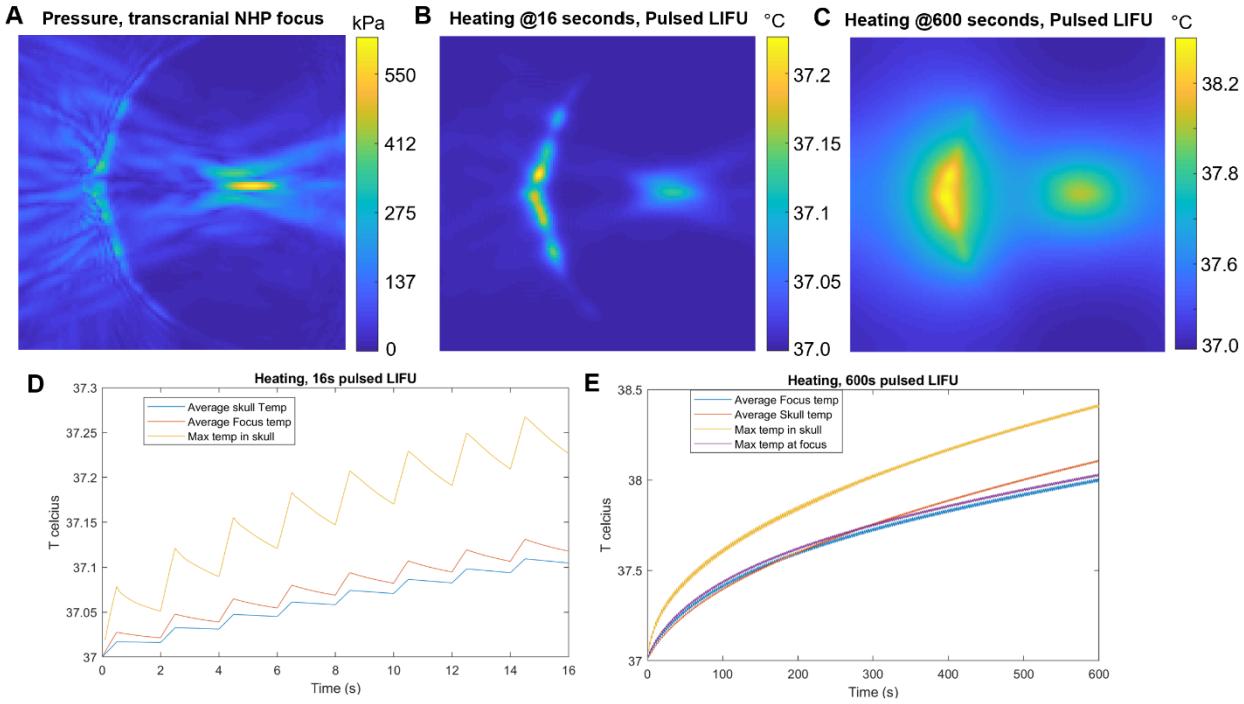

Fig 2.3. Modeling heat deposition and diffusion in therapeutic ultrasound scenarios. A) Pressure field predicted by k-Wave for a 650 kHz transducer through a macaque skull. B) Heating from ultrasound predicted from eq. 2.13 with 16 seconds of pulsed ultrasound at 550 kPa. C) Heating from ultrasound after 600 s of pulsed ultrasound at 550 kPa. D) Plots of heating versus time for the skull average, acoustic focus average, and skull maximum. D) Plots of heating versus time for the focus average, skull average, max in skull, and max in focus.

2.1.2.2 Cavitation

When the peak negative pressure (PNP) of the rarefactional portion of an ultrasound wave is sufficiently low, cavitation can occur. In these cases, dissolved gasses in the tissue coalesce into microbubbles which then undergo cavitation. The mechanical index (MI) was derived to predict the likelihood of cavitation events (Holland and Apfel 1990):

$$MI = \frac{PNP}{\sqrt{f}} \tag{2.14}$$

Here PNP denotes peak negative pressure (rarefactional pressure) in MPa and f is the frequency in MHz. These cavitation events are inherently unstable and typically result in collapse of gas vesicles which result in extreme localized forces (W. W. Roberts et al. 2006). The net effect of cavitation in biological tissue is localized stress and pressures that can mechanically fragment and subdivide tissue, resulting in cellular destruction.

An alternative approach to utilizing cavitation is to introduce exogenous microbubbles to the tissue prior to sonication (Tran et al. 2003). Microbubbles of diameters 2-5 um are administered intravenously and circulate freely through the vasculature with a half-life of approximately 2 minutes. Microbubbles undergo volumetric oscillations (also referred to as cavitation) in the presence of ultrasound. The volumetric oscillation of a microbubble in an incompressible fluid can be modeled by the Rayleigh-Plesset equation (also the RPNNP model after Rayleigh, Plesset, Noltingk, Nepiras, and Poritsky). Forces acting on the bubble surface on the gas side of the bubble are equated to forces acting on the liquid side using Newton's Third Law to give the instantaneous bubble radius of a spherically symmetric bubble with radius R as a function of time: (Leighton 2012)

$$R\ddot{R} + \frac{3}{2}\dot{R}^2 = \frac{1}{\rho_L}\left[P_{G0}\left(\frac{R_0}{R}\right)^{3k} + P_V - \frac{2\sigma}{R} - 4\eta_L\frac{\dot{R}}{R} - P_0 - P_{ac}(t)\right] \tag{2.15}$$

ρ_L is the equilibrium density of the surrounding liquid, $P_{G0} = P_0 - P_V + 2\sigma/R_0$ is the equilibrium pressure inside the bubble; R_0 is the bubble radius at rest; k is the polytropic exponent of the gas; P_V is the vapor pressure inside the bubble; σ is the surface tension for the liquid-gas interface; η_L is the dynamic viscosity of the liquid; P_0 is the hydrostatic pressure in the liquid; and $P_{ac}(t)$ is the driving acoustic pressure. Several modifications to this model have been proposed to incorporate fluid compressibility, shell viscosity,

and surrounding tissue (Qin and Ferrara 2010; Doinikov and Bouakaz 2011). These additional factors are important to capture the behavior of microbubbles during cavitation at higher pressure regimes.

The pressure range at which microbubbles begin cavitation is linked to mechanical index (eq. 2.14). Cavitation thresholds of microbubbles have been extensively studied for a range of ultrasound frequencies and microbubble sizes (Holland and Apfel 1990). Lower frequencies have lower cavitation thresholds. At higher pressures, bubbles begin to collapse in a process known as inertial cavitation. The term "inertial cavitation" is descriptive of the process because the bubbles are collapsing under their own inertia. The shell of the bubble rapidly contracts through a compression phase, and the momentum of the shell is such that during what should become the rarefactional phase, the bubble is unable to expand and instead collapses, often into smaller bubbles (Ohl, Klaseboer, and Khoo 2015). Microbubble facilitated cavitation enables ultrasound blood brain barrier opening, where forces from microbubble volumetric oscillations exerted on surrounding vasculature temporarily increase permeability in tight endothelial junctions. This is discussed in detail in section 2.2.3.

2.1.2.3 Radiation force

As tissue absorbs energy from an incident traveling pressure wave, a portion of the wave's momentum is absorbed and imparted into the tissue resulting in a displacement along the direction of propagation. The time-averaged acoustic radiation force (ARF) imparted on absorbing tissue by a plane harmonic wave can be approximated as:

$$ARF \cong \frac{2\alpha I_{SPPA}}{c} \tag{2.16}$$

where I_{SPPA} is the spatial peak pulse average intensity, and c is the speed of sound in the supporting medium (Sarvazyan, Rudenko, and Nyborg 2010). This equation neglects directivity which is present in focused ultrasound especially with low f-number, spherical transducers. A treatment for radiation force which accounts for directivity has been described (Szabo 2022). Acoustic radiation force impulse (ARFI) imaging uses this force to induce displacements and generate images of relative differences in tissue stiffness (Nightingale 2011). The magnitude of soft-tissue displacement is on the order of microns (<20 μm) for pushing pulses used in ARFI (Selzo and Gallippi 2013). Displacement from ARF generates a shear wave traveling in the plane orthogonal to the beam propagation. The speed of the shear wave can be sampled to generate an image proportional to the tissue's Young's modulus in what is known as shear wave elastography imaging (Sigrist et al. 2017). Tissue stiffness is linked to several indications such as liver health and tumor status making it a useful value to measure noninvasively. Displacement from acoustic radiation force can also be sampled by magnetic resonance imaging (MRI) for acoustic radiation force imaging (MR-ARFI). MR-ARFI is can be used for focus localization in cases where heating is not an option (Nathan McDannold and Maier 2008), and is discussed in greater detail in section 2.3.2 and used in chapter 5 of this work.

2.1.3 Focusing sound

2.1.3.1 Focusing sound

Target regions for therapeutic ultrasound often lie well beneath the skin. In these cases, it is desirable to achieve adequate acoustic power at the target without effecting tissue along the sound path (i.e., nearfield). For this reason, therapeutic ultrasound is typically also focused ultrasound (FUS) where focusing provides a means to remotely concentrate acoustic energy. Factors used to gauge the focusing quality of a transducer include the intensity gain at the geometric focus, the spot size of the focus, and the steering capabilities (in the case of arrays). Each of these can be evaluated in homogenous medium conditions exhibiting linear

propagation based on Huygens' principal of infinitesimal spherical radiators. The complex acoustic pressure at a point, $p(r)$, due to a radiating surface, *S,* is given by the Rayleigh-Sommerfeld integral: (E.S. Ebbini and Cain 1989)

$$p(r) = \frac{j\rho ck}{2\pi}\int^{s} u(r')\frac{e^{-(\alpha+jk)|r-r'|}}{|r-r'|}dS \tag{2.17}$$

Here $k, \alpha, \rho, c,$ and u as previously introduced in eq. 2.2, 2.3, 2.6, and 2.12 are, wavenumber, attenuation coefficient, density, speed of sound, and particle velocity. r and r' are the observation and source points, respectively, and S is the radiating surface.

This integral can be used to evaluate the intensity gain for a given transducer at its focus. At the geometric focus of a spherically curved surface with uniform particle velocity in a non-attenuating ($\alpha = 0$) medium, the pressure is given by: (VanBaren et al. 1995)

$$p(R) = \frac{\rho cuA}{\lambda R} \tag{2.18}$$

Here A is the area of the active surface, *S,* of the transducer, $R = |r - r'|$ and λ was substituted for $\frac{2\pi}{k}$. This is useful because by describing the intensity, $I(R)$, as:

$$I(R) = \frac{p(R)^2}{\rho c} \tag{2.19}$$

And the intensity at the surface as:

$$I(0) = \rho c u^2 m \tag{2.20}$$

The intensity gain relative to the array's surface is given by:

$$\frac{I(R)}{I(0)} = \left[\frac{A}{\lambda R}\right]^2 \tag{2.21}$$

Practical manufacturing constraints with arrays limit the coverage (proportion of A which can be active surface). Eq. 2.21 provides an important benchmark to compare the intensity gain of a proposed array to that achievable by an ideal spherical array with the same radius of curvature and aperture (VanBaren et al. 1995).

Equation 2.17 also provides a means to evaluate the spot size of the focus for a transducer for both steered and non-steered foci. Equation 2.17 can directly solve for three-dimensional pressure fields by integrating the pressure contribution from all points on the emitting surface for each point in space. The pressure fields produced by therapeutic transducer foci are commonly evaluated by the full-width-at-half maximum (FWHM) pressure and intensity spot sizes as well as non-focal maxima.

Equation 2.17 can also provide the phases needed to electronically steer an array by solving for $u(r')$, the complex particle velocity at each element (E.S. Ebbini and Cain 1989). Not only does this approach compute optimal phase and amplitude values for the electronic beam-steering, it also generalizes to produce arbitrarily shaped foci and null-pressure areas. This method is used for all beam steering in this dissertation. However, it is worth noting that for steering to a single point, driving phases can be directly computed by converting the distances between each element and the desired target into wavelengths and then phase such that:

$$\varphi_n = 2\pi \, mod\left(\frac{z_n}{\lambda}, \lambda\right) \tag{2.22}$$

Here φ_n is the phase for the nth element, z_n is the distance between the desired focus and the nth element, and *mod()* represents the modulus operator.

In section 2.1.3.2, we introduce a variety of therapeutic transducers which have been developed along with their unique focusing properties. In chapter 4, we discuss design aspects of spherical phased arrays in detail and present the design and validation of an array for small volume blood-brain barrier opening in non-human primates.

2.1.3.2 Transducer options

The most basic transducer is a flat piston transducer where the entire active surface is a single electrically coupled piezoelectric element. Historically, lead zirconate titanate (PZT), manufactured as a single, continuous crystal, was the piezo of choice. Bulk PZT ceramics are still the highest efficiency piezo option in terms of mechanical loss (W. A. Smith and Auld 1991). However, bulk ceramics have been largely replaced by piezocomposite materials. Piezocomposites are a combination of a polymer material with lower acoustic impedance and some flexibility merged with pieces of piezo ceramics. 1-3 piezocomposites (where 1-3 denotes a connectivity formalism compared to 0-3 and 2-2 which also exist but are less popular) are made up of small columns of piezoelectric ceramics embedded into a polymer material (Wilm et al. 2002). There are several advantages of 1-3 piezocomposites compared with bulk PZT. Composites have lower acoustic impedance which improves coupling efficiency into tissue and bandwidth. The polymer portion of the composites can be selected to add flexibility to the material which enables manufacturing of curved surfaces. Composites also dampen vibrational modes other than the thickness mode which improves the decoupling of neighboring elements (Chapelon et al. 2000).

Typically, a matching layer with an impedance value between the piezo impedance and the target medium impedance is included to improve transmission into the medium. Backing the piezo with air improves the forward transmit and receive efficiency of the element (due to air's extremely low acoustic impedance) and is typically used for therapeutic transducers (Szabo 2004). Air backing increases the ring-up and ring-down time of the unit which degrades axial resolution in imaging applications compared to backing with a damping material. The focal gain of a single element transducer can be improved by increasing the active surface area and using a spherical or parabolic element. Single element transducers are common for non-destructive testing, oceanographic measurements, industrial flow applications, and some biological applications. The neuromodulation work described in chapter 3 uses small aperture (1"), 250 kHz and 500 kHz transducers. Single element transducers have been implanted in the extradural space for blood-brain barrier opening in humans in multiple clinical trials (Carpentier et al. 2016).

Single element transducers are the building blocks for imaging and therapeutic arrays which feature multiple elements that can be independently driven and/or used for receiving. With therapeutic arrays, it is common to place the elements about a spherical surface (E.S. Ebbini and Cain 1991). The spherical surface improves the focal gain of the transducer while reducing near-field pressure distributions but at the cost of degrading steering performance (Clement et al. 2000). Therapeutic arrays offer the benefit of steering as well as aberration correction (Clement and Hynynen 2002) over single element transducers but add cost and complexity for the transducer itself as well as the supporting electronics. Recently, a rapid-prototyping modular approach to array fabrication has been developed which lowers the cost of these systems while enabling multiple configurations to be used for a given set of element modules (Y. Kim et al. 2014). The design considerations of spherical arrays are outlined in detail in chapter 4, which describes the design of an array for transcranial macaque blood-brain barrier opening therapies.

Holographic acoustic plates and acoustic lenses have been developed to bring phase control for steering, aberration correction, and arbitrary focal patterns to lower-cost single element transducer systems. Acoustic lenses use a layer of material with varying thickness to impart a phase profile on the transmitted wave front (Maimbourg et al. 2018). Acoustic lenses can improve acoustic foci through human skulls. Acoustic lenses do not provide amplitude control across the aperture. Holographic acoustic plates use a separate approach for thickness calculations, working under Fabry-Perot resonance assumptions, and theoretically allow for both phase and amplitude control (Jiménez-Gambín et al. 2019). Holographic plates are typically used for arbitrary focal shaping and use flat transducers in place of spherical to allow for better focal shaping performance (less directivity).

A common consideration for transducer selection is transmit/receive capabilities. While some applications of therapeutic ultrasound only use transmitted sound, others benefit from being able to receive sound during therapies. In some cases, entirely separate transducers are used for receiving which avoids requirements for complex equipment but does not inherently align the foci of the transducers (N. McDannold et al. 2012). Another approach is to embed a receive element(s) into the transmit array ((H. A. Kamimura et al. 2019; Vandiver Chaplin, Phipps, and Caskey 2018). This enables receiving at separate frequencies by tuning receive element sensitivities and ensures good alignment with the transmit focus, but results in direct coupling of energy into the receive elements. A third approach is to build a therapeutic array with a central cavity to house an imaging transducer and is referred to as a dual-mode transducer (Emad S. Ebbini, Yao, and Shrestha 2006). Dual-mode transducers provide the diagnostic imaging capabilities of an imaging array paired with the capabilities of the therapeutic array while also inherently co-registering the foci of the two transducers.

There are several ablation arrays which do not use curved faces. Profound Medical (Toronto, CA) uses a linear ablation probe for trans-urethral prostate cancer ablation (Chopra et al. 2012). The probe works in conjunction with a rectal cryo-probe to limit off-target cooling. A flat 518 kHz array with 6144 elements

with λ/2 spacing (96 8x8 modular elements) has been developed for uterine fibroid ablation (Aslani et al. 2020) and is being testing in a clinical trial (NCT03323905).

Several non-conventional elements and emitting materials have been developed. Polyvinylidene fluoride (PVDF) is a ferroelectric polymer with lower acoustic impedance (more comparable to human tissue than PZT) and more broadband sensitivity (Foster, Harasiewicz, and Sherar 2000). PVDF transducers have been adopted for passive cavitation detection systems which require high bandwidth and sensitivity (O'Reilly and Hynynen 2010). An additional alternative to piezoelectric transducers are capacitive micromachined ultrasonic transducer (CMUT) (Ladabaum et al. 1998). CMUTs were first developed for air coupled applications, but when initial testing revealed potential bandwidth, sensitivity, and form-factor advantages over piezoelectrics the focus shifted also to medical applications. Despite several decades of development, their adoption into clinical devices is limited to an estimated 23 companies (Brenner et al. 2019). One limitation to CMUTs is lower electro-acoustic efficiency (Meynier et al. 2012). Carthera, a company developing extradural implants for blood-brain barrier opening, attempted to incorporate CMUTs into early designs, but their attempts failed to meet robustness criterion prompting them to switch to piezoelectrics (M. Canney, personal communication, October 26, 2022).

2.2 Therapeutic applications of ultrasound

2.2.1 State of therapeutic ultrasound

The variety of mechanical and thermal mechanisms exhibited by ultrasound give it a range of therapeutic applications and clinical indications. Heating from the thermal effects of absorption enables ablation of tissue, and the most clinically adopted therapeutic ultrasound procedures are ablative. These include thalamotomy for essential tremor and Parkinson's disease (Lipsman et al. 2013), prostate ablation for

prostate cancer (Madersbacher et al. 1995), and uterine fibroid ablation (Hindley et al. 2004). Other targets for ablation reaching clinical trial status include liver cancer (L. Chen et al. 1993), breast cancer (Schmitz et al. 2008), bone metastasis (Liberman et al. 2009), and facet joint ablation for back pain (Harnof et al. 2014). An additional thermal based mechanism is skin tightening, in which thermal rise is leveraged to denature collagen in the skin to achieve an aesthetic effect on skin (Alam et al. 2010).

Other techniques being explored include histotripsy, sonobiopsy, immunotherapy, neuromodulation, and blood-brain barrier opening. Histotripsy is a technique for fractionating soft tissue with low cycle count (single cycle or <1 cycle), high intensity pulses (>6 MPa at 1 MHz) which generate a destructive shockwave (W. W. Roberts et al. 2006). Histotripsy may have potential for treating hepatocellular carcinoma (Worlikar et al. 2018), and liver cancer (Vlaisavljevich et al. 2013) among other indications where conventional ablation is difficult due to high perfusion cooling in vascular organs. Sonobiospy uses ultrasound focused to brain tumors in the presence of circulating microbubbles to increase the blood concentration of tumor-derived molecular biomarkers (Pacia et al. 2022). By increasing the presence of these biomarkers, the hope is that diagnosis sensitivity and specificity can be improved. Immunomodulation via focused ultrasound is being explored for the potential to trigger or improve the immune system's response to cancer, Alzheimer's, and other disorders. FUS immunotherapy uses ablation, histotripsy, or mild hyperthermia to modulate an immune response (Curley et al. 2017). In the presence of certain sensitizing drugs and molecular oxygen, focused ultrasound can generate localized cytotoxic reactive oxygen species. These species may provide a means for treatment of solid cancerous tumors (Costley et al. 2015).

We introduce these topics in brief to provide an overview of the field of therapeutic ultrasound. In the next two sections we discuss the two applications of therapeutic ultrasound explored in this dissertation in more detail. These are neuromodulation and blood-brain barrier opening.

2.2.2 Ultrasound Neuromodulation

Ultrasound can alter the behavior of the nervous system, and researchers have demonstrated these effects sporadically throughout the past century in different *in vivo* and *ex vivo* preparations (Fry, Ades, and Fry 1958; Mihran, Barnes, and Wachtel 1990). Since this time, researchers have validated ultrasound neuromodulation (USN) in animal models such as in vivo murine (W. Lee et al. 2018; H. A. S. Kamimura et al. 2016), rabbit(S.-S. Yoo et al. 2011), sheep (W. Lee et al. 2016), and non-human primate (Folloni et al. 2019). USN holds exciting potential as a means to remotely excite or inhibit neural pathways (Tyler et al. 2008). USN may hold the potential to stop tremors, reduce chronic pain, promote neurogenesis, or alter learning. Achieving these goals requires USN to reach consistent effect. One feature limiting the advancement of USN is the lack of understanding of the mechanisms underlying USN. Although heat is known to affect neural activity at the bulk and molecular scale (J. Wells et al. 2007; Shapiro et al. 2012), USN is frequently observed using power levels that do not generate significant heat (< 0.1 C) (Wattiez et al. 2017).

There is increasing evidence that mechanical effects of ultrasound underly neuromodulation, yet the discussion remains open (Blackmore et al. 2019). Ye et al. found that mechanical index correlates with response frequency in *in vivo* mice, directly linking particle displacement to USN (Ye, Brown, and Pauly 2016). A study in c. elegans showed that mutants without thermal sensitivity responded to US while mutants without mechanical sensitivity did not (Kubanek et al. 2018). This mechanical effect may be manifesting via ion channels. Researchers observed ion currents in bi-layer preparations containing the Nav1.2 ion channel during sonication (Prieto et al. 2013). Pyramidal neurons express stress activated cation channels which trigger action potentials when subjected to pressure (Nikolaev et al. 2015). Ion channel current modulation dependence on US power has been reported in the Xenopous oocyte (Kubanek et al. 2016). Prieto et al. showed activation of the Piezo1 channel by 43 MHz ultrasound and report acoustic streaming rather than particle displacement as the primary mechanism (Prieto et al. 2018).

In 2022, a strong case was made that mechanical stress on the plasma membrane due to ultrasound is the transduction mechanism underlying USN (S. Yoo et al. 2022). This work provided supporting evidence on multiple fronts. An assortment of ion channels were genetically and pharmacologically inhibited which reduced ultrasound response. Upregulation of these channels increased ultrasound response. A signal pathway was reported whereby ultrasound results in calcium influx through endogenous mechanosensitive ion channels which triggers signal amplification by calcium-gated sodium channels, and results in robust spiking activity. They show the pathway functions within neurons and does not require synaptic transmission. A fiber optic thermometer recorded temperature changes below 0.02°C at all parameters tested (300 kHz transducer). High speed camera images did not observe cavitation or large membrane deformations.

An alternative transduction mechanism excluding ion channels is that pressure-induced displacement of the lipid bi-layer generates action potentials (Krasovitski et al. 2011). By extending the Hodgkin and Huxley model to include capacitance changes in the cell membrane due to ultrasound, Plaksin et al. created a model (Plaksin, Kimmel, and Shoham 2016) which matches well with *in vivo* observations of mouse motor cortex activation via ultrasound (King et al. 2013). However, these *in vivo* observations may be confounded by auditory transduction (Sato, Shapiro, and Tsao 2018).

Citation	Ultrasound Parameters	Readout	Model	Response % or yes/no
(Tyler et al. 2008)	440 kHz, <1 MPa, pulsed and continuous	Fluorescent Imaging	*Ex vivo* mouse	Yes
(Tufail et al. 2010)	0.35-0.5 MHz, 1.5-2.5 kHz PRF, 0.36-0.42 W/cm^2 I_{SPTA}	Electromyogram and tail movement	Mouse	Yes
(Legon et al. 2012)	350 kHz, 70-100 PRF, 11.8-54.8 W/cm^2 I_{SPPA}	fMRI	Human	Yes
(King et al. 2013)	500 kHz, 0.03 to 1.11 MPa, continuous and pulsed	Electromyogram	Mouse	0-64%
(Deffieux et al. 2013)	320 kHz, continuous, 4 W/cm^2 I_{SPPA}	Eye saccade	Macaque	Yes
(H. Kim et al. 2014)	350-650 kHz, pulsed and continuous, 4.8-5.6 W/cm^2 I_{SPTA}	Tail movement	Rat	10-100%
(W. Lee et al. 2015)	210 kHz, 500 Hz PRF, 35 W/cm^2 I_{SPPA}	Tactile response	Human	Yes
(W. Lee et al. 2016)	250 kHz, 500 Hz PRF, 6.6-14.3 W/cm^2 I_{SPPA}	Electroencephalograph	Sheep	100%
(G.-F. Li et al. 2016)	5 MHz, 1 kHz PRF, 0.13-0.23 W/cm^2 I_{SPTA}	Tail movement	Mouse	0-70%
(Ye, Brown, and Pauly 2016)	0.3 - 2.9 MHz, continuous, 0-150 W/cm^2 I_{SPPA}	Electromyogram	Mouse	0-70%
(H. A. S. Kamimura et al. 2016)	1.9 MHz, 1 kHz PRF, 1.1-1.8 MPa	Motor response and pupil dilation	Mouse	0-70%
(Wattiez et al. 2017)	320 kHz, , 240-410 kPa, 100 ms burst	Electrophysiology and eye movement	Macaque	47-53%
(Dallapiazza et al. 2017)	1.14 MHz, 10 Hz PRF, 35-40 W/cm^2 I_{SPPA}	Electrophysiology	Pig	76%
(Gulick et al. 2017)	200 kHz, 1 kHz PRF, 4.5 W/cm^2 I_{SPTA}	Motor response	Rat	>50% in 4 of 10 sessions
(Guo et al. 2018)	500 kHz, 200 kPa, 1 kHz PRF	Fluorescent Imaging and Electrophysiology	Guinea pig	**No**
(Sato, Shapiro, and Tsao 2018)	500 kHz, 1.5 kHz PRF, 4.2 W/cm^2 I_{SPTA}	Fluorescent Imaging	Mouse	**No**
(Legon, Bansal, et al. 2018)	500 kHz, 1 kHz PRF, 23.87 W/cm^2 I_{SPPA}	Electroencephalograph	Human	Yes
(Fisher and Gumenchuk 2018)	510 kHz, 1 kHz PRF, 0.17 MPa	Ca^{2+} Imaging	Mouse	Yes
(Kubanek et al. 2018)	10 MHz, 30 - 3000 Hz PRF, 0 - 1 MPa	Motor response	*C. Elegans*	0-80%
(P.-F. Yang et al. 2018)	250 kHz, 2kHz PRF, 0.5-0.9 MPa	fMRI	Macaque	Yes

Table 2.1. An aggregation of ultrasound neuromodulation parameters, models, and outcomes. This is not a comprehensive list but meant to be representative of foundational works published at the time of the work done in chapter 3 (2019). In some cases parameters and results listed are from one of the experiments described in a publication which included multiple experiments. Yes/no is used for outcomes which did not report outcomes in terms of a % likelihood but did observe or not observe an effect. PRF: pulse repetition frequency. fMRI: functional magnetic resonance imaging. I_{SPPA}: spatial peak pulse average intensity. I_{SPTA}: spatial peak temporal average intensity.

To illustrate the range of ultrasound parameters explored for neuromodulation and the variation in results, table 2.1 aggregates methods and findings from several works. The variety of parameters and outcomes highlights a need for consensus on which parameters should be used and for what purpose. A consensus could improve the response rate of neurons to ultrasound and the consistency of results across studies. Table 2.1 shows response rates ranging from no response to 100% response. While readout scheme (calcium imaging, electrophysiology, motor response, functional magnetic resonance imaging) and animal model (mouse, rat, pig, sheep, non-human primate, or human) likely affect response rates, ultrasound parameters also play a role and are most readily tunable. The work in chapter 3 seeks to address the parameter space question surrounding ultrasound neuromodulation by studying the process in a controlled environment.

We developed a model to study neural activity in the presence of ultrasound and used it to evaluate the effectiveness of a range of ultrasound parameters for modulating calcium influx in neurons. The model revealed a pulse repetition frequency dependence on neural activity and an ion channel dependence on the cellular mechanisms linking ultrasound and calcium influx. These findings strengthen the understanding of ultrasound neuromodulation and may increase the consistency of outcomes.

2.2.3 Ultrasound blood-brain barrier disruption

2.2.3.2 Disruption of the BBB with ultrasound

The blood-brain barrier (BBB) refers to the network of vasculature supplying the brain which exhibits lower permeability than elsewhere in the body (Pardridge 2012). Increased tight junctions in endothelial cells are responsible for this decreased permeability. Natural transport across the BBB is limited to molecules smaller than 400 Da and having fewer than 8 hydrogen bonds (van de Waterbeemd et al. 1998). This creates a scarcity of drugs which permeate the BBB at therapeutically relevant concentrations with 98% of small-molecules not meeting this criterion (Pardridge 2005).

Major efforts to design drug delivery strategies to overcome this have been undertaken in pharmacological research (Pardridge 2006). Strategies for enhanced transport without modifying tight junctions include chemical-mediated transport, receptor-mediated transport, and molecular trojan horses (Patel et al. 2009). Each of these hijack existing or engineered pathways through the endothelial cells to increase the amount of transport for a target molecule. Recent advances in nanoparticle fabrication techniques have added nanoparticles to the list of tools, but these need to overcome safety and scalability concerns (Ferraris et al. 2020). Systemic administration of mannitol can increase the delivered concentration of drugs through hyperosmotic shock (Greenwood et al. 1988). Mannitol is used mainly for administration of anticancer agents in the treatment of brain tumors and has been tested in clinical and preclinical trials. However, preclinical work demonstrated structural brain damage, plasma extravasation, altered glucose uptake, and expression of heat shock proteins can occur, which have restricted its broad adoption (Miller 2002).

Ultrasound was first shown to increase BBB permeability without circulating microbubbles in 1995 (Vykhodtseva, Hynynen, and Damianou 1995). These initial results failed to identify ultrasound parameters which could increase permeability without causing permanent tissue damage. This is likely due to the requirement for cavitation to increase BBB permeability. Without exogenous microbubbles, high pressures were required to coalesce gas in the tissue into microbubbles which then are likely to violently collapse during the extreme rarefactional phase. By introducing exogenous microbubbles, the BBB could be temporarily and safely opened (Hynynen et al. 2001). With circulating microbubbles, the acoustic parameters required were much lower and largely removed concerns of skull heating and tissue hyperthermia. In fact, the permeability opened at such low pressure (0.8 MPa at 1.63 MHz) that the mechanical effects of the oscillating microbubbles were identified as the predominant driving factor instead of hyperthermia.

The mechanisms of microbubble-facilitated ultrasound BBB opening have been investigated in detail. Microbubbles oscillate volumetrically when subjected to ultrasound at appropriate frequency and pressure. The expansion ratio of bubbles can reach 30 fold under conditions employed for BBB opening (Ilovitsh et al. 2018). At low acoustic pressures, the volumetric oscillations are repeated in what is denoted as stable cavitation. Mechanical interactions between the expanding microbubbles and vascular endothelial cells are likely responsible for the increased permeability (Tung et al. 2011). At the cellular level, the permeability is linked to endothelial cell cytoplasmic openings in the form of fenestration, channel formation, and opening of tight junctions (Sheikov et al. 2004). Direct observations of microbubble interaction with micro vessel walls has been observed to support this theory (Caskey et al. 2007). Apart from direct coupling of the oscillating bubble and surrounding vasculature, acoustic streaming or radiation force on the bubbles may also increase permeability (N McDannold, Vykhodtseva, and Hynynen 2006). The tunneling of microbubbles into channel walls has been observed in gel phantoms and is attributed to radiation force deflecting bubbles into the walls (Caskey et al. 2009). At higher acoustic pressures, the volumetric oscillations begin collapsing in what is referred to as inertial cavitation. Inertial cavitation results in shock waves and high-velocity jets (Leighton 2012), the formation of free radicals (Edmonds and Sancier 1983), and high local temperatures (Apfel 1982). Inertial cavitation has been linked to severe mechanical damage to surrounding tissue, including edema and hemorrhage (N McDannold, Vykhodtseva, and Hynynen 2006; O'Reilly and Hynynen 2012).

The parameters for ultrasound facilitated BBB opening have also been studied in detail. Frequencies used for BBB opening are typically between 200 kHz and 1.5 MHz with lower frequencies exhibiting higher skull transmission and larger foci. A parametric study in rabbits linked the threshold for BBB opening to mechanical index (equation 2.12) with a mechanical index of 0.46 giving a 50% probability of disruption (Nathan McDannold, Vykhodtseva, and Hynynen 2008a). Pulsed ultrasound is typically used to avoid heating with pulses around 10 ms in length and pulse repetition frequencies varying from 0.5 to 5 Hz). Pulse repetition frequency within this range was shown to not effect opening size (Nathan McDannold,

Vykhodtseva, and Hynynen 2008b). Reducing burst length to 1 and 0.1 ms reduced opening. However, shorter pulses have since been investigated to further reduce heating (Morse et al. 2019). The size of blood-brain barrier opening is linked to acoustic pressure with higher pressures facilitating transport of increasingly large agents (up to 2000 kDa) (H. Chen and Konofagou 2014). Microbubble doses between 50, 100, and 250 µl/kg all gave the same opening outcomes in a parametric rabbit study (Nathan McDannold, Vykhodtseva, and Hynynen 2008b). The outcome of opening is linked to tissue type (grey matter vs. white matter) in the brain. Grey matter disruption occurs at lower pressures (Carpentier et al. 2016) and in greater extent likely due to increased vascularity (N McDannold, Vykhodtseva, and Hynynen 2006; M. E. M. Karakatsani et al. 2017).

2.2.3.2 Cavitation monitoring

Due to the link between inertial cavitation and tissue damage, it is desirable to keep pressures at the target within the range that causes stable cavitation. In practice this is made challenging in large animal and clinical procedures due to variable transmission through the skull. For this reason, it is common to use acoustic feedback to control pressure levels. Cavitating microbubbles emit pressure waves which map to the status of the oscillations (none, stable, inertial). Stably oscillating microbubbles produce pressure waves with harmonic frequency content at whole number intervals (Leighton 1994) of the fundamental frequency. At the upper end of the pressure range for stable cavitation, nonlinear oscillations result in ultra-harmonic content and half fraction intervals ($0.5*f_0$, $1.5*f_0$, $2.5*f_0$, and so on) with f_0 being the fundamental frequency). Inertial cavitation events result in highly non-linear pressure waves with broadband frequency content.

These differences in emitted pressure waves corresponding to the cavitation conditions provide a means for real time feedback during BBB opening therapies. In general, there have been three approaches to cavitation monitoring feedback. First of these are constant pressure, where pressure is estimated based on a derating

factor and cavitation signals are used only as a comparative measure of safety (hemorrhage, edema, histology) (Pouliopoulos et al. 2021; S.-Y. Wu et al. 2014). The drawback to this approach is that pressure is set based on a fixed derating factor and that procedures with outliers may result in insufficient or excess pressure delivery. However, with sufficiently low frequency transducers or models with thin skulls this approach is effective.

A second approach is to tune PNP to produce an empirically determined magnitude of emissions, as first proposed by Arvanitis in non-human primates (Arvanitis et al. 2012). In this scheme, an amount of harmonic emission is empirically chosen as a target value. During therapies, the applied pressure can be manually or automatically increased until that amount of emission is detected. This approach was shown to be effective using harmonic emissions for doxorubicin delivery (T. Sun et al. 2017). This technique was extended to incorporate baseline subtraction, where baselines are captured for all candidate amplitudes prior to the arrival of bubbles (H. A. Kamimura et al. 2019). In this work, the feedback system avoided damage in non-human primates while achieving BBB opening. A strength of this approach is that it provides real-time pressure adjustment which helps capture variance in transmission from therapy to therapy. A downside to the approach is that it requires a set of initial test subjects to determine the target emission value. Furthermore, this target value must be identified empirically for each new ultrasound device used for BBB opening.

A third approach which has been clinically adopted is to incrementally increase PNP until the detection of a threshold event and then reduce the pressure to an empirically determined value. This approach was effective using ultraharmonics as the threshold event and reducing pressure to half the threshold value (O'Reilly and Hynynen 2012). This approach has also been adapted to work using subharmonic emissions (Burgess et al. 2014) and was adopted clinically for BBB opening trials (Lipsman et al. 2018; Abrahao et al. 2019; Mainprize et al. 2019). A strength of the threshold event approach is that it provides an opportunity to inform low pressure pulses that may not result in detectable cavitation with signals from high pressure

pulses that do result in detectable cavitation. For instance, if the system detects the onset of inertial cavitation or ultraharmonics at one pressure level, it can be assumed that some cavitation is occurring at the target at significantly lower pressures even if cavitation signals were not measured at those levels. This approach may be beneficial to cavitation monitoring systems with signal detection limits higher than the magnitude of emissions from transcranial, low pressure, stable cavitation events.

Several factors confound using cavitation feedback to estimate *in situ* pressure. Microbubble concentration is not constant throughout the brain (Prada et al. 2021). Harmonic signal amplitude increases with microbubble concentration. Therefore, the ideal emission amplitude-based feedback metric would change based on the focus location in the brain and the microbubble concentrations of that location. Practically the variance in microbubble concentration could be partially accounted for by updating the target emission value based on which tissue type or what ratio of tissue types overlap with the acoustic focus. Skull distortions also produce high variability in the magnitude of bubble emissions incident on the receive element. Thickness, density, porosity, and incidence angle vary across skulls and patients and factor into the transmitted amplitude of both the therapy pulse and the detected microbubble emissions. The magnitudes of returning signals are affected by receive element sensitivity. Because magnitude is part of the empirically determined dose decision, the empirical relationship must be re-established for each system.

Systems have been developed which take cavitation monitoring a step further by adding spatial information using passive cavitation mapping. Passive cavitation mapping was originally developed for diagnostic imaging purposes but has shown been shown effective in preclinical models for predicting BBB opening sites (Deng et al. 2016). Incorporating this technology into clinical studies has added challenges due to significant skull distortions which violate beamforming assumptions (Ryan M Jones, O'Reilly, and Hynynen 2013) . Complex custom transcranial transducers with multiple receive elements distributed about a large aperture are required to enable this approach along with beamforming algorithms which factor in skull aberration (Ryan M. Jones et al. 2018). Cavitation mapping may help predict and control BBB opening

outcomes like volume and location of disruption with higher precision than enabled with a single receive element. Also, because of the spatial information provided, cavitation mapping may enable BBB opening procedures without MRI guidance or evaluation, which would greatly reduce cost and complexity while increasing the treatable population by enabling procedures at clinical sites where MRI is unavailable.

Chapters 4 and 5 of this work focus on BBB opening. Chapter 4 describes the design and initial testing of a transducer for small volume blood-brain barrier opening in the macaque. Chapter 5 describes the *in vivo* validation of the transducer along with MRI based outcome evaluation. The spatial specificity of ultrasound BBB opening is limited by the spot size of the transducer used. In applications such as drug-delivery for glioblastoma, desired opening volumes are large. However, for gene-therapy, the desired opening volume matches the size of the brain region that is the target of the therapy. Table 2.2 aggregates the specifications and performances of prior systems tested for *in vivo* transcranial non-human primate BBB opening procedures. The table also the specification and performance of the transducer designed and tested in chapter 4 and five of this work.

Citation	Transducer	Spot size [mm]	Opening Volume [mm^3]
(Marquet et al. 2011)	500 kHz single element	-	24 - 285
(N. McDannold et al. 2012)	ExAblate 4000, 220 kHz, 1024 channels	4 x 10 *	~1000 (multi-point therapies)
(Marquet et al. 2014)	500 kHz single element	3 x 21	115
(S.-Y. Wu et al. 2014)	500 kHz single element	5.85 x 34	112 - 495
(Downs, Buch, Karakatsani, et al. 2015)	500 kHz single element	3 x 21	462 - 605
(Downs, Buch, Sierra, et al. 2015)	500 kHz single element	3 x 21	29 - 2480
(Samiotaki et al. 2017)	500 kHz single element	5.85 x 34	160 - 850
(M. E. M. Karakatsani et al. 2017)	500 kHz single element	5.85 x 34	142 - 854
(S.-Y. Wu et al. 2018)	500 kHz single element	5.85 x 34	100 - 600
(H. A. Kamimura et al. 2019)	500 kHz annular array	2.8 x 33	-
(Pouliopoulos et al. 2020)	250 kHz single element	6 x 49	153
(M. E. Karakatsani et al. 2021)	500 kHz single element	5.85 x 34	57 - 64
(Constans et al. 2020)	245 kHz single element	6 x 39	-
(Pouliopoulos et al. 2021)	250 kHz single element	6 x 49	680 - 1413
(Zhou et al. 2021)	300 kHz single element	6.9 x 30	-
(Zhou et al. 2022)	300, 650, and 800 kHz single element	~ 5 x 20 **	-
Our system	**1 MHz phased array**	**1.9 x 9.5 *** **	**59 ± 37.3 **** **

Table 2.2. Specifications and performance of systems used for transcranial blood-brain barrier opening in non-human primates. * Spot size for 220 kHz mode (Raspagliesi et al. 2021). ** Spot size only reported for 800 kHz transducer. *** Spot size when steered inward 1 cm. **** Opening volume at cortical targets. - : value not reported.

2.3 Essential adjacent technologies

2.3.1 Acoustic simulations for transcranial ultrasound

Computational techniques for acoustic field predictions have played a key role in transcranial ultrasound for the past two decades. Aberrations are imparted on wave fronts as they pass through skull, resulting in distorted foci with spatial shift and decreased intensity. It was clear from early on that the effect of the skull would have to be considered for both the transducer design stage and therapy stage. Early numerical studies evaluated the feasibility of transcranial focusing, the appropriate frequency ranges to use, and the ideal size of elements (J. Sun and Hynynen 1998). Hydrophone measurements of transcranial foci revealed that without phase correction, the acoustic focus is inadequate for accurate therapy in many skulls (Clement et al. 2000).

Wavevector-frequency domain (also termed k-space) models have been most widely adopted for transcranial ultrasound simulations, offering the ability to incorporate heterogeneous media into solutions while demonstrating stability out to computationally suitable spatiotemporal step sizes. An early model used for non-invasive (hydrophone-free) correction of a transcranial focus used a k-space model which simulates elements of a phased array independently and approximates the skull for each as a homogenous plane (Clement and Hynynen 2002). This model computes the refraction and transmission for each wavevector independently using an intermediate ray tracing step and outputs the expected phase deviation from water at the focus. The angular spectrum technique is applied for grid portions in water and brain to reduce computation time. The Clement technique offers a method for incorporating the size and shape of the skull into the acoustic field while taking advantage of the computational efficiency of the Fourier transform and its relationship to acoustic propagation. The Clement technique is reportedly the closest published work to what is used in clinical systems for phase correction (Ryan M Jones and Hynynen 2016)

(apart from microbubble based correction which is used in some blood-brain barrier opening procedures). A limitation of the Clement model is that is treats the skull as a plane of homogenous media for each element and fails to incorporate small scale variations in the skull. The model also ignores acoustic nonlinearity. A practical limitation is the lack of a public repository with implementation code.

Most similar to the Clement approach and of recent interest is the hybrid angular spectrum (HAS) model (Vyas and Christensen 2012). Similar to the Clement model, HAS uses the angular spectrum technique to propagate the pressure field in the k-space domain through homogenous portions of the medium. Rather than assuming the medium heterogeneity can be represented as a single plane as in the previous model, HAS incorporates voxel-wise heterogeneity by alternating between k-space projection and a spatial plane-by-plane propagation. HAS was shown to improve transcranial focusing over the clinically available proprietary phase-correction model (Leung et al. 2021) and to predict thermal rise in essential tremor treatments (Leung et al. 2019). A major limitation of this approach is that it has not been extensively validated in highly heterogeneous media.

A third option, the k-space pseudospectral method, provides a balance of computational efficiency, voxel-wise heterogeneity, and time-domain output (Bojarski 1982). As with the two prior models, this approach uses a propagator expressed in the spatial frequency domain (k-space) but combines it with a finite difference approach. Rather than solving a resulting pressure field from an initial pressure distribution, this method can solve temporal pressure fields given a temporally varying excitation source (Treeby and Cox 2010). The grid-wise finite differences are computed using a spectral method rather than a classic numerical derivative which facilitates stability at larger spatial step sizes. Furthermore, this approach can be extended to incorporate acoustic nonlinearities (B/A parameter) (Beyer 1997; Martin, Jaros, and Treeby 2020). This model has been packaged into a freely available, well documented MATLAB library (k-wave.org). It's accuracy has also been validated in transcranial scenarios (Robertson et al. 2017). CUDA solvers are

provided which leverage GPU capabilities to provide suitably fast computation. For these benefits, k-Wave has been the simulation approach of choice for simulations used throughout this work.

Simulations guide the design of a transducer for transcranial blood-brain barrier opening in chapter 4 of this dissertation. The methods used for computing simulation grids is described in this chapter along with the approach for computing acoustic properties from simulation grids.

2.3.2 MRI for guidance and evaluation

2.3.2.1 MRI for evaluation

MRI has found an essential role in both preclinical and clinical FUS. A portion of that role is evaluating the outcomes of FUS procedures. Several MRI contrast mechanisms linked to FUS outcomes have proven critical in advancing the field including MR-thermometry, fMRI, gadolinium imaging, susceptibility-weighted imaging, and FLAIR imaging. MR-thermometry provides quantitative spatial maps of temperature changes. MR-thermometry works by taking advantage of the temperature dependence of proton resonant frequency (Rieke and Pauly 2008). MR-thermometry has been critical in prostate ablation and thalamotomy procedures where it provides both targeting and dosimetry feedback. Surgeons can accurately estimate ablated regions during the procedure, terminate the therapy once the ablation goal is met, and measure with a post therapy T2-weighted image to confirm ablated volume (Lipsman et al. 2013). Diffusion MRI is also now incorporated into MR-guided ablations, with tractography changes providing an additional level of information to plan and evaluate treatments (Krishna et al. 2019).

Functional MRI has also synergistically combined with FUS in the neuromodulation realm. fMRI provides contrast of oxygenated blood delivery via the blood oxygen level-dependent (BOLD) effect which is linked to neural activity and prioritization (Ogawa et al. 1990). By acquiring fMRI during US neuromodulation

procedures, BOLD changes due to neuromodulation can be spatiotemporally monitored. This has proven a fruitful combination in humans (Legon et al. 2012) and non-human primates (P.-F. Yang et al. 2018). fMRI + US enables measurement of both isolated and network scale neuromodulation effects. However, the low signal magnitude of the BOLD changes limits the spatiotemporal resolution achievable with adequate SNR.

Gadolinium imaging, susceptibility weighted imaging, and FLAIR imaging have all taken core roles in ultrasound BBB disruption. Gadolinium imaging uses t1-weighted hyperintensity in the presence of exogenously introduced gadolinium to measure BBB integrity (Ryken et al. 2014). Gadolinium imaging became popular for glioblastoma analysis where the BBB is often compromised in and around tumors and is an excellent tool for measuring BBB disruption caused by ultrasound. It is the only non-invasive method for measuring this disruption. Invasive methods include Evans blue histology (Chiueh et al. 1978) and imaging assays which measure the presence of a fluorescent biomarker delivered during the BBB disruption window (Szablowski et al. 2018).

Susceptibility weighted images (SWI) provide contrast on tissues' magnetic susceptibilities (Haacke et al. 2004). Of interest to FUS, SWI is used to check for hemorrhage which has been linked with excessive ultrasound dose during BBB opening procedures. Hemorrhage in these cases is long lasting and can be measured with SWI at time periods greater than months, sometimes with little change. A drawback of SWI is that healthy vasculature also shows as hypointensity. It can be difficult to ensure no hemorrhage in the event of BBB opening which occurs around vessels.

Fluid attenuated inversion recovery (FLAIR) imaging provides T2 contrast in which fluids are bright but with CSF signal suppressed (Hajnal et al. 1992). Edema occurs commonly in glioblastoma, brain surgery, and BBB opening therapies. FLAIR imaging provides good contrast for edema and is used to measure occurrences following BBB opening therapies. Edema in these cases is also linked to excessive pressure delivery but is typically temporary in nature.

2.3.2.2 MRI for guidance

MRI is also critical for guiding ultrasound procedures. MRI provides excellent soft tissue contrast in the brain, prostate, breasts, and liver which have been major target groups for FUS. Additionally, MR-ARFI and MR-thermometry sample displacement and temperature changes during sonications. These provide a spatial map of changes induced by the ultrasound that can readily be co-registered with high contrast soft tissue images such as t1-weighted images to guide placement of the focus or electronic steering of the focus. MR-ARFI measures displacement along a motion encoding gradient (MEG) (Nathan McDannold and Maier 2008). Tissue displaced along the gradient accumulates phase at a different rate than static tissue. MR-ARFI typically uses two equal magnitude, opposite polarity MEGs such that static tissue accumulates net-zero phase, while tissue displaced by acoustic radiation force from ultrasound accumulates phase proportional to displacement. Acoustic radiation force is proportional to spatial peak pulse average intensity (equation 2.16). Perfectly elastic tissue would experience displacement proportional to this force. Phase accumulation in MR-ARFI is proportional to net displacement and thus temporal average acoustic intensity.

MR-ARFI sequences are capable of detecting single micron displacement which is sufficient for detecting relatively low power, short (< 10 ms) FUS pulses (Nathan McDannold and Maier 2008). MR-ARFI therefore has the advantage over MR-thermometry in scenarios where heating is to be avoided such as non-ablative therapies (BBB opening and neuromodulation). MR-ARFI may also offer advantages in fatty tissue (Payne et al. 2020). MR-thermometry offers higher spatiotemporal resolution than MR-ARFI making it a better choice for ultrasound pulses which cause heating, such as ablative therapies. MR-ARFI requires higher pressure but lower duty cycle.

2.3.3 Optical tracking

Optical tracking has played a key role in the guidance of FUS. While MRI and CT provide unmatched deep tissue contrast in regions well suited for FUS, they greatly increase procedural cost and time. It has become common to acquire preoperative images for surgical planning and then use optical tracking in conjunction with these images for neuronavigation. In this scenario optical tracking provides the means to overlay the location of a transducer's focus on preoperative images in real time (V. Chaplin et al. 2019). Optical tracking has been used in research (S.-Y. Wu et al. 2018) and clinically (K.-T. Chen et al. 2020) for BBB opening procedures as well as for neuromodulation in large animals (P.-F. Yang et al. 2018; W. Lee et al. 2016). The accuracy of optical tracking varies from task to task and within FUS studies investigating this but has been reported as 2-3 mm (V. Chaplin et al. 2019; Wei et al. 2013).

In typical optical tracking, a stereovision infrared camera is used to track passive tools with multiple reflective spheres arranged to have unique vertices. The camera identifies the location and pose of several tools at once and streams this information in real time to a virtual serial port or similar interface where other applications can access the information. The locations and poses (Euler angles or quaternions) of the tools are in a coordinate system relative to either the camera itself or the coordinate system of a reference tool which is fixed relative to the subject. It is then simply a matter of transforming the preoperative images and the location of the FUS focus into the same coordinate system.

The transform between image space and camera or reference space is commonly inferred using fiducials which are visible in both the preoperative images and in the procedural room. By collecting the coordinates of each fiducial digitally in image space and physically with a tracked tool (stylus) the transform can be computed using point-based registration (Fitzpatrick, West, and Maurer 1998). The other necessary transform is that which informs the location of the transducer's focus relative to the transducer's tracker tool

coordinate system. Several methods exist for computing this transform including pivot calibration (H. Kim et al. 2012), surface fitting the transducer face using a stylus, and optically tracking a hydrophone (arrays only). We describe the optical tracking with a hydrophone technique in detail in section 4.7

Chapter 3

Ultrasound neuromodulation depends on pulse repetition frequency and can modulate inhibitory effects of tetrodotoxin

3.1 Abstract

Ultrasound is gaining traction as a neuromodulation method due to its ability to remotely and non-invasively modulate neuronal activity with millimeter precision. However, there is little consensus about optimal ultrasound parameters required to elicit neuromodulation and how specific parameters drive mechanisms that underlie ultrasound neuromodulation. We address these questions in this work by performing a study to determine effective ultrasound parameters in a transgenic mouse brain slice model that enables calcium imaging as a quantitative readout of neuronal activity for ultrasound neuromodulation. We report that (1) calcium signaling increases with the application of ultrasound; (2) the neuronal response rate to ultrasound is dependent on pulse repetition frequency (PRF); and (3) ultrasound can reversibly alter the inhibitory effects of tetrodotoxin (TTX) in pharmacological studies. This study offers mechanistic insight into the PRF dependence of ultrasound neuromodulation and the nature of US/ion channel interaction.

*This chapter is published in *Nature, Scientific Reports* (T. J. Manuel et al. 2020)

3.2 Introduction

Ultrasound neuromodulation (USN) is gaining traction as a non-invasive neuromodulation modality but little is known about how ultrasound affects neurons. Ultrasound can alter the behavior of the nervous system, and researchers have demonstrated these effects sporadically throughout the past century in

different *in vivo* and *ex vivo* preparations (Fry, Ades, and Fry 1958) (Mihran, Barnes, and Wachtel 1990). Since this time, researchers have routinely validated USN in animal models such as *in vivo* murine (W. Lee et al. 2018) (H. A. S. Kamimura et al. 2016), rabbit (S.-S. Yoo et al. 2011), sheep (W. Lee et al. 2016), and non-human primate (Folloni et al. 2019) . Researchers have recently found ultrasound stimulation of specific regions of the primate brain elicits responses in both the stimulated and connected regions (P.-F. Yang et al. 2018) (Deffieux et al. 2013). Ultrasound offers a potential therapy in these cases by enabling non-invasive modulation of specific brain circuit nodes that underlie diseases such as disorders of consciousness (Monti et al. 2016), chronic pain (Hameroff et al. 2013) and Alzheimer's disease (Beisteiner et al. 2019). For an in-depth review on USN results, mechanisms, and safety see Blackmore et al (Blackmore et al. 2019). Further information about the interactions of ultrasound with neurons will be crucial to fully leverage this therapeutic technology.

As ultrasound propagates through tissue it displaces particles and can potentially generate biological effects through mechanical or thermal effects (O'Brien 2007). At low mechanical indexes where diagnostic imaging occurs, the tissue is mostly unaffected and returns to its original state after the ultrasonic wave propagates. As the mechanical index is increased, the displacement can be large enough to generate direct mechanical effects or heat. Although heat is known to affect neural activity at the bulk and molecular scale (J. Wells et al. 2007) (Shapiro et al. 2012), USN is frequently observed using power levels that do not generate significant heat (< 0.1 °C) (Wattiez et al. 2017). We only explore pulses in this "non-thermal" regime in the present study.

There is increasing evidence that mechanical effects of ultrasound underlie neuromodulation, yet the discussion remains open. Ye et al. found that mechanical index correlates with response frequency wh *vivo* mice, directly linking particle displacement to USN (Ye, Brown, and Pauly 2016). A study in *c. elegans*

showed that mutants without thermal sensitivity responded to US while mutants without mechanical sensitivity did not (Kubanek et al. 2018). This mechanical effect may be manifesting via ion channels. Researchers observed ion currents in bi-layer preparations containing the Nav1.2 ion channel during sonication (Prieto et al. 2013). Nikolaev et al found that pyramidal neurons express stress activated cation channels which trigger action potentials when subjected to pressure (Nikolaev et al. 2015). In the Xenopous oocyte, ion channel current modulation dependence on US power has been reported (Kubanek et al. 2016). Prieto et al. showed activation of the Piezo1 channel by 43 MHz ultrasound and report acoustic streaming, or the displacement of fluid in the direction of ultrasound propagation, rather than particle displacement as the primary mechanism (Prieto et al. 2018). An alternative transduction mechanism excluding ion channels is that pressure-induced displacement of the lipid bi-layer generates action potentials (Krasovitski et al. 2011). By extending the Hodkin and Huxley model to include capacitance changes in the cell membrane due to ultrasound, Plaksin et al. created a model (Plaksin, Kimmel, and Shoham 2016) which matches well with *in vivo* observations of mouse motor cortex activation via ultrasound (King et al. 2013).

In implementing USN, several parameters can be varied for pulse design. These include fundamental frequency, duty cycle, pressure, and pulse repetition frequency (PRF). Since mechanisms remain unknown, researchers select parameters using empirical and ad hoc methods. An early study detailing the use of ultrasound for neuromodulation employed PRF in the kilohertz range (Tufail et al. 2011). Many studies have since chosen a similar repetition frequency in USN pulses presumably based on this work, but there is little physiological basis for introducing this pulsed scheme (King et al. 2013) (H. Kim et al. 2014) (Legon et al. 2014). King et al. did not find PRF to increase stimulation success, while others have noted that burst parameters elicit a strong off-target auditory effect which can confound the direct neuromodulatory effect (Guo et al. 2018) (Sato, Shapiro, and Tsao 2018). Yoon et al. conducted a thorough parametric study in sheep and found continuous ultrasound to perform worse than pulsed ultrasound for cortical and thalamic stimulation (Yoon et al. 2019). Other studies investigating USN in peripheral nerves show that tuning PRF

affects skin sensations and readouts from functional magnetic resonance imaging (fMRI) and electroencephalographic (EEG) data (Legon et al. 2012; W. Lee et al. 2014). As our understanding of direct neuromodulatory and off-target effects evolves, increased knowledge about the nature of mechanical stimulation is desirable to clarify the role of pulse repetition frequency and help us design pulses that are optimized for neuromodulation.

In order to improve our understanding of the ultrasound parameters that best modulate neurons, we quantified neuronal activity in an *ex vivo* brain slice model using a range of non-thermal ultrasound parameters. This manuscript describes the methods and experiments used to test USN parameters in a murine brain slice model using calcium imaging for activity measurement. These measurements are independent of artifacts from auditory pathway confounds as well as artifacts from ultrasound interacting with electrodes. We show direct observation of calcium signaling in response to ultrasound at parameters reported by others. Furthermore, we show dependence of USN on PRF, revealing that tuning PRF affects response rates. Using low concentration inhibition agents, we demonstrate that pulsed ultrasound reversibly affects ligand/channel kinetics, highlighting a potential mechanism that has not been previously considered. Our observations provide an important link between observations at the single cell and whole animal.

3.2 Methods

We used a calcium imaging brain slice model to optically measure intracellular calcium mobilization of genetically tagged neurons (T.-W. Chen et al. 2013) in response to ultrasound. Coronal brain slices containing the motor cortex were prepared from transgenic mice selectively expressing genetically encoded calcium indicator GCaMP6s in cortical pyramidal cells or all neuronal cells by crossing Cre-dependent GCaMP6s mice (JAX #024106) with CaMKIIα-Cre mice (JAX #005359) or Syn-Cre mice (JAX #003966),

respectively. Animals were housed under a 12-hour light/dark cycle with free access to food and water in their home cages. All procedures were approved by the Institutional Animal Care and Use Committee of Vanderbilt University and conformed to the guidelines established by the National Research Council, the *Guide for the Care and Use of Laboratory Animals.* In brief, mice (both male and female, 6-19 weeks of age) were anesthetized with isoflurane, euthanized, and decapitated. Brains were rapidly removed and submerged into oxygenated (95% O_2/5% CO_2), ice-cold NMDG-based cutting/recovery solution (in mM: 93 NMDG, 2.5 KCl, 1.2 NaH_2PO_4, 30 $NaHCO_3$, 20 HEPES, 25 $_D$-glucose, 5 sodium ascorbate, 2 thiourea, 3 sodium pyruvate, 10 $MgSO_4$, 0.5 $CaCl_2$; pH 7.3, 298-305 mOsm). Coronal slices (200-300 □m thick) containing the motor cortex were cut using a Leica VT1200S microtome (Leica Microsystems Inc, Wetzlar, Germany) and transferred into and incubated in a chamber containing the NMDG-based cutting/recovery solution aerated with 95% O_2/5% CO_2 at 32 °C for 8 min. Slices were then maintained at room temperature in a holding chamber containing artificial cerebral spinal fluid (aCSF) (in mM: 126 NaCl, 2.5 KCl, 1.25 NaH_2PO_4, 2 $CaCl_2$, 1 $MgSO_4$, , 26 $NaHCO_3$ and 10 D-glucose) for at least 1 hour until transferred to an imaging chamber superfused with oxygenated aCSF.

Experimental Setup

We developed an experimental apparatus capable of delivering ultrasound to a brain slice via a 1-inch spherically focused transducer (NDT, Huntington Beach, CA, USA) of either 250 kHz or 500 kHz (figure 3.1A) center frequency powered by an amplifier and function generator (A150, E&I, Rochester, NY, USA; Keysight, 33500B Santa Rosa, CA, USA)**.** Figure 3.1A was rendered using Solidworks (Solidworks Corp., Waltham MA). Sound was delivered through an agarose filled custom 3D printed acoustic reflection cone coupled through a Thermanox membrane (NUNC) and into an imaging chamber superfused with oxygenated aCSF (34°C). The cone was designed so that the propagation direction was not perpendicular to the microscope objective to reduce standing wave effects. The brain slices were held in place above the acoustically transparent membrane in the imaging chamber by a harp (Warner). The harp strings which are

40μm in diameter were positioned such that they were not within the field of view of the microscope and were thus not affecting the ultrasound path through the neurons being imaged. Fluorescent images were captured using an Olympus BX50WI upright fluorescence microscope equipped with a 10x water immersion objective (Olympus, Lake Success, NY). Blue light (470nm LED, Thorlabs Inc., New Jersey) was delivered through the 10x water immersion objective lens on the microscope. Clampex software (Molecular Devices, San Jose, CA) and HCImage Live (Hamamatsu, Japan) were used for triggering and image acquisition. A Hamamatsu ORCA-Flash4.0 LT digital camera (Hamamatsu, Japan) was used sampling at 6.5 μm per pixel and 2 frames per second with a 1.3 mm field of view.

On each day of experimentation, the acoustic reflector cones (one for each frequency tested) were filled with fresh agarose and allowed to set for one hour. The pressure output was measured for both cones by coupling the cone face to a waterbath and measuring pressure with a ceramic hydrophone (Onda, Sunnyvale, CA). The pressure maximum for each cone was marked by crosshairs on the cone face, which were used as a reference to accurately position the motor cortex of the brain slices in the imaging chamber. The uniformity of the acoustic intensity across the microscope field of view is shown for both cones in

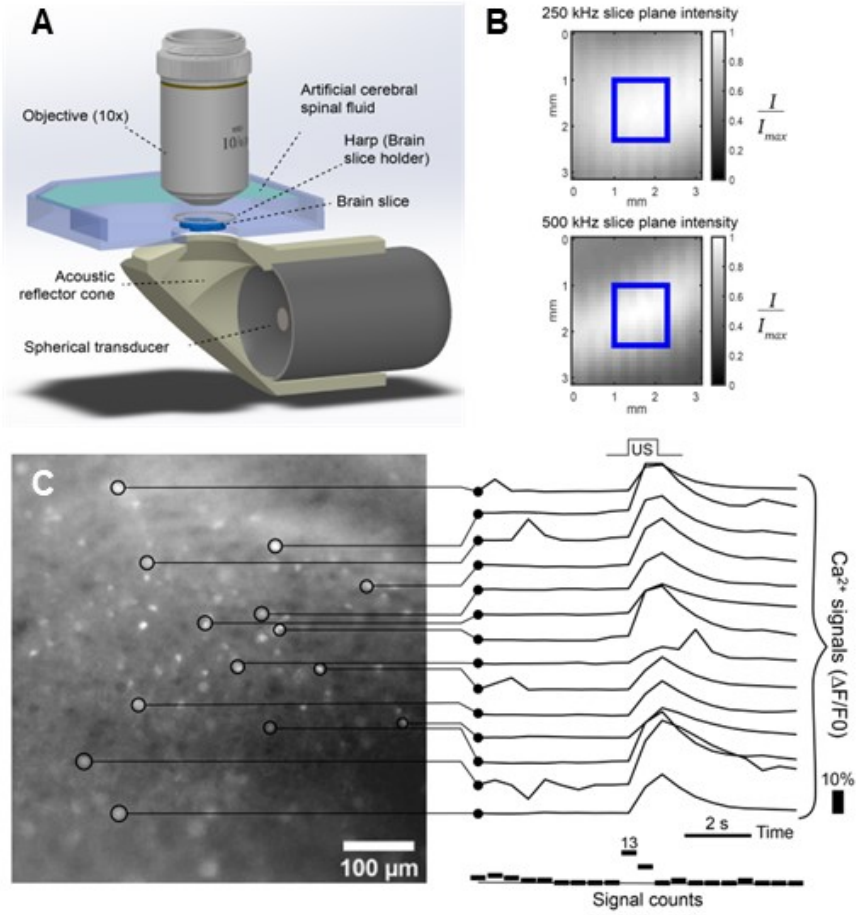

Figure 3.1. A) Experimental setup showing sonication from below while imaging from above. B) Relative acoustic intensity at the plane of the slice (blue square marks field of view of microscope, 1.3mm^2). C) Processing procedure showing Ca^{2+} signal traces for individual ROIs. Ca^{2+} images (left) taken at 2 frames per second (fps). Number of signal increases for each frame is shown below the traces. Response to US was determined by comparing signal rates between baseline frames and frames during and after US stimulation.

figure 3.1B. Temperature measurements were recorded once for each US parameter reported using a thermocouple (MAX31855, Adafruit, New York, NY USA) placed at the hotspot in the imaging chamber and read by an Arduino UNO (Arduino, Somerville, MA, USA).

Protocol for ultrasound calcium imaging trials

Slices were transferred to the imaging chamber and allowed to rest for 2 minutes prior to imaging. A 'single trial' is a measurement which includes calcium imaging during a baseline period and calcium images during a sonication period. For continuous wave experiments 30 seconds of images were acquired at 2 Hz with 20s baseline and 10s post sonication. For low duty cycle trials varying PRF, longer acquisitions were used with 40s of baseline followed by 120s post sonication. The minimum time between repeated trials was 30s.

Processing image sequences

The general processing approach is shown in figure 3.1C. Processing was done in MATLAB R2019a (MathWorks, Natick, MA) and ImageJ (Schneider, Rasband, and Eliceiri 2012). Each dataset was corrected for photobleaching by fitting an exponential model to the average intensity over time. Cell ROIS were selected manually using the ImageJ oval tool while visualizing the signal change ($\Delta F/F_0$) which allowed recording individual cells that were active during the entire observation window. These cell ROIs were loaded into MATLAB to generate fluorescent plots. An individual Ca^{2+} signal was defined as a change in an ROI's mean intensity by >1% over the span of 2 or less frames (1 second).

Continuous wave trials

The signaling rates for baseline frames and sonication frames were calculated by counting all signals within those frames and dividing by the number of frames. The signaling rate represents the calcium signals per time and allows quantification of calcium signaling increase during sonication. We ensured that slices were healthy by rejecting observations with low slice activity (< 0.2 signals per frame inclusive of baseline and post-sonication time frames). To account for the range of number of active cells and level of spontaneous activity exhibited in slices, a slice was considered as responsive to US if the signal rate increased by either 90% or 0.4 signals per frame compared to its baseline. Two metrics were used because a trial with few active cells and low baseline activity (~0.3 signals per frame) is unlikely to increase by 0.4 signals per frame, even given a response but is capable of a 90% rate increase. Conversely, a slice with many active cells and a high baseline activity (~1.5 signals per frame) may exhibit increases of 0.4 signals per frame given a response but will not increase by 90% as that would require a rate of 2.8 signals per frame.

Pulsed ultrasound trials

The trials investigating PRF differed from continuous wave trials in that they were lower duty cycle (2% total duty cycle and 60% burst duty cycle as opposed to 100% in continuous wave) and longer in duration (160s vs. 30s). A center frequency of 500 kHz and pressure of 100 kPa were used. Both pulsed parameters used a slow trigger at 0.5 Hz which activated the bursts 50 times per trial. To match duty cycle while varying PRF, pulse length (number of cycles) and number of pulses per burst were varied. The 1500 Hz pulses used 200 cycles per pulse (0.4 ms) and 100 pulses per burst. The 300 Hz pulses used 1000 cycles per pulse (2 ms) and 20 pulses per burst. Firing rates were grouped into time bins with 20 s duration. To account for variability in spontaneous activity from trial to trial, signaling rates were offset by the first baseline bin so that each bin represents the change in calcium signaling rate during the trial. The change in signaling is reported across all trials at each time bin (figures 3.3 and 3.4). To directly compare pulsed trials to continuous wave trials (figure 3.2), PRF pulses were analyzed using the same criterion for success as the continuous wave trials (signal rate increased by either 90% or 0.4 signals per frame compared to its

baseline). For consistency, only the 20s of baseline prior to sonication was included, and only 24 s of sonication was analyzed. 24 s of sonication with the pulsed parameters corresponded to 240 kilocycles which made the comparison between continuous wave (250 kilocycles) and pulsed trials as equal as possible.

TTX trials

In tetrodotoxin (TTX) trials, the same protocol was used as in pulsed US trials, except that TTX was introduced into the perfusing aCSF at 0 μM, 0.5 μM, or 1.0 μM to serve as a control, or to partially or fully block Na^{2+} channels. Three minutes were allowed for the TTX to diffuse throughout the imaging chamber before running trials. When TTX trials were repeated in a slice, 2 minutes of rest were given between pulses to allow the baseline to return to normal following sonication.

3.4 Results

Calcium signaling increases following ultrasound

Brain slices were sonicated with 8 continuous wave parameters with varying sonication frequency, pressure, and pulse length. Sample size (n) refers to number of trials where a trial comprises a baseline measurement, sonication measurement, and a rest period of 30s or greater. Two pulse lengths were tested for 250 kHz and 500 kHz with a matched number of cycles. The shorter pulse was 50 kilocycles of sound which corresponds

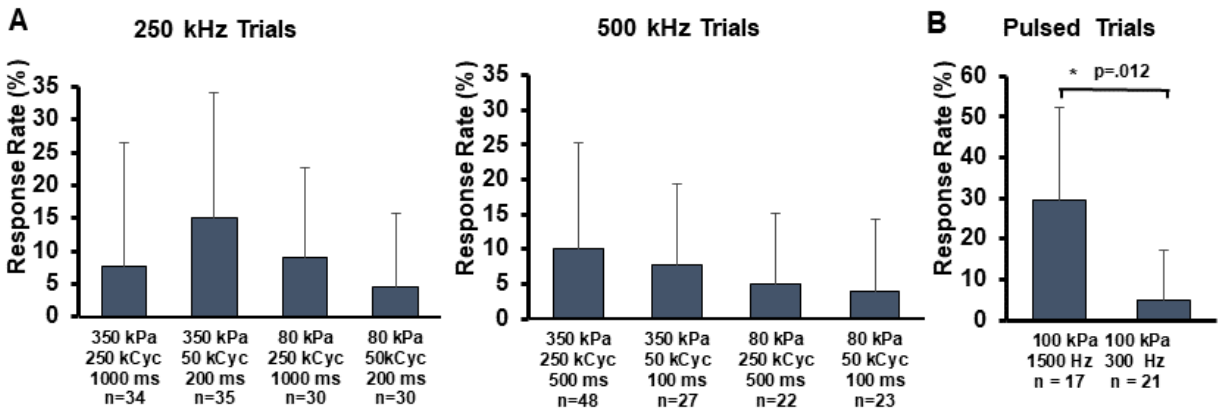

Figure 3.2. Response rates for all investigated parameters reporting average and standard deviation across slices. A) 250 and 500 kHz continuous wave trials varying pressure and pulse duration. Pulse duration is half for 500 kHz trials because the number of pressure cycles were matched across frequency. B) 500 kHz pulsed ultrasound trials at 1500 Hz and 300 Hz PRFs with duty cycle, intensity, and frequency matched. See figure 3.3 for pulsed parameter details. kPa: kilopascals (pressure); kCyc: kilocycles (number of pressure cycles). * student's paired t-test

to 200 ms and 100 ms for 250 kHz and 500 kHz respectively. The longer pulse was 250 kilocycles which is 1000 ms and 500 ms for 250 kHz and 500 kHz sound respectively. We matched the number of cycles to account for frequency dependent differences in thermal deposition between 250 kHz and 500 kHz. Continuous wave ultrasound increased calcium signaling in brain slices in 19 out of 221 total trials (8.5%) across 53 slices (figure 3.2A). For the continuous wave parameters examined (80 kPa & 350 kPa and 50 kilocycles & 250 kilocycles), the response rate was less than or equal to 15%. Among these parameters, 200 ms 350 kPa 250 kHz pulses showed the highest average response rate across all slices (5 out of 33 trials, 15%) but this was not statistically significant compared to the other parameters. Brain slices were sonicated with two pulsed ultrasound parameters with duty cycle, intensity, and transmit frequency held constant and pulse repetition frequencies (PRF) of 1500 Hz and 300 Hz (figure 3.2B). When analyzing these trials using the same criteria for continuous pulses over a time frame encompassing a matched number of ultrasound cycles, we found that the response rate was 29% and 5% for 1500 and 300 Hz PRFs respectively ($p = .012$, Student's t-test).

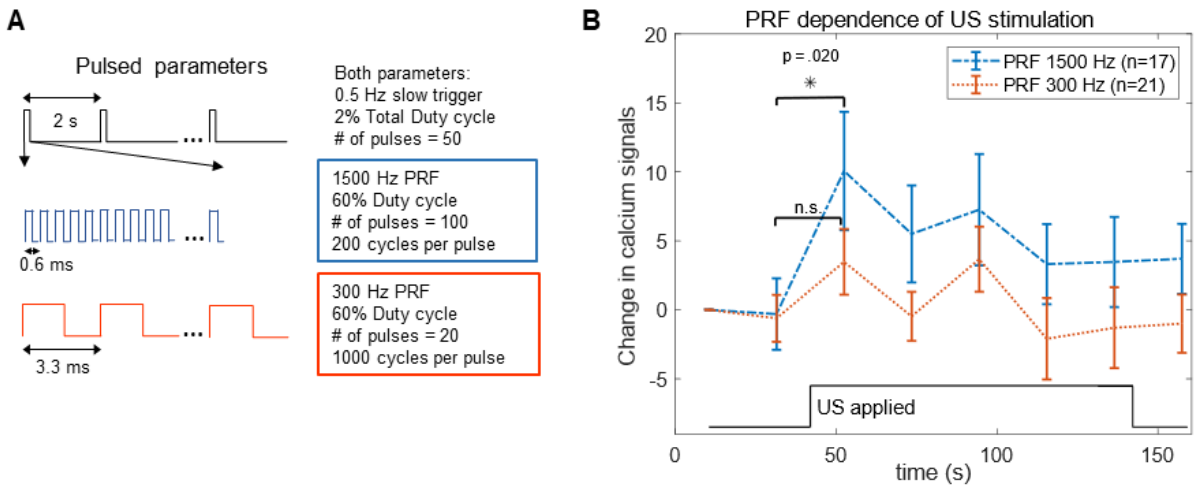

Figure 3.3. Pulse repetition frequency (PRF) affects calcium signaling rates. A) US parameter details. A slow trigger at 0.5 Hz which fired 50 times was used for both parameters. This trigger activated the two PRFs shown in blue and red which varied in pulse length and number of pulses to enable matched duty cycle. B) Calcium signaling at two PRFs with duty cycle and power matched. Only PRF 1500 Hz in the time bin immediately following US onset shows significant increase from baseline signaling (*p=0.02, student's paired t-Test). Data are presented as mean ± SEM. (n.s. not significant)

Neuronal response is PRF dependent

To investigate the effect of pulse repetition frequency (PRF) on neuronal responses, slices were sonicated at two PRFs with duty cycle, intensity, and transmit frequency matched (figure 3.3). We chose 1500 Hz PRF with 500 kHz frequency because similar parameters have elicited measurable responses in humans and non-human primates along with minimal induced heating (P.-F. Yang et al. 2018; Legon et al. 2014; Legon, Ai, et al. 2018). 300 Hz PRF has been previously reported to be less effective than 1500 Hz in mice (King et al. 2013) but equally effective in C. elegans (Kubanek et al. 2018). The duty cycle was 60% during bursts and 2% for the total sonication which includes inter-burst intervals. The total sonication time was 100 s (50 bursts, 0.5 Hz). 1500 Hz PRF resulted in an increase in calcium signaling from the baseline (p=.02, student's t-test) for the time point immediately following US onset. No timepoints from 300 Hz trials showed statistically significant change from baseline. At each timepoint during sonication, 1500 Hz

trials induced a greater change in calcium signals than 300 Hz trials. These differences were not statistically significant ($p >= 0.13$). Duty cycle, intensity, and transmit frequency were held constant because they have each been shown to affect US neuromodulation (Ye, Brown, and Pauly 2016; King et al. 2013; Yoon et al. 2019).

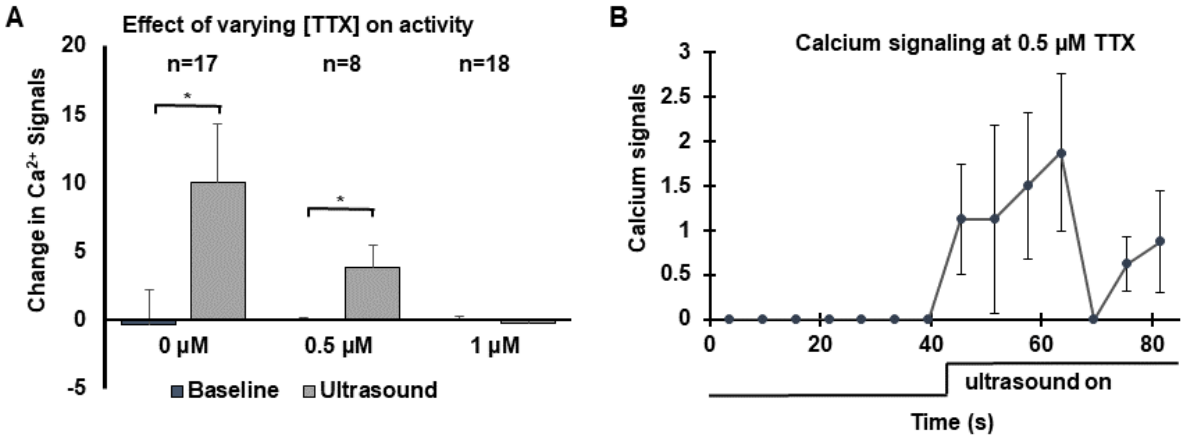

Figure 3.4. (A) Change in calcium signaling during ultrasound with three concentrations of the voltage-gated sodium channel blocker, TTX. At 0.5 µM TTX, ultrasound temporarily reduces the inhibitory effect of TTX. (*$p < 0.05$, student's paired t-test). (B) Calcium signals vs. time at 0.5 µM TTX showing reduction of TTX inhibition during ultrasound (n=8). All data are presented as mean +/- SEM.

Ultrasound modulates ion channel interactions

Application of 1 µM TTX eliminated baseline spontaneous as well as US-induced calcium mobilization (figure 3.4). At a reduced concentration of 0.5 µM TTX, baseline calcium signals were eliminated, but US induced calcium signaling. During 0.5 µM TTX tests, we measured two brain slices with 4 observations in each slice and two minutes of rest between trials. Increased Ca^{2+} signaling in the presence of 0.5 µM TTX only occurred during sonication and returned to baseline after sonication. As a positive control, we compared spontaneous baseline activity between no TTX and 0.5 µM TTX, with the expected outcome

being suppression of calcium signaling at 0.5 μM TTX. In the absence of TTX, calcium signaling during baseline was 1.1 signals per second compared to 0.0 signals per second for 0.5 μM TTX ($p=0.0007$, student's t-test). Pulsed ultrasound was associated with increased Ca^{2+} signaling at the 0.5 μM concentration of TTX that fully blocked Ca^{2+} signaling at baseline.

USN pulses generated limited heat and displacement

Beam maps reporting relative acoustic intensity measured in a waterbath at the face of both reflector cones had uniform pressure within the microscope field of view. For continous wave pulses used in figure 3.2, heating from acoustic absorption was less than 1 °C at the maximum pressure and pulse duration used. For pulsed ultrasound, heating was less than .25 °C. There was no detectable change in image intensity due to displacement from the acoustic radiation force imparted on the brain slices for parameters reported in this study.

3.5 Discussion

USN has been demonstrated in multiple experimental models, but there are many confounds that can make interpreting experimental outcomes challenging. Our study demonstrates direct USN in a brain slice model using optical imaging for feedback. By using genetically targeted optical methods to image neural activity, our reported measurements are isolated from off-target effects or other known artifacts. We report overall success rates using non-thermal parameters known to elicit neuromodulation in various animal models and demonstrate that USN is PRF dependent and capable of modulating ion channel interactions with pharmacological agents. Our observations provide an important link between single cell experiments and work in fully intact brains.

Optical readouts avoid potential confounds

Using optical methods to assess neural responses to ultrasound avoids potential confounds created by the presence of an electrode. Traditional electrophysiology is challenging in the presence of ultrasound because electrodes are typically small metal probes which are highly absorbing and scattering as reported by Morris et al (H. Morris et al. 2008). When an ultrasound pulse propagates, it generates a force that is proportional to the absorption (α) of the propagating medium and intensity (I) of the pulse given by:

$$F = \frac{2\alpha \mathrm{I}}{c} \tag{3.1}$$

with c as the speed of sound in the media (Nightingale 2011). At non-thermal ultrasound pressure used for neuromodulation, this force is on the order of $\mu N/cm^3$ to mN/cm^3 in brain tissue, but the addition of a highly absorbing and scattering electrode causes a stronger force to be imparted. The induced motion of the electrode would result in both viscous and absorptive heating (H. Morris et al. 2008) amplifying the mechanical effects of ultrasound and confounding any measurements. Electrodes can also result in standing pressure waves which alter the distribution of pressure and radiation force in surrounding tissue (Menz et al. 2019). Ultrasound-induced artifacts have also been reported in patch clamping methods using glass pipette electrodes due to a disruption of the connection between the tissue and probe (Tyler et al. 2008). Optical imaging, as used in our study, mitigates these confounds present in electrophysiology, although we note that radiation force interactions in the slice preparation differ from the intact brain in two main ways. When used at sufficient pressure, the acoustic radiation force can displace the tissue slice out of the focal plane, generating false positive readings. The pressures used in our study did not displace the tissue by a detectable amount. Acoustic streaming is the displacement of fluid in the direction of ultrasound propagation. In our slice preparation, which is acoustically similar to Prieto et al., acoustic streaming directly at the Thermanox layer would be zero and increase with increasing distance away from the Thermanox layer (Prieto et al. 2018). Streaming at the slice location (directly above the Thermanox) was

not strong enough to generate detectable displacement at pressures used in our study. However, the overall fluid dynamics of acoustic streaming likely differ between the brain slice and intact brain. Models of acoustic propagation in the brain that incorporate this effect do not exist and would improve our understanding of streaming in the intact brain.

Optical tracers for readouts within the ultrasound pressure field remain the most non-invasive and essential tool for USN measurements. For this reason, Lee et. al have developed a system for optical readouts while sonicating co-cultured neurons and astrocytes (J. Lee et al. 2019). Other groups are using optical tracers *in vivo* including Han et al. who showed that ketamine blocks USN in *in vivo* cortical neuron activity using calcium imaging with indicator OGB-1 AM (Han et al. 2018) and Sato et al. who used wide-field cortical imaging with GCaMP6s to monitor US neuromodulation *in vivo* but report no observation of direct US neuromodulation (Sato, Shapiro, and Tsao 2018). The isolated brain slice in our study targeted GCaMP6s in a similar manner but shows direct neuromodulation from ultrasound.

Direct neuromodulation in the absence of auditory confounds

The ability for ultrasound to elicit audible sensations in humans was reported in studies as early as 1950 (Pumphrey, 1950). The precise mechanism through which ultrasound activates the auditory system is not fully understood and is hypothesized to involve mode conversion of the ultrasonic wave into shear waves within the bone (Clement et al. 2004) or coupling through the cochlear fluid (Guo et al. 2018). A prior study in the intact mouse reported no evidence of direct stimulation with widefield calcium imaging during transcranial stimulation of mice expressing GCaMP6s proteins in neurons bearing the Synapsin I promoter (Sato, Shapiro, and Tsao 2018). We used similar genetic targeting to this prior work but observed direct effects that were not observed in the intact animal. We hypothesize that Sato et al. observed a combined effect of direct USN and auditory effects but that direct effects were either combined with auditory effects

or below the detection threshold of the *in vivo* optical system, which would primarily be sensitive to cortical activation in the living animal. This interpretation is consistent with *in vivo* studies in genetically deafened mice that demonstrate motor responses from transcranial ultrasound (Mohammadjavadi et al. 2019).

Role of pulse repetition frequency

Continuous and pulsed wave ultrasound have been shown to elicit a wide range of neuromodulatory effects in a variety of animal models (for reviews see Tufail et al. (Tufail et al. 2011) and Blackmore et al. (Blackmore et al. 2019)). The use of pulsed bursts in the kilohertz range generates acoustic waves capable of generating auditory brainstem response in mice, which can be mitigated by using smooth amplitude windows for the modulatory wave to reduce audible frequency components (Mohammadjavadi et al. 2019). The inclusion of a pulsed repetition frequency compared to continuous ultrasound was not a strong indicator for modulation success in a mouse study measuring motor responses to modulation of the motor cortex (King et al. 2013). However in *c. elegans*, Kubanek et al. (Kubanek et al. 2018) reported maximum frequency of motor responses at PRF's between 300 Hz and 3 kHz and 50% duty cycle using 10 MHz ultrasound. In a study sonicating the motor cortex of rats, Kim et al. (H. Kim et al. 2014) report that pulsed ultrasound elicits responses at lower acoustic intensities thresholds than continuous wave ultrasound (PRFs up to 2 kHz with varying duty cycle were investigated). Our results agree with these findings, as we report that 1500 Hz PRF low pressure, pulses with 60% intra-burst duty cycle and 2% total duty cycle is effective.

It is interesting to consider the temporal aspects of tissue displacement during pulsed ultrasound. With the 1500 Hz PRF, 200 cycle, 500 kHz, pulses used in this study, the relaxation time between single pulses is 260 µs. Using Viscoelastic Response (VisR) imaging (Selzo and Gallippi 2013), an acoustic radiation force based elastography method which employs multiple displacement pulses to infer mechanical properties of tissue, a relaxation time of 240 µs is employed between pulses to allow for partial tissue relaxation. Their

model shows that tissue relaxation occurs at timescales similar to the off periods of PRFs which have incidentally become popular in USN. With tissue relaxation occurring in the off time of these pulses, it follows that tuning PRF and duty cycle is equivalent to tuning the displacement and relaxation dynamics of sonicated tissue. If ARF induced displacement is the predominant transduction mechanism for USN – as suggested in (Menz et al. 2019) – it follows that tuning the temporal displacement profile could result in varied response rates due to ultrasound. In our study, pulsed ultrasound at a PRF of 1500 Hz exhibited robust response. The mean change in calcium signals was higher in every sonication time bin compared to 300 Hz PRF, with duty cycle and pressure held constant. The use of pulsed ultrasound enables neuromodulation at low duty cycles, making it a desirable candidate for *in vivo* applications where heating from absorption should be minimized.

Continuous wave trials showed low response rates

The response rates across continuous wave trials were low (<15 %) and less robust than pulsed ultrasound in this model. When analyzing pulsed ultrasound trials with the same protocol used for continuous wave pulses, the 1500 Hz PRF pulse resulted in 29% response rate at lower pressure (100 kPa in pulsed trials versus 350 kPa in continuous wave trials). This metric only included the 24 s following the onset of ultrasound in pulsed trials to keep the total amount of pressure cycles delivered comparable (250 kilocycles in continuous wave trials, 240 kilocycles in pulsed trials). The response rate is much lower than what is reported in *in vivo* murine models where motor responses >80% were found for very similar US parameters (500 kHz 80 ms pulses at 300 kPa or 2.9 W/cm^2 I_{SPTA}) (Mohammadjavadi et al. 2019). Factors inherent to our experimental design may have contributed to these low response rates. The magnitude of the calcium response must be high enough to distinguish spontaneous activity from US induced activity. Tissue scattering limits the depth of the 300 μm thick brain slice which is resolvable by the microscope, meaning only neurons in the top portion of the slice contribute to measured signals. The number of neurons exposed

to the US is inherently lower in the slice than *in vivo* given that the slice occupies only a small portion of the US focus as opposed to *in vivo,* where the entire sound focus may interact with a large population of neurons in brain tissue. A similar explanation relating exposure volume to stimulation is offered in both Ye et al. (Ye, Brown, and Pauly 2016) and Menz et al. (Menz et al. 2019) Furthermore, several *in vivo* studies explore higher pressure regimes for USN. In our model pulses above 350 kPa often resulted in slice motion which limited our ability to explore higher pressure.

Inhibitory effects of low concentration TTX on calcium mobilization are temporarily reduced by pulsed US

Our model demonstrated a complete blocking of baseline calcium signaling at 1uM TTX and a lack of response to ultrasound at that concentration. This agrees with the findings of Tyler et al. (Tyler et al. 2008) who showed at 0 to 100 Hz PRF, 440 kHz US that 1 μM TTX suppressed US stimulation and Lin et al. (Z. Lin et al. 2018) who demonstrated inhibition in the presence of continuous wave 27 MHz US with 0.1 μM TTX in pyramidal cells of rat brain slices using whole-cell patch-clamp recordings. These findings suggest that US stimulates neurons through a transduction pathway influenced by voltage-gated Na^{2+} channels. Voltage-gated Na^{2+} channel conductivity has been shown to increase with mechanical deformation (C. E. Morris and Juranka 2007), providing a potential mechanism for US ion channel interaction. Gaub et al. found that mechanical deformation of neurons with pressures greater than 6 kPa resulted in increased calcium signaling in cultured cortical and hippocampal mouse cells expressing GCaMP6s and suggest sub-traumatic pressures applied to neurons evoke neuronal responses via gating of ion channels (Gaub et al. 2020). Unique to our results, a concentration of 0.5 μM TTX suppressed the baseline level of calcium signaling, but US still induced calcium mobilization. In these trials, ultrasound temporarily reduced the inhibitory effect of TTX. We hypothesize that ultrasound reversibly alters the inhibitory effects of TTX at 0.5 μM with voltage-gated Na^{2+} channels of pyramidal cells.

3.6 Conclusion

Pulsed ultrasound at a PRF of 1500 Hz increased calcium signaling in neurons, confirming the efficacy of this parameter and that low duty cycle low intensity ultrasound can be used to directly excite neurons. Pulsed ultrasound is more effective for USN than continuous wave ultrasound in this model. This finding is encouraging for transcranial applications where pulsed ultrasound is conducive for higher pressure and lower tissue heating. Our findings offer further insight into sodium channel involvement in US neuromodulation by demonstrating that US can reduce the inhibitory effect of TTX on voltage gated sodium channels.

Chapter 4

Design of a 1-MHz therapeutic ultrasound array for small volume blood-brain barrier opening at cortical targets in macaques

4.1 Abstract

Focused ultrasound (FUS) can temporarily open the blood brain barrier (BBB) and increase the delivery of chemotherapeutics, viral vectors, and other agents to the brain parenchyma. To limit FUS BBB opening to a single brain region, the transcranial acoustic focus of the ultrasound transducer must not be larger than the region targeted. In this work, we design and characterize a therapeutic array optimized for BBB opening at the frontal eye field in macaques. We used 115 transcranial simulations in four macaques varying f-number and frequency to optimize the design for focus size, transmission, and small device footprint. The design leverages inward steering for focus tightening, a 1 MHz transmit frequency, and can focus to a simulation predicted 2.5 ± 0.3 mm lateral and 9.5 ± 1.0 mm axial full-width at half maximum spot size at the frontal eye field without aberration correction. The array is capable of steering axially 35 mm outward, 26 mm inward, and laterally 13 mm with > 50% the geometric focus pressure. The simulated design was fabricated, and we characterized the performance of the array using hydrophone beam maps in a water tank and through an ex vivo skull cap to compare measurements with simulation predictions. We describe a method for integrating the array transducer into a magnetic resonance guided FUS system with optical tracking validated by magnetic resonance thermometry. The transducer produced by this design process is optimized for BBB opening at the frontal eye field in macaques.

*This chapter is under review and available as a preprint (T. Manuel, Phipps, and Caskey 2022)

4.2 Introduction

The blood-brain barrier (BBB) is a selectively permeable membrane that presents an obstacle for the treatment of neurological disorders by keeping many therapeutic molecules from entering the brain. Focused ultrasound (FUS) in combination with circulating microbubbles can temporarily disrupt the BBB, allowing for localized delivery of therapeutic agents which would otherwise not reach the parenchyma. Circulating microbubbles interacting with the acoustic focus temporarily increase the permeability of the BBB through a mechanical interaction (Hynynen et al. 2001). FUS BBB opening (BBBO) extends brain therapeutic options to include viral vectors (C.-Y. Lin et al. 2016; H. Li et al. 2021), nanoparticles (Ohta et al. 2020), neurotrophic factors (Samiotaki et al. 2015), antibodies (Kinoshita et al. 2006), chemotherapy agents (Idbaih et al. 2019), and others. Sonication parameters required for transport of molecules 2,000 kDa or larger may pose risk of permanent damage (H. Chen and Konofagou 2014). The safety of FUS BBB opening has been demonstrated in Macaques (Pouliopoulos et al. 2021; N. McDannold et al. 2012) and humans (Lipsman et al. 2018; Carpentier et al. 2016).

FUS BBBO has transitioned from the proof-of-concept stage to deployment in studies with physiological indicators of success. FUS BBBO was shown in preclinical studies to enhance the concentration and effect of chemotherapeutics in glioblastomas (Treat et al. 2012; F.-Y. Yang et al. 2012) which propelled it to use in 13 clinical trials as of June 2022 (for clinical summary, see Roberts et al. 2022 (J. W. Roberts et al. 2022)). FUS BBBO has applications beyond drug delivery. FUS BBBO can facilitate viral vector-based gene therapy (Thévenot et al. 2012) which has been applied in a mouse model to encode a G-protein-coupled receptor that responds to systemically administered designer compounds providing spatiotemporal modulation of neural circuits (Szablowski et al. 2018). The size of the acoustic focus is a key factor in FUS BBBO study designs. In glioblastoma studies, large treatment volumes are needed to match the tumor size and often require electronic steering to cover a range of tissue. In gene-therapy studies aiming to transfect

a specific brain region, the ideal focal volume is small, matching the size of the targeted brain region.

We set out to design a transducer with a small focal volume capable of BBBO in macaques at cortical targets. We specifically focused on the frontal eye field (FEF), a common candidate in research for its known functions in visual processing. The macaque FEF is in the frontal lobe along the anterior border of the arcuate fissure, corresponding to Brodmann's area 8 (Vernet et al. 2014). Relative to the approach angle a transducer can take relative to the skull, FEF is 1 cm in depth at its largest approach and has widths varying from 3 to 9 mm. Based on these values, we set a focal spot size of 3 x 10 mm (pressure, full-width at half-maximum) as the goal with sufficient beam steering range (± 5 mm) to span the volume of the target. Beam steering enables spanning the target with iterative sonications at multiple locations.

Prior works have established general guidelines for therapeutic array design. Multi-element arrays were introduced for their steering capabilities as well as the ability to correct for skull induced aberration (Clement et al. 2000). Near-field pressure and secondary maxima around the focus can be reduced by placing elements about a spherical surface (E.S. Ebbini and Cain 1991). Trade-offs for element distribution are also well described. Periodic arrangement of elements results in larger grating lobes in the focal plane (Pernot et al. 2003; Stephens et al. 2011), which led to the adoption of random and spiral element distributions, both of which reduce secondary maxima. Spiral distributions provide higher coverage which increases focal gain (Ramaekers et al. 2017). Random arrays offer improved off-axis steering and grating lobe reduction if some coverage can be sacrificed. Sparse arrays offer decreased element count with minimal performance degradation around the natural focus but at the cost of increased near-field energy deposition (Ellens et al. 2011).

These design works used simulations in homogenous media to outline the tradeoffs of element distribution, radius of curvature, aperture, and frequency on transmission, spot size, steering, and off-target pressure.

The performance of transducers in the skull is further complicated by absorption, reflection, and aberration as the sound travels through material with greatly differing acoustic impedance and absorption. Furthermore, a transducer's performance will vary with targets across the brain due to skull geometry. This has been measured experimentally with MR-thermometry in a study evaluating the treatment envelope of a transducer throughout a lamb brain (Odéen et al. 2014).

These effects from the skull have been incorporated into transducer design by using models of acoustic propagation in heterogenous media. A modified multi-layered skull ray tracing model was used to investigate the feasibility of transcranial passive acoustic mapping with sparse hemispherical arrays (Ryan M Jones, O'Reilly, and Hynynen 2013). The performance of skull-conforming arrays were compared with hemispherical arrays for a range of human brain targets using a combination of ray-tracing and finite-element modeling (Adams et al. 2021). A transducer for multiple foci in non-human primates featuring an imaging array insert was optimized using a k-space pseudo spectral model (Rebecca M. Jones et al. 2022).

Designing a transducer for BBBO has unique physical considerations apart from arrays designed for thermal ablation. BBBO requires lower acoustic power than thermal ablation with in-situ pressure requirements below 1 MPa and at low duty cycle, 10 ms bursts (pulse repetition frequency 2 Hz or less). Large area, high transmit power arrays which are critical for thermal ablation are not necessary for BBBO. Additionally, the interaction between the therapy pulse and the circulating microbubbles is frequency dependent with lower frequency sound resulting in cavitation at lower pressures. 200-500 kHz sound is typically used for BBBO but frequencies up to 8 MHz have been shown to increase permeability in small animal models (Bing et al. 2009). Because the focal volume decreases with increasing frequency for a given transducer, we explored frequencies up to 1.5 MHz, which is higher than typically used in medium to large animal and human transcranial procedures.

In this work we optimized a transducer design using transcranial simulations with the primary objective of

generating a small focus (3 x 10 mm) at the frontal eye field through the macaque skull. A second practical objective was to limit the size of the transducer to reduce three features: i) the required area of skull access in transcranial procedures where space is often limited ii) the degradation of MRI image quality due to the amount of transducer and coupling material present iii) inconvenience with mechanical steering due to transducer bulkiness. Building upon prior array design efforts, we simulated Fermat spiral arrays to improve coverage which reduces near-field pressure particularly with inward steering. To account for inter-subject variability, all candidate models were simulated through four macaque skulls. Following fabrication by a commercial manufacturing house, we characterized the performance of this array in a water bath and through an *ex-vivo* skull cap.

4.3 Methods

Study design and parameter space justification

The transducer design was informed by acoustic simulations performed in k-Wave, a MATLAB toolbox (Treeby and Cox 2010). There were several initial considerations which constrained the range of transducer designs simulated. We bound the frequencies to be simulated between 0.2 and 1.5 MHz. Frequencies below 0.2 MHz will produce large focus sizes and frequencies above 1.5 MHz will have lower transmission and increased aberration through the skull. We set the element size to 3.5 mm diameter, which was the maximum size that fit on all f-number models. We wanted a design suitable for small cortical targets which added geometric constraints. Furthermore, we sought to limit the size of our design. Large, low f-number arrays are expensive and can be challenging to manufacture, and their bulkiness can degrade MRI image quality for sensitive measurements like functional MRI and MR acoustic radiation force imaging (MR-ARFI). Large arrays require access to more skull, which is often unavailable in research settings due to additional hardware on the head. With these considerations in mind, we limited simulated array geometries

that included f-numbers between 0.6 and 1.2 and diameters from 42 to 80 mm. We fixed the focal length at 50 mm which was the minimum focal length to provide sufficient room between the aperture and head for coupling at all f-numbers considered while reaching FEF. We simulated Fermat spiral arrays to improve coverage and transmit power on our relatively small area array while also reducing secondary maxima and near-field pressure.

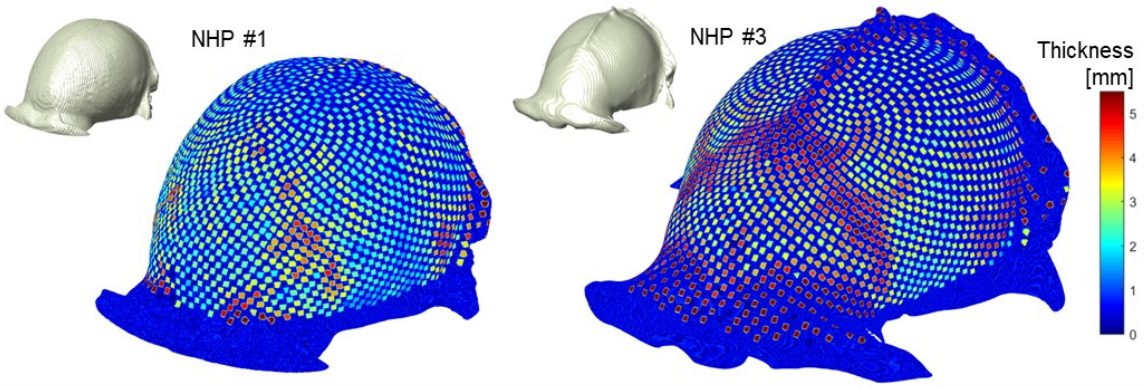

NHP #	Sex	Thickness [mm]	Density [kg/m^3]	Max Density [kg/m^3]	Volume [mm^3]
1	F	2.9 ± 1.1	2323 ± 200	2712 ± 244	15300
2	F	3.5 ± 1.6	2239 ± 94	2562 ± 118	15600
3	M	4.2 ± 2.0	2040 ± 152	2296 ± 182	29600
4	M	4.1 ± 2.1	2007 ± 121	2242 ± 151	21900

Figure 4.1. Comparing skull properties for the four macaques used in simulations. Properties were measured by analyzing skull voxels along ray paths between transducer elements and the focus for a transducer with 2048 elements. **(Top)** Thicknesses overlayed on skull surface at each ray path intersection for NHP # 1 and 3. **(Bottom)** Properties for NHP #1-4 (average across rays ± standard deviation).

Justification for simulating through multiple skulls

The goal of simulations was to identify how transmission through the skull and focal spot size changed with different designs, and to identify a design which balanced tradeoffs between these metrics. Skull thickness and density varies on an individual basis, and we wanted to capture this in our simulations to avoid overfitting a design to one monkey. To accomplish this, we simulated all designs in two female and two male macaque subjects with average skull thicknesses ranging from 2.9 to 4.1 to mm. Figure 4.1 shows

skull properties of our subject population measured by ray tracing through the skull from elements of a hypothetical array. The 3D renderings illustrate the thickness at each ray intersection point to highlight spatial variances. The table shows average ± standard deviation values from measures combined across all rays.

Simulation details

We collected computed tomography (CT) scans of four macaques (0.6 x 0.6 x 0.8 mm voxels) and used these scans to populate simulation mediums. Speed of sound and density were computed from Hounsfield units (HU). First a skull mask was created by thresholding the CT image at values above 600 HU. Density of voxels within the skull were estimated from HU by referencing the HU of water and air (Connor, Clement, and Hynynen 2002; Pichardo, Sin, and Hynynen 2011) given by:

$$\rho = k_1 HU + k_0 \tag{4.1}$$

$$k_1 = \frac{\rho_w - \rho_{air}}{H_w - H_{air}} \quad \text{and} \quad k_0 = \frac{-\rho_w H_{air}}{H_w - H_{air}} \tag{4.2}$$

with ρ as density, ρ_w density of water, ρ_{air} density of air, H_w HU of water, and H_{air} HU of air. Speed of sound was estimated by first estimating bone porosity φ:

$$\varphi = 1 - \frac{HU}{\max(HU_{volume})} \tag{4.3}$$

and then estimating the speed of sound (Aubry et al. 2003):

$$c = (c_{Max} - c_{min})(1 - \varphi) + c_{min} \tag{4.4}$$

Values used were c_{Max} 3100 m/s, c_{Min} 1480 m/s, ρ_w 997 kg/m^3, ρ_{air} 1.225 kg/m^3, H_w 0, H_{air} -1000. To model absorption, a value of 0.2 dB/MHz/cm was used for all non-skull voxels and 8.1 dB/MHz/cm was used for skull (Pinton et al. 2012). Simulations which use phase-only abberation correction use a simulated time-reversal with a point target source at the transcranial target to extract phases. In the phase-extraction simulation, element centers are set as sensors and record the pressure time series, $p(\mathrm{t})$, for the simulation. The phase, α, of $p(\mathrm{t})$ for each element is extracted with respect to the transmit frequency f_0:

$$I = \sum_{0}^{T} p(\mathrm{t}) cos(2\pi f_0 t) \tag{4.5}$$

$$Q = \sum_{0}^{T} p(\mathrm{t}) \sin(2\pi f_0 t) \tag{4.6}$$

$$\alpha = arctan\left(\frac{Q}{I}\right) \tag{4.7}$$

We do not use total time reversal (as in (Aubry et al. 2003)) because our generator is unable to produce arbitrary waves. We note that simulating both the inverse and forward problem with the same numerical model (known as inverse crime) will produce idealized focusing compared to what is achievable in practice. Simulations which used steering without phase correction generated phases with a Rayleigh-Sommerfeld inversion technique described by Ebbini and Cain (E.S. Ebbini and Cain 1989).

Generating transducer models

We developed a workflow between 3D-Slicer (http://www.slicer.org/) and MATLAB to set up simulation inputs for k-Wave. A custom MATLAB script was developed which creates a model of a transducer given the inputs of number of elements, element size, aperture, and focal length. For Fermat spiral arrays with the golden angle, we found the element distribution iteratively. We started by populating a sphere of radius

equal to the desired geometry with elements distributed along a Fermat spiral. The coordinates (x, y, z) for this distribution were given as:

$$x = \cos(\theta)\sin(\phi), y = \sin(\theta)\sin(\phi), z = \cos(\phi) \tag{4.8}$$

$$with\ \theta = m\pi\left(1 + \sqrt{5}\right), \qquad \phi = cos^{-1}\left(1 - \left(\frac{2m}{n}\right)\right) \tag{4.9}$$

$$n = no.of\ elements, and\ m = (0:1:n-1) + 0.5 \tag{4.10}$$

We cropped the sphere of distributed points to only include a spherical cap of aperture equal to the desired transducer and checked the number of points which lie on this cap. By iteratively changing n until 128 elements lie on the cap, a Fermat spiral with golden divergence angle distribution was achieved for 128 elements across the specified aperture.

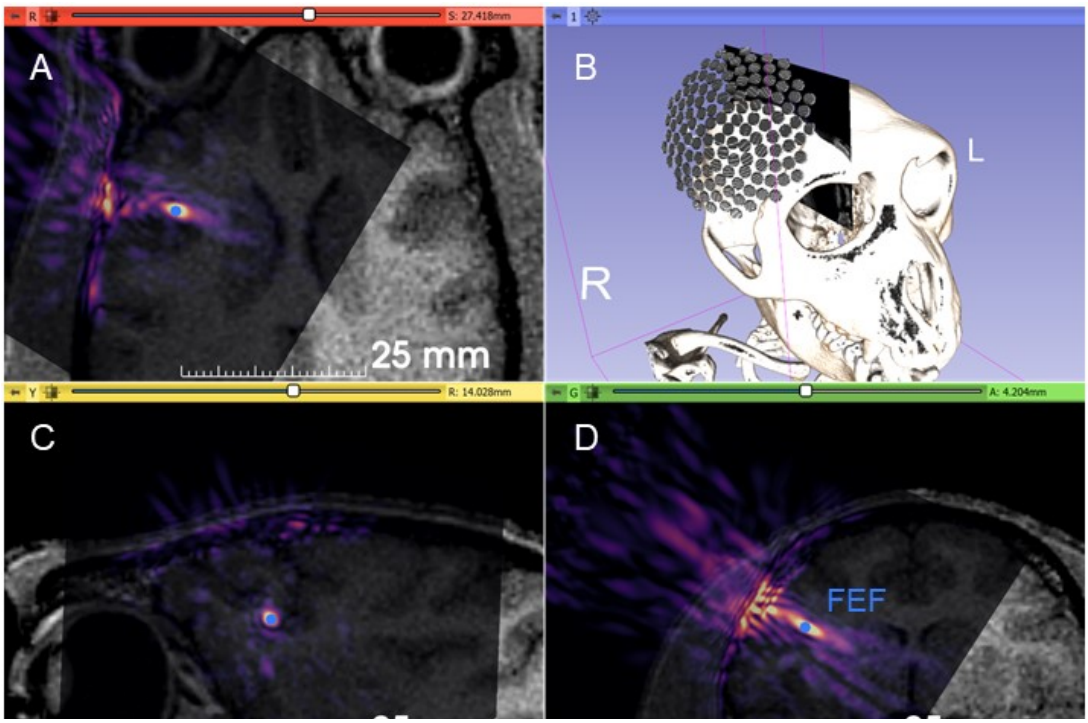

Figure 4.2. Screenshot of 3D-Slicer used to setup k-Wave simulations and visualize results. **(A, C, D)** Root mean square pressure results from simulations overlaid on t1-weighted magnetic resonance images in the transverse, sagittal, and coronal planes, respectively. **B)** 3D models of the macaque skull and transducer model used to generate the k-Wave simulation input fields.

Generating simulation grids

The distributions produced by these scripts were converted into 3D models using k-Wave's makeMultiBowl function which outputs a binary mask of elements matching a specified diameter and facing a focal point which sets the radius of curvature. We then added a marker to this model at the geometric focus to aid visualization. We output the model from MATLAB as a NIfTI file with 0.2 mm isotropic voxels which was read into Slicer. This corresponds to 7.5 points per wave in water at 1 MHz which has been shown to be sufficient sampling in a transcranial simulation convergence test (Robertson et al. 2017). In water-only simulations, we used 0.25 mm isotropic voxels. By representing the transducer model as a NIfTI which includes metadata for size and position, the orientation of the transducer can be manipulated and saved by Slicer's tools for transformation (figure 4.2B). This enabled us to visually place the transducer models at targets guided by CT and MRI images and align orientations to reduce angle-based reflections at the skull.

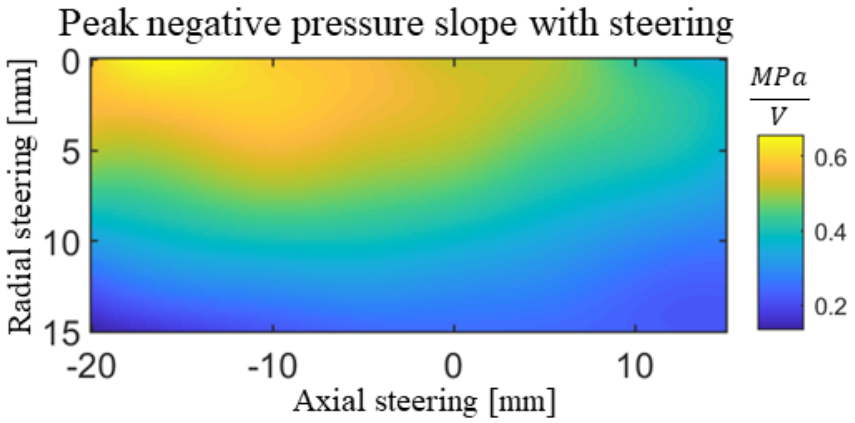

Figure 4.3. Peak negative pressure slopes extracted from a linear fit of pressure to generator output for all steering points collected (interpolated to 0.1 mm step sizes). Because the array steering is radially symmetric, steering points along multiple lateral dimensions can be mapped to this plane by converting to radial distance. Slope has units of MPa/V.

We placed a model of the transducer such that the geometric focus was at or 10 mm beneath the frontal eye

field depending on the simulation and that the angle of the transducer axis was approximately normal to the skull surface. The FEF is irregularly shaped and cannot be spanned by a single acoustic focus. We used the portion of the FEF which has the longest vertical extent as our target because this portion of the FEF most matches an acoustic focus (ellipsoid). We manually registered the four NHP skulls to each other using 3D-Slicer's transform module and emphasized that the portions of the skull nearest to FEF were closely aligned. This was important because the four skulls have different sizes and shapes and so rigid registration of the entire skull results in areas with large differences. With the skulls co-registered, the same transducer orientation could be simulated across all skulls. Furthermore, different transducer geometries could be placed at the same orientation to ensure that the comparison in performance was not affected by differences in the angle or location of the transducer relative to the skulls. Generation of the simulation grid is achieved by using Slicer's resampleImage module. By resampling the CT data with the transducer model, a CT image is created in the simulation space which is sampled identically with the transducer model and serves as the simulation grid. For inward steering simulations, the transducer model is translated 1 cm along its z axis prior to generating the simulation grid. The Slicer and k-Wave workflow also works in reverse, enabling the visualization of pressure fields output by k-Wave within Slicer overlaid on CT and MRI as in figure 4.2. Focal volumes are computed as the volume of an ellipsoid with axis lengths equal to the axial and lateral FWHM of the pressure field (root mean square pressure).

Hydrophone measurements

Beam maps of the acoustic field were collected as a raster scan using a 3-axis motor stage (Image Guided Therapy- Pessac, France) at 0.2 mm lateral and 0.5 mm axial steps. Degassed water tank beam maps were performed using a ceramic needle hydrophone (HNC 0400, Onda Corp., Sunnyvale CA). The hydrophone signals were read by a digital oscilloscope (Picoscope, Allied Electronics, Midrand, South Africa). An optical hydrophone (136–10 T and 132–03, Precision Acoustics Ltd., Dorchester, Dorset, UK) was used for high pressure measurements to avoid damage to the ceramic hydrophone.

For transcranial beam maps, a macaque skull cap which included the region of skull over the FEF was degassed in water for 20 hours at -95 kPa using a vacuum chamber (Abbess Instruments, Holliston, MA, USA) and then placed in a tank of degassed water for measurements. The skull was oriented such that the steered acoustic focus was roughly at the FEF, except 5 mm deeper to prevent hydrophone damage from contact with the skull. Phases for aberration correction were computed by sequentially driving individual transducer elements at maximum power with 40 us pulses while recording the pressure at the target using a ceramic needle hydrophone. For each element, 15 acquisitions were acquired, and the arrival time relative to time zero (trigger) was averaged across runs. Relative arrival times were converted to phase which were used to offset waveforms in the phase-correction measurements.

Pressure calibration for steered sonications

We calibrated the pressure output of the transducer as a function of steering when powered by a 10 watt per channel 128 channel generator (Image Guided Therapy- Pessac, France). An optical hydrophone (136–10 T and 132–03, Precision Acoustics Ltd., Dorchester, Dorset, UK) was used for pressure measurements. The hydrophone was mounted to a 3-axis stage. Measurements were made sampling a 2-D plane at 5 mm increments for points ranging from -20 to +15 mm axially and 0 to 15 mm laterally. At each point, we implemented a power ramp using 75 us pulses starting from the lowest generator output until a mechanical index of 4 was reached at the hydrophone. We then extracted the peak negative pressure (PNP) from each sample. Next, we performed a linear fit between the generator output value and the PNP for each steering coordinate (figure 4.3). This provided a calibration between generator output and PNP as a function of radial steering and axial steering. Because electronic steering of the array is radially symmetric, steering along multiple lateral dimensions can be mapped to this plane by converting the lateral values to a radial quantity. We up sampled the plane with B-spline interpolation to have 0.1 mm step sizes. This plane was used as a look-up table in a script with desired pressure and steering coordinate as inputs and generator

value as output. At the geometric focus, the transducer produces 0.52 MPa peak negative pressure (PNP) per volt (peak positive voltage). Our generator outputs a maximum peak positive voltage of 33 V.

4.4 Results

Inward steering reduces focal volume

Inward electronic steering reduced the focal volume of a transducer model in all transcranial simulations targeting frontal eye field (FEF) when compared with placing the geometric focus at the FEF (figure 4.4). With the geometric focus placed at the FEF, the focal volume was 51.4 ± 19.1 mm^3, and the spot size was 2.8 ± 0.4 mm lateral and 12.9 ± 1.1 mm axial full width at half-maximum (FWHM). With the geometric focus placed 10 mm past the FEF and the focus steered inward 10 mm, the focal volume reduced to 29.7 ±8.1 mm^3 (2.5 ± 0.3 mm lateral and 9.5 ± 1.0 mm axial FWHM). Both the reduction in axial spot size (p=.0076) and focal volume (p=.0435) were statistically significant (single tail student's t-test). With phase correction added to the inward steering condition, the focal volume further reduced to 14.4 ± 2.9 mm^3 (1.9 ± 0.1 mm lateral and 8.0 ± 1.1 mm axial FWHM). Lateral spot sizes reported are the average of two orthogonal measurements. Comparable focal transmission was observed between the geometric focus case, 29 ± 9%, and the inward steered case, 27 ± 6% (p=.1136). Phase correction increased transmission to 34 ± 8%. Focal offset from the selected target was 0.8 ± 0.2 mm and 0.7 ± 0.1 mm for inward steering and geometric groups, respectively (p=0.26, single tail student's t-test). With phase correction applied, focal offset was 0.3 ± 0.3 mm which is less than both the inward steering (p=0.01) and the geometric groups

(p=0.04).

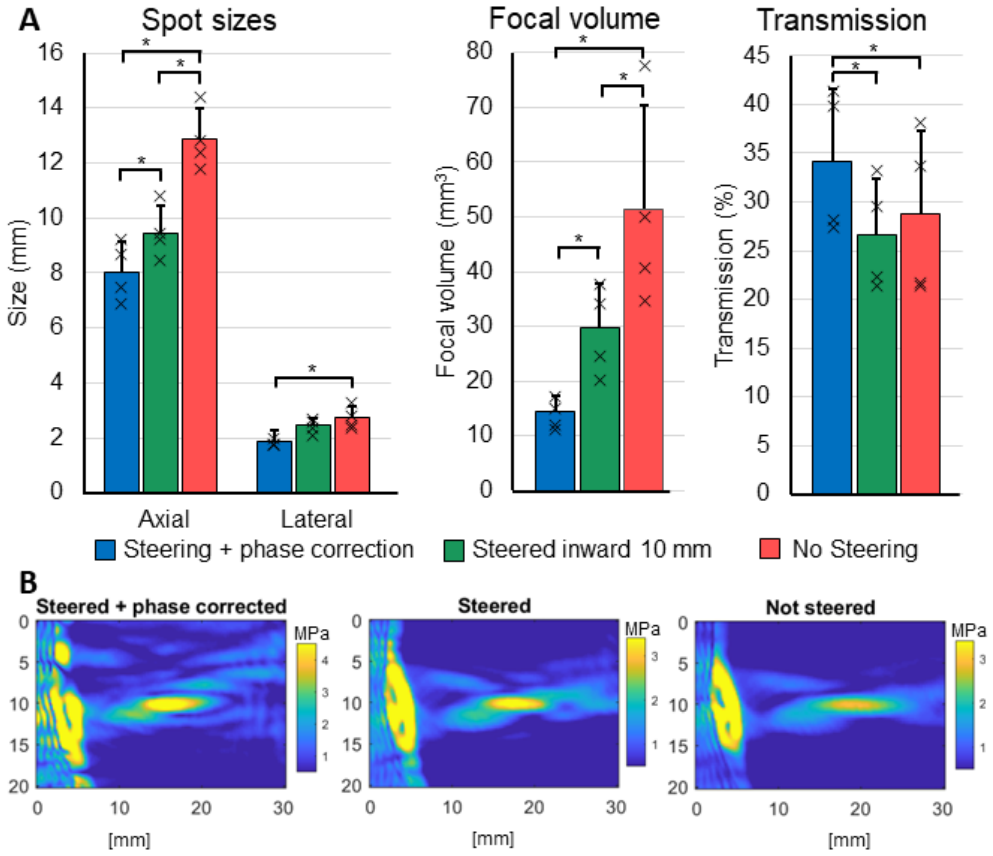

Figure 4.4. Transcranial simulation results in four macaques comparing no steering, steering inward 10 mm, and steering inward + phase correction. **A)** Axial and lateral spot sizes, focal volume, and transmission for the three conditions. **B)** Cropped pressure maps from simulations for the three conditions. * p<.05 (paired, single-tailed student's t-test).

Frequency simulations

To investigate transmit frequency, we first set the radius of curvature (ROC) at 50 mm which worked well with our target depth, inward steering plan, and coupling space requirements set by the presence of muscle outside the skull (FEF is 4-10mm beyond the skull). We simulated transducer frequencies varying from 0.25 to 1.5 MHz (figure 4.5A) using CTs from 4 NHPs with a transducer of geometric f-number equal to 0.9. As expected, transmission, focal volume, and axial spot size reduced with increased frequency.

Aberration correction was required to maintain good transmission at frequencies higher than 1 MHz, and spot size improvements beyond 1 MHz were marginal. 1 MHz achieved our axial spot size goal (< 10 mm). The gains of aberration correction can be difficult to actualize in all experimental scenarios, so our optimization is guided by simulation without aberration correction, and we report the volumes of aberration corrected foci to provide information on theoretical performance. The simulated transmission at 1 MHz was 27 ± 6 % with steering only and 34 ± 7% when aberration correction was applied.

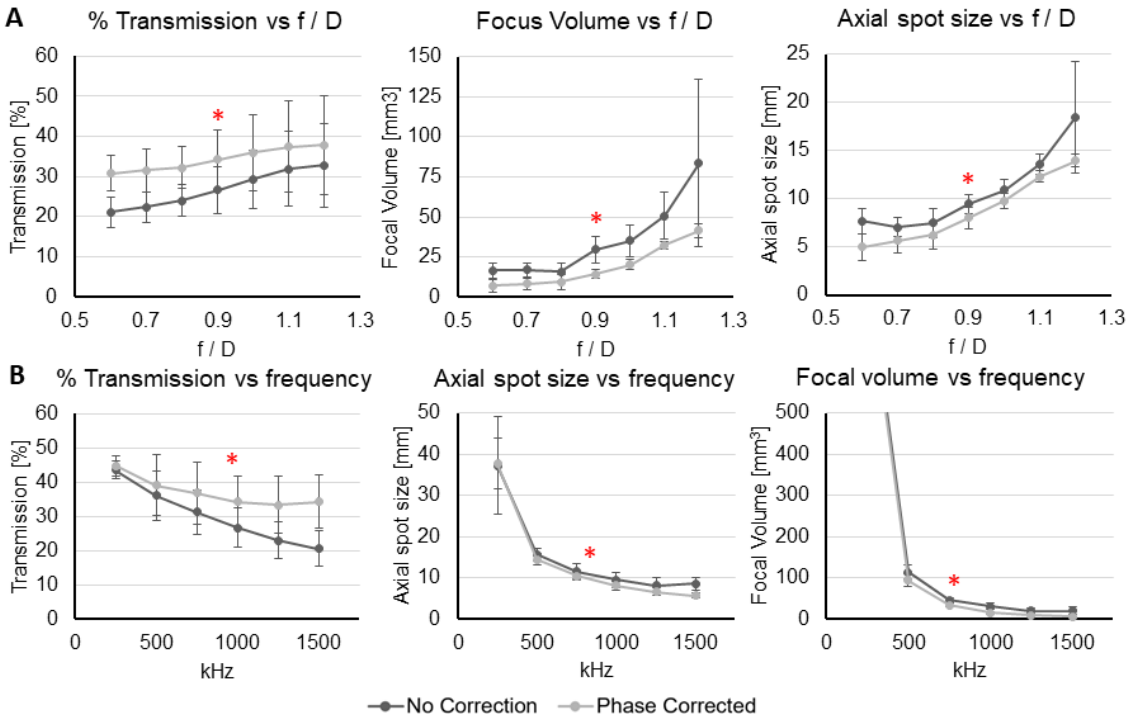

Figure 4.5. Transcranial simulation results in four macaques with the transducer steered inwards 1 cm. **A)** Transmission, focus volume, and axial spot size for f-numbers ranging from 0.6 to 1.2 simulated at 1 MHz. Diameter was varied and focal length was constant (5 cm). **B)** Transmission, axial spot size, and focal volume for frequencies ranging from 0.25 to 1.5 MHz**.** Transmission is percent pressure compared to free field performance. Error bars show standard deviation across macaques (n=4 per datapoint). Light lines show performance using phase-only abberation correction. Dark lines are without aberration correction. * Selected design

F-number simulations

With the center frequency of 1 MHz chosen based on transmission with a single geometry, we then simulated transducers with geometric f-numbers from 0.6 to 1.2 and measured the transmission, focal volume, and axial spot size (figure 4.5B). Higher f-numbers demonstrated better transmission but with larger axial spot sizes and focal volume. The 0.9 f-number model achieved our axial spot size goal (<10 mm). Improvements in axial spot size were marginal at lower f-numbers without aberration correction compared to reduction in transmission so we chose a f-number of 0.9 to compromise between axial spot size and transmission. Furthermore, choosing a lower f-number would increase the area of skull required for sonications and the size of the transducer.

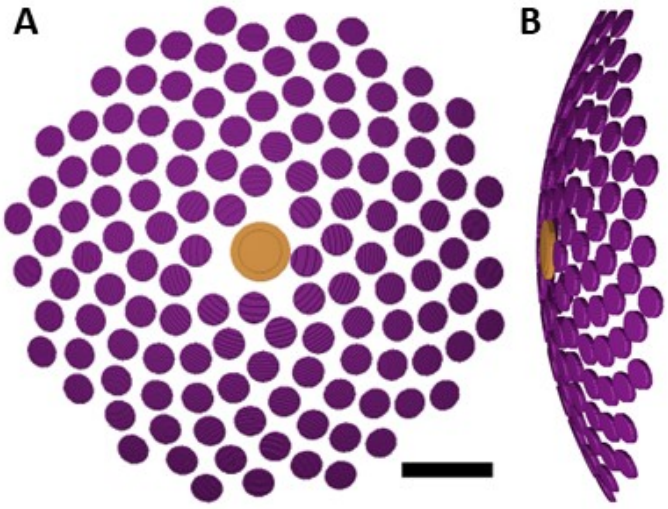

Figure 4.6. Rendering showing element locations and arrangement for final design. There are 128 transmit (purple) and 1 receive element (orange). Scale bar 1 cm. **A)** Top-down view **B)** Side view + 10 degrees of tilt.

Final design

With these simulation results in mind, we generated a final transducer design which allowed space for the passive cavitation element and room around the outer transmit elements for manufacturing. The final design was a 1 MHz transducer with a total diameter of 58 mm, a focal length of 53.2 mm (f-number as 0.92) and 128 transmit elements with 3.5 mm diameters distributed along a Fermat spiral (figure 4.6). The minimum distance between any two elements was 0.2 mm. The true active aperture of the transducer (maximum distance between outer element edges) was 54.1 mm. The coverage of the transducer is 50.1% computed as the percentage surface area of the transmit elements divided by the surface area of a spherical cap with aperture diameter 54.1 mm and radius 53.2 mm. The central passive cavitation detection (PCD) element has an active diameter of 3.5 mm and required a total diameter of 7.5 mm for manufacturing. Its receive sensitivity is centered on the second harmonic (2 MHz). The PCD will be used for cavitation monitoring. Simulations predicted the transducer would achieve a transcranial focal volume of 30 ± 8 mm^3, transmission of 27 ± 6 %, axial spot size of 9.5 ± 1.0 mm, and lateral spot size of 2.5 ± 0.3 mm with 10 mm inward steering without aberration correction. With aberration correction and inward steering, simulations predict

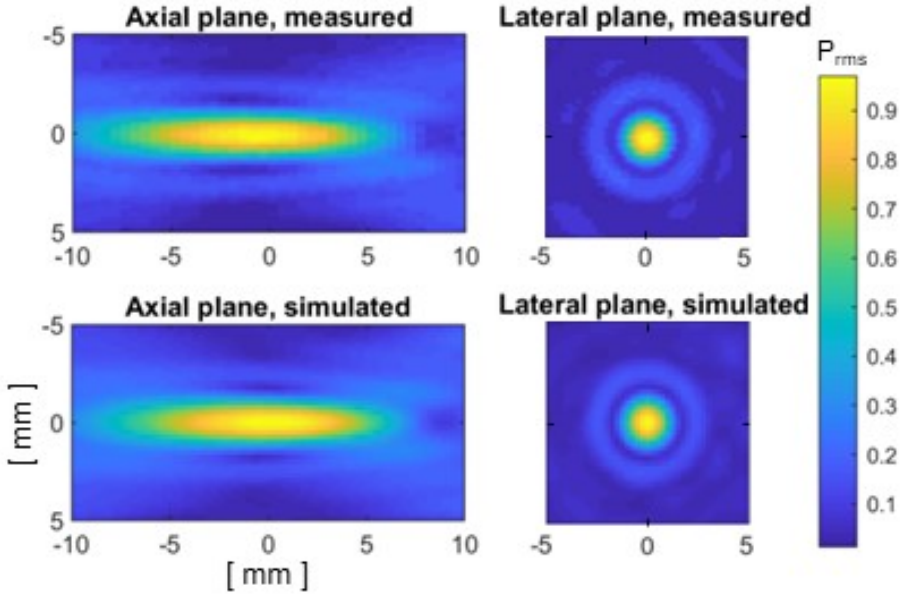

Figure 4.7. Comparing simulated focus with measured focus. **Top row)** measured focus. **Bottom row)** simulated focus. Color bar: P_{rms} (normalized).

a transcranial focal volume of 14.4 ± 2.9 mm^3, transmission of 34 ± 7%, axial spot size of 8.0 ± 1.0 mm, and lateral spot size of 1.9 ± 0.1 mm. These values are within our design goal of 3.0 x 10.0 mm derived from the dimensions of macaque FEF. The transducer was fabricated by Imasonic (Besancon, France) to our specifications.

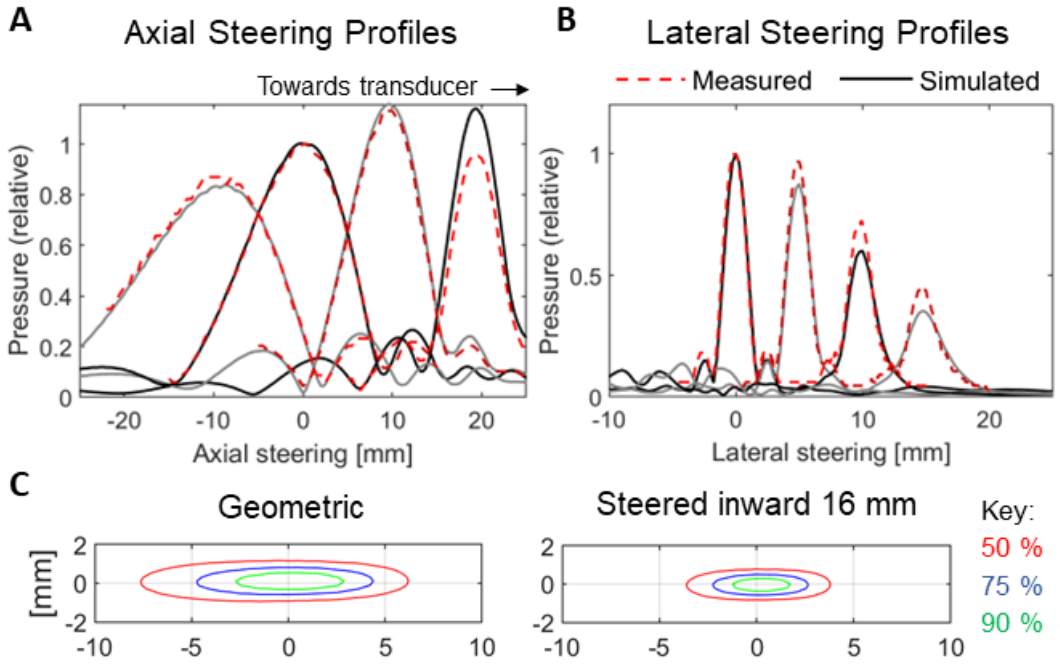

Figure 4.8. Measured and simulated electronic steering performance of the array **A)** Simulation and hydrophone axial line plots through focus steered -1 to 2 cm axially at 10 mm increments (maximum pressure) **B)** Simulation and hydrophone lateral line plots through focus steered laterally at 5 mm increments (maximum pressure) **C)** Measured focus pressure contours for the geometric focus (left) compared to the steered inward focus (right) (p_{rms}). Contours are at 50%, 75%, and 90% the focus maximum.

Beam maps with free field steering

We measured and compared the performance of the transducer in water to our simulations. The measured spot size at the geometric focus was 2.2 x 2.0 x 13.5 mm which was similar to the simulated spot size (2.3 x 2.3 x 13.3 mm) (figure 4.7). We collected axial steering and lateral steering beam maps at steering increments of 10 mm (axial) and 5 mm (lateral) (figure 4.8). The transducer is capable of steering laterally

± 13 mm, axially outward 35 mm and inward 26 mm with <50% pressure reduction. The measured steering shows the same trends in spot size and pressure with steering but with some magnitude difference. We compared the steering performance of the transducer with simulations and confirm that the spot size reduced with inward steering. With inward steering 16.0 mm, the measured spot size reduces to 1.6 x 1.6 x 7.5 mm (figure 4.8C).

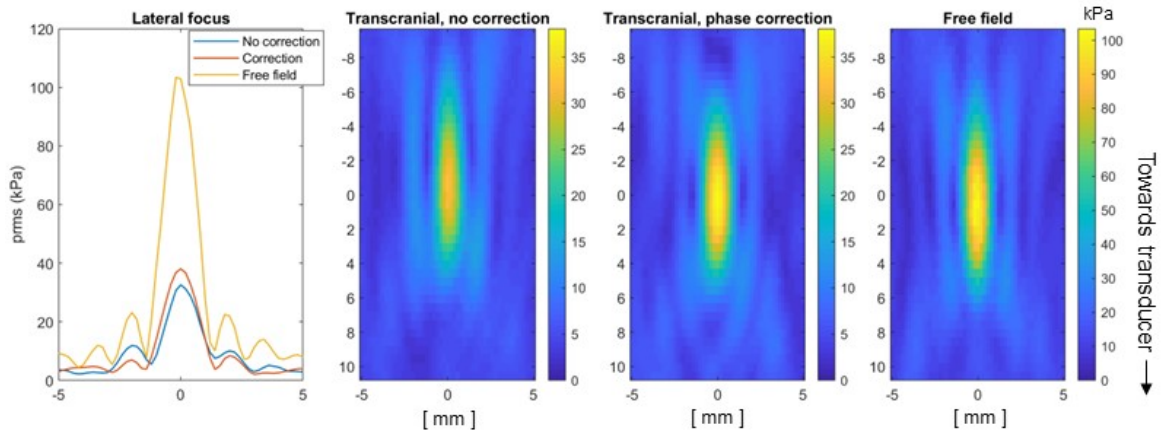

Figure 4.9. Measured beam maps for free field focus, transcranial focus, and transcranial focus with aberration correction. Measurements performed through ex-vivo macaque skull fragment. Color bars show prms in kPa. The skull surface is at 13 mm in the beam map coordinates.

Transcranial evaluation

To evaluate the performance of the transducer through macaque skull, we performed beam maps behind a macaque skull cap with 0.2 mm lateral samples and 0.5 mm axial samples using a ceramic hydrophone. We compared pressure fields for three cases: i) no skull, steered inward ii) with skull steered inward iii) with skull phase corrected at inward steered target. Beam maps in figure 4.9 show the results. The spot size in the free field with 10.0 mm inward steering is 1.6 mm by 9.5 mm. The transcranial spot size without phase correction was 1.6 mm by 10.5 mm with a transmission of 32 %. The aberration corrected spot size was 1.8 mm by 9.5 mm with a transmission of 37 %. The presence of the skull shifted the maximum of the focus away from the transducer compared to the free field focus by 1.0 mm. Phase correction returned the maximum of the focus to the same location as free field.

4.5 Discussion

In many transcranial FUS applications such as BBBO or neuromodulation, control of the spatial extent of the ultrasound focus is desirable to avoid therapeutic effects at off target sites. Small cortical brain regions near the skull are especially challenging to sonicate with high precision and require small focusing transducers able to focus just beneath the skull and with sufficient steering to facilitate neuronavigation. To address these challenges, we designed and tested a transducer in the Macaque which can achieve target specificity in BBBO procedures at the frontal eye field.

We applied transcranial simulations in four macaques across 6 frequencies and 7 transducer f-numbers with and without aberration correction to identify a design which met our criterion of localizing the focus to the frontal eye field. We found that to achieve small focal volume, higher transmit frequencies were required than the typical range used in transcranial procedures for humans and large animals, leading us to choose 1 MHz. This design choice comes at the costs of decreased transmission (26.6 ± 5.7 % predicted by simulations), higher pressure required for BBBO (Nathan McDannold, Vykhodtseva, and Hynynen 2008a), and may reduce SNR in cavitation monitoring scenarios due to frequency dependent attenuation of harmonic signals. However, adequate transcranial focusing with 1 MHz therapeutic array has been demonstrated in human cadavers (Marsac et al. 2012).

Our simulations show that lower f-numbers have smaller transcranial spot sizes but at the cost of increasing aperture size and lower transmission. For the FEF, reduced f-number designs required larger apertures to provide space for coupling due to muscle outside the skull in macaques. We sought to find a small transducer design to lower manufacturing cost and complexity, reduce MRI artifacts, and reduce the skull area required for therapies. For this reason, we gravitated towards f-number above 0.6. For reference, when

targeting the FEF with our f-number 0.9 design, the acoustic path intersects a portion of skull roughly equal to a disc with a 12-mm diameter which is sufficiently small to integrate into typical macaque procedures.

We found that inward electronic steering reduced focal volume without requiring a larger aperture or reducing transmission. Inward steering 10 mm decreased the simulated axial spot size from 12.8 mm to 9.5 mm and steering 16 mm reduced it further to 7.5 mm bringing the focus size within the range of many macaque cortical targets including FEF, our target of interest. Although inward steering of phased arrays can increase near-field pressure in some scenarios (Payne et al. 2011), we did not observe large pressure increases outside the skull in our studies. With inward steering, the pressure in an 8-mm cube above the skull was 27 ± 5% the pressure at the transcranial focus (n=4). Without inwards steering, the pressure above the skull was 27 ± 8% the pressure at the transcranial focus (n=4). Macaques have muscle above the skull and pose risks of bubble-induced bioeffects in muscle tissue at mechanical indexes above 0.4 in the presence of contrast agents (ter Haar 2009). Limiting the pressure above the skull to much less than the focal pressure is important to prevent vascular damage during BBBO therapies.

Simulations helped identify complex acoustic interactions at the skull that highlight important factors to consider when targeting small brain regions. Simulations predicted a shift in the focus away from the transducer in transcranial settings with pre-focal steering, which was corroborated by our *ex-vivo* skull cap beam maps. We have measured in prior works that the focus shifts towards the skull when no electronic steering is applied (Vandiver Chaplin, Phipps, and Caskey 2018; Kusunose et al. 2021). Simulations also predicted aberration correction *in vivo* can reduce the focal volume for the selected transducer from 57 ± 35 mm^3 to 15 ± 6 mm^3. In practice aberration correction is difficult to implement into FUS procedures using optical tracking in macaques. Computing effective phases and amplitudes for correction requires accurate estimation of the transducer's location relative to the skull as well as accurate modeling of the skull, muscle, skin and brain between the transducer and target. Measuring the *in vivo* improvements from aberration correction to develop and validate the correction pipeline is also difficult given that the spatial resolution

of our MR-ARFI sequence (2x2x4 mm) is close to the spot size of the transducer and that the sequence's noise levels are close to the amount of displacement increase expected with perfect aberration correction.

Our hydrophone-based aberration correction is implemented differently than in our simulations for practical reasons. In simulation we place a 1 voxel point source at the target of interest and propagate it out to all elements at once to capture the phase of arriving sound at each element. This allows the information needed to be attained in a single simulation and is possible because the transducer elements can be modeled as sensors. In the physical experiment, we placed a hydrophone at the target and received signal from each element transmitted in isolation. This allows us to attain similar element-wise phase information while using our array and generator in transmit mode as they were designed to be used. Unlike in simulations where simulating 128 transmit channels in separate simulations would be computationally expensive, capturing 128 physical transmit events at a hydrophone takes little time. It is known that cross talk between elements may alter the true phase of signals emitted from elements driven concurrently with nearby elements of different phase (Martin, Roberts, and Treeby 2021). This may reduce the performance of this hydrophone based abberation correction technique as well as electronic steering.

The transducer in this work was optimized for small volume opening in macaques and is likely not well suited for humans due to skull differences and target depths. However, this design approach based on transcranial simulations in multiple subjects varying transducer geometry and frequency at a specific target could be applied across species and targets to evaluate transducer options for other cases. There have been transducers designed for BBBO in humans which relied on building multiple versions (Liu et al. 2008) and testing at a range of frequencies (Liu et al. 2014) to evaluate design options. Undertakings such as these could benefit from incorporating transcranial simulations as done in this work and others (Adams et al. 2021; Ryan M Jones, O'Reilly, and Hynynen 2013; Rebecca M. Jones et al. 2022).

Further work is needed to evaluate the effectiveness of the design choices made for the central receive element (2 MHz peak sensitivity). Both the lower subharmonic (O'Reilly and Hynynen 2012) and higher harmonics and ultra-harmonics (H. Chen and Konofagou 2014; N. McDannold et al. 2012) are useful for cavitation monitoring. The ideal sensor would have high sensitivity at both the half harmonic and higher harmonics while also having low sensitivity at the transmit frequency to improve sampling resolution for cavitation signals which are lower in amplitude than reflections of the transmitted sound. In practice, this is unachievable for single piezoelectric sensors and is part of the motivation behind a multi-frequency array for BBBO which used elements centered at three separate frequencies (Deng et al. 2016). We chose to center our receive element on 2 MHz operating on the assumptions that i) its bandwidth would sufficiently capture 0.5 MHz as well as harmonics up to 3 MHz ii) pre-bubble baseline subtraction would be sufficient for isolation of cavitation signals of interest. Apart from reflection of 1 MHz sound, there is also concern of direct coupling across the face of the transducer from transmit elements into the receive element which adds to the 1 MHz signal for receive events concurrent with transmission events. Other groups have adopted separate receive transducers for passive cavitation detection which avoid direct coupling and allow for orthogonal skull placement (often at the temporal bone window) to improve cavitation signal sensitivity which is omnidirectional (N. McDannold et al. 2012). Dedicating a high number of receive elements across the aperture is another approach which has the added benefit of enabling passive acoustic mapping which provides spatial and temporal cavitation feedback (Ryan M. Jones et al. 2018; Deng et al. 2016). Nevertheless, embedding a central receive element is a common and proven approach (H. Chen and Konofagou 2014; Pouliopoulos et al. 2021; O'Reilly and Hynynen 2012; Pascal et al. 2020; H. A. Kamimura et al. 2019).

The transducer developed here is ideal for BBBO applications and specifically will be used in for local gene-therapy at the frontal eye field in macaques for acoustically targeted chemogenetics (H. Li et al. 2021; Szablowski et al. 2018). Simulations and measurements suggest the transducer will have sufficiently small focal volume to largely limit BBBO to the frontal-eye field. BBB opening volume is dictated by additional

factors beyond focal volume including the acoustic pressure and vascular properties of the targeted tissue. Precise targeting and pressure control will be required to limit opening to the FEF. Given that the skull over the FEF is thicker than most other skull areas (Fig. 1), it is likely that the transducer will perform similarly or better at other cortical targets. However, at targets too deep to be reached while steering inward, simulations suggest the spot size may be larger. Upon validating our targeting approach, cavitation monitoring software, and ability to safely open the BBB, we will deploy the system for transcranial gene therapy.

4.6 Conclusion

Small volume blood brain barrier opening is critical for study designs requiring target specificity such as gene therapy in the frontal eye field. In this work, we designed a small aperture phased array optimized for BBBO localized at the frontal eye field in macaques. The optimal design was fabricated, evaluated in a water tank, and shown to focus sufficiently well through a macaque skull cap. The transducer produced by this work will facilitate localized transcranial gene-therapy at the frontal eye field.

4.7 Supplementary materials

Integrating into optical tracking for image-guided FUS therapy

We 3D printed (Stratasys, Rehovot, Israel) a transducer case to facilitate coupling for transcranial procedures (figure 4.S1). The case has an outer diameter of 102 mm. Two outer grooves made for 4 mm n-buna O-rings seal a latex membrane which serves as a water bag for coupling. Two inner grooves made for .103” n-buna O-rings provide a seal at the outer housing of the transducer. The transducer slides into the

case to form a seal. The water bag is serviced by inflow and outflow tubes which attach to printed ports (3.3 mm ID, 5.1 mm OD) and provide flow between the inner and outer seal points. Figure 4.S1B shows the transducer with the case on and filled with water.

We fabricated a backplate which mounts to a stereotactic frame via a 12.7 mm inner diameter hole (figure 4.S1A). The backplate also adapts to a passive tracking tool compatible with an NDI Polaris Vicra tracking system (Northern Digital Inc, Waterloo, Canada). The backplate was fabricated with a combination of 3D printing, laser cutting, and machining. The optical tracking piece is 3D printed with male Lego ports. We use Lego ports because axle Lego pieces snap into tracking spheres provided by NDI. Our optical tracking methods were described in detail previously (V. Chaplin et al. 2019).

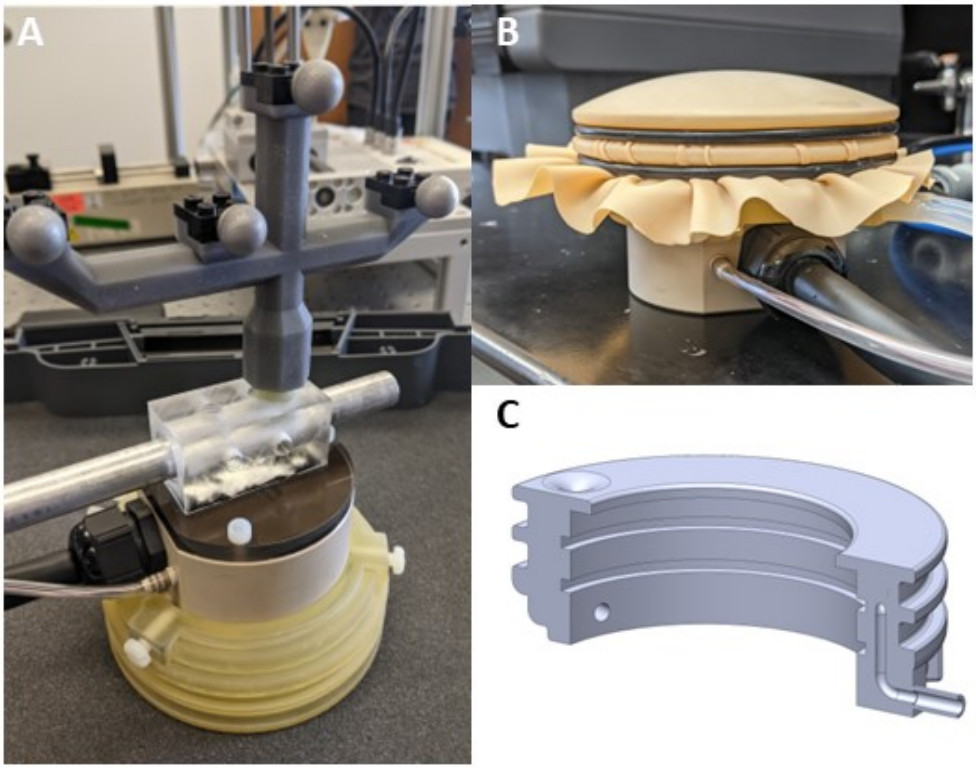

Figure 4.S1. Transducer case and tracker fabrication. A) Assembled case, transducer, backplate, and optical tracking tool. B) Transducer case and transducer with filled water coupling bag and O-rings. C) Solidworks drawing of transducer case with sliced view to reveal inner O-rings and interior tubes for water flow.

Optical tracking calibration

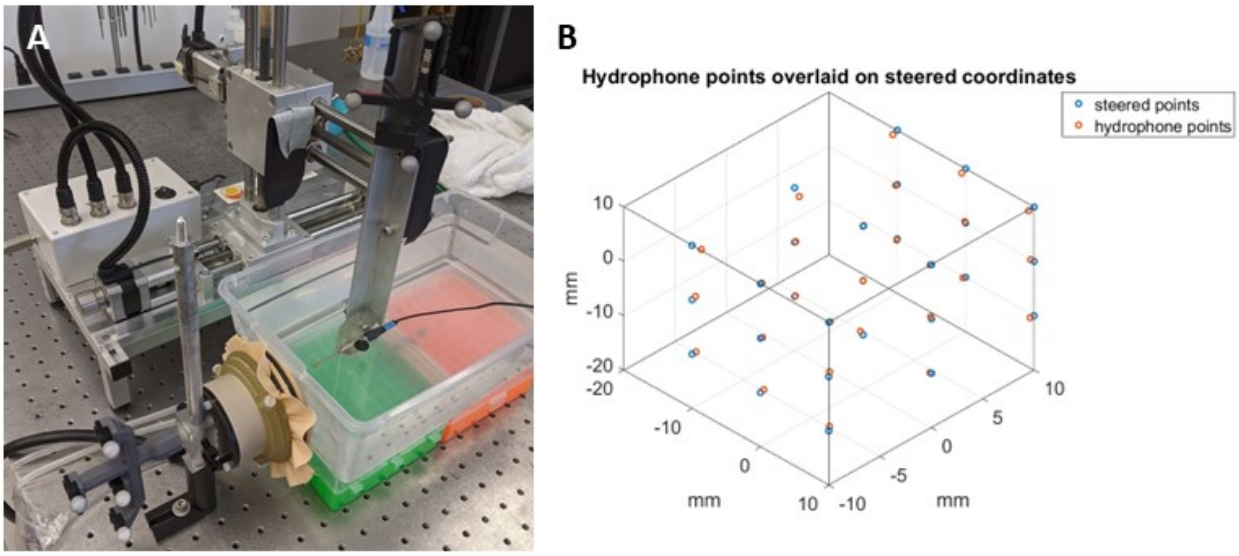

Figure 4.S2. Finding the transformation between the transducer tracker and transducer steering coordinates. A) experimental setup. The transducer is coupled to a water tank while being optically tracked. The hydrophone is also optically tracked. B) Measured hydrophone locations while steering the focus compared to known steering coordinates. Registration of these sets calculates the desired transformation.

A transducer tracker file was generated using NDI's NDI 6D Architect program. In addition to tracking the tool itself, we needed to track the location of the acoustic focus relative to the tool. To measure the transform between the tracker orientation and acoustic focus orientation, we performed a water tank experiment while using optical tracking to track the transducer tracker and a hydrophone (figure 4.S2). The hydrophone was tracked by fixing a tracker tool to an arm holding the hydrophone. The tip of the hydrophone can be tracked by performing a pivot test about the tip of the hydrophone while recording tracking data with NDI Track software. To avoid damaging the hydrophone, we replaced it with a brass replica during the pivot test. Although placing the tracked hydrophone tip at the acoustic focus allows us to directly compute the vector between the transducer tracker to the focus, it is desirable to also solve for the rotation angles of the tracker relative to the transducer so the transducer's electronic steering coordinates can be addressed based on the optical tracker location. To acquire data required to solve for the translation and rotation, we steered the focus to a grid of points spanning ± 1 cm in all dimensions at 1 cm increments. At each point, we moved

the tracked hydrophone tip to the focus in the water bath and collected a tracking point. This provides a grid of points at the focus with tracking coordinates relative to the transducer tracker and a grid of corresponding coordinates in transducer steering space. These two sets were registered (Fitzpatrick, West, and Maurer 1998) in MATLAB to output a transform which goes from transducer tracker to ultrasound coordinate space with (0,0,0) at the geometric focus of the transducer.

Chapter 5

Small volume blood-brain barrier opening in macaques with a 1 MHz phased array

5.1 Abstract

Focused ultrasound blood-brain barrier (BBB) opening is a promising tool for targeted delivery of therapeutics into the brain. The volume of opening determines the extent of therapeutic administration and sets a lower bound on the size of targets which can be selectively treated. Here, we tested a custom 1 MHz array transducer optimized for cortical regions in the macaque brain with the goal of achieving small volume openings. We integrated this device into a magnetic resonance guided focused ultrasound system and demonstrated twelve instances of small volume BBB opening with average opening volumes of 59 ±37 mm^3 and 184 ±82 mm^3 in cortical and subcortical targets respectively. We developed real-time cavitation monitoring using a passive cavitation detector embedded in the array and characterized its performance on a bench-top flow phantom mimicking transcranial BBB opening procedures. We collected cavitation monitoring during *in-vivo* procedures and compared cavitation metrics against opening volumes and safety outcomes measured with FLAIR and susceptibility weighted imaging. Our findings show BBB opening at smaller volumes than previously reported in macaques and characterize the safe pressure range for 1 MHz BBB opening. This system enables BBB opening for drug delivery and gene therapy to be limited to more specific brain regions.

5.2 Introduction

A physiological barrier exists between the parenchyma and vasculature of the brain, blocking the transport of pathogens, neurotoxic plasma components, and blood cells (Sweeney et al. 2019). Vessels in the brain develop a continuous endothelial cell membrane sealed by tight junction structures and highly selective transport systems which account for this blood-brain barrier (BBB) (Armulik et al. 2010). While critical for regulating transport between the brain and the broader circulatory system, the BBB creates a major hurdle in the treatment of neurological disorders (Abbott 2005). Any candidate therapeutic agent faces the issue of low transport into the brain unless smaller than 400 Da and forming fewer than 8 hydrogen bonds (Pardridge 2012). These chemical properties exclude most small molecule drugs and all large molecule drugs with some exceptions such as receptor-mediated (Lajoie and Shusta 2015) and Trojan horse (Pardridge 2006) vehicles, or vasodilation induced by mannitol infusion (Rapoport 2000). These obstacles remain barriers in the treatment of Alzheimer's disease, Parkinson's disease, glioblastoma, and other neurological disorders.

Focused ultrasound (FUS) in combination with microbubbles can reversibly open the BBB noninvasively in focal brain locations and has been explored for many applications where localized drug delivery is desired. Circulating microbubbles interacting with the acoustic focus temporarily increase the permeability of the BBB through a mechanical interaction (Hynynen et al. 2001). FUS BBB opening is sufficient for transport of 70 kDa molecules (Choi et al. 2010) and magnetic resonance contrast agents of hydrodynamic diameters up to 65 nm (Marty et al. 2012). This opening size extends brain therapeutic options to include viral vectors (C.-Y. Lin et al. 2016)(H. Li et al. 2021), nanoparticles (Ohta et al. 2020), neurotrophic factors (Samiotaki et al. 2015), and antibodies (Kinoshita et al. 2006). Transport of even larger molecules (2,000 kDa) has been achieved but may pose risk of permanent damage (H. Chen and Konofagou 2014). Safety can be improved by monitoring bubble activity during application of therapy (O'Reilly and Hynynen 2012).

Safe FUS BBB opening without edema or hemorrhage has been demonstrated in Macaques (Pouliopoulos et al. 2021) (N. McDannold et al. 2012) and humans (Lipsman et al. 2018) (Carpentier et al. 2016). Edema has been reported at lower pressures than what cause red blood cell extravasation, but typically resolves within one week (Downs, Buch, Sierra, et al. 2015; Downs, Buch, Karakatsani, et al. 2015).

Effective and safe BBB opening requires accurate *in situ* pressure estimation This is challenging in transcranial macaque procedures where pressure delivery varies across targets and skull incidence angle at magnitudes affecting BBB opening outcomes (M. E. M. Karakatsani et al. 2017). Most studies have used cavitation monitoring for *in situ* pressure feedback after it was shown that incorporating harmonic and broadband signatures can reduce the occurrence of hemorrhage and edema in rats (O'Reilly and Hynynen 2012). However, cavitation monitoring is increasingly difficult with increasing skull attenuation, and attenuation is higher at 1 MHz through macaque and human skulls (S.-Y. Wu et al. 2014). Inspired by prior work focused on skull effects, we adopted a cavitation monitoring strategy which captures baseline spectra for all candidate amplitudes prior to therapy (H. A. Kamimura et al. 2019). This provides a mean to adaptively change pressure during therapies based on spectral content while removing the effects of reflected sound with changing transmit amplitude. During all therapies, we plotted stable and inertial cavitation metrics as done in similar systems along with an updating spectrogram and line plot of the latest spectrum (Marquet et al. 2014; Pouliopoulos et al. 2021; Chien et al. 2021; Novell et al. 2020).

In glioblastoma treatment, large opening volumes on the order of 1-2 cm^3 are desirable to match tumor size (Idbaih et al. 2019). However other applications require small opening volumes to match the anatomical target's size. The transducer tested in this work is designed for gene therapy at the frontal-eye field (FEF) and benefits from restricting the gene delivery to the FEF alone. The macaque FEF is approximately 10 mm in depth at its largest cross-section, 3 to 9 mm wide and has a total volume of 211 mm^3 (Jung et al.

2021). Most BBB openings demonstrated in macaques have used single element transducers ranging from 200 to 500 kHz which are well suited for transmission through the skull but have spot sizes much larger than the FEF. The transducer in this study has a higher central frequency of 1 MHz and a spot size of 1.9 x 1.9 x 9.5 mm in free field when steered inward 10 mm making it well suited for this target. We describe the design and characterization of this transducer in a prior publication (T. Manuel, Phipps, and Caskey 2022).

The goal of this work is to investigate the capabilities of a transducer optimized for small volume BBB opening in macaques, including developing cavitation-based feedback to identify the pressure range which opens the BBB without causing edema or hemorrhage. We characterize the performance of a cavitation monitoring system in *in vivo* and benchtop scenarios, and then applied the system to open the macaque BBB and quantify the opening volumes achievable at different cortical and subcortical targets, including the FEF. Our study is the first to characterize ultrasound-based BBB opening with 1 MHz through intact macaque skulls at cortical and subcortical targets, outlining a safe pressure range and highlighting challenges with cavitation monitoring through the skull at high frequencies.

5.3 Methods

Transducer specifications

A custom built 1 MHz array (focal length 53.2 mm, diameter 58 mm) was used for therapies (Imasonic, Besancon, France). . The transducer is a 1 MHz array with a total diameter of 58 mm, a focal length of 53.2 mm (f-number as 0.92), and 128 3.5 mm diameter transmit elements distributed along a Fermat spiral. The transducer features one central receive element for cavitation monitoring with peak sensitivity at 2 MHz and an active diameter of 3.5 mm. The transducer's spot size is 2.2 x 2.0 x 13.5 mm (31 mm^3). The spot size decreases with steering towards the transducer. All cortical targets leverage this to reduce opening

volume, using an inward steering of 10 mm. At 10 mm, the spot size reduces to 1.9 x 1.9 x 9.5 mm (17.95 mm^3) in free field. We expect the focus to broaden due to aberration in *in vivo* procedures. Simulations predict a transcranial spot size of 2.5 ±0.3 mm lateral and 9.5 ±1.0 axial (30 ±8 mm^3) with conditions used during our cortical therapies (10 mm inward steering and no aberration correction). Transcranial transmission to the frontal eye field was 27 ±6% in simulations.

We 3D printed a custom transducer cone (Stratasys, Rehovot, Israel) which paired with a latex membrane bound by rubber o-rings and a degassing circuit to provide coupling to the head during procedures. This setup is described in more detail in the transducer design paper (T. Manuel, Phipps, and Caskey 2022). The transducer was powered by a 10 watt per channel, 128 channel generator (Image Guided Therapy- Pessac, France) which was impedance matched to the transducer via matching network.

Animal protocol

The ultrasound procedures were performed in two adult macaques (one male, one female) with a minimum of two weeks between sessions in the same macaque. 5 scan days with 12 total therapy attempts were performed with no more than 3 therapies in a single day. During procedures animals were initially anesthetized with ketamine hydrochloride (10 mg/kg) and then anesthetized with isoflurane (1.0-1.5%) delivered over medical air. Medical air was used over oxygen delivery because oxygen has been shown to reduce the half-life of circulating microbubbles compared to medical air (Mullin et al. 2011). 2.5% dextrose in saline solution was infused intravenously (3 ml/kg/h) to prevent dehydration. Artificial ventilation was used during the procedure. Animals were placed in a custom stereotaxis frame with ear bars, eye, and mouthpieces to secure the head (Figure 5.1). A circulating water blanket informed by a rectal temperature probe was used to maintain body heat between 37.5°C and 38.5°C. Respiration pattern, heart rate, end-tidal CO^2 (24-32 mmHg; SurgiVet), and peripheral capillary oxygen saturation (SpO^2; Nonin) were monitored and maintained during the procedure. All procedures were conducted in accordance with National Institutes

of Health guidelines and were approved by the Institutional Animal Care and Use Committee of Vanderbilt University. All macaques were imaged using two surface coils placed on opposite sides of the head.

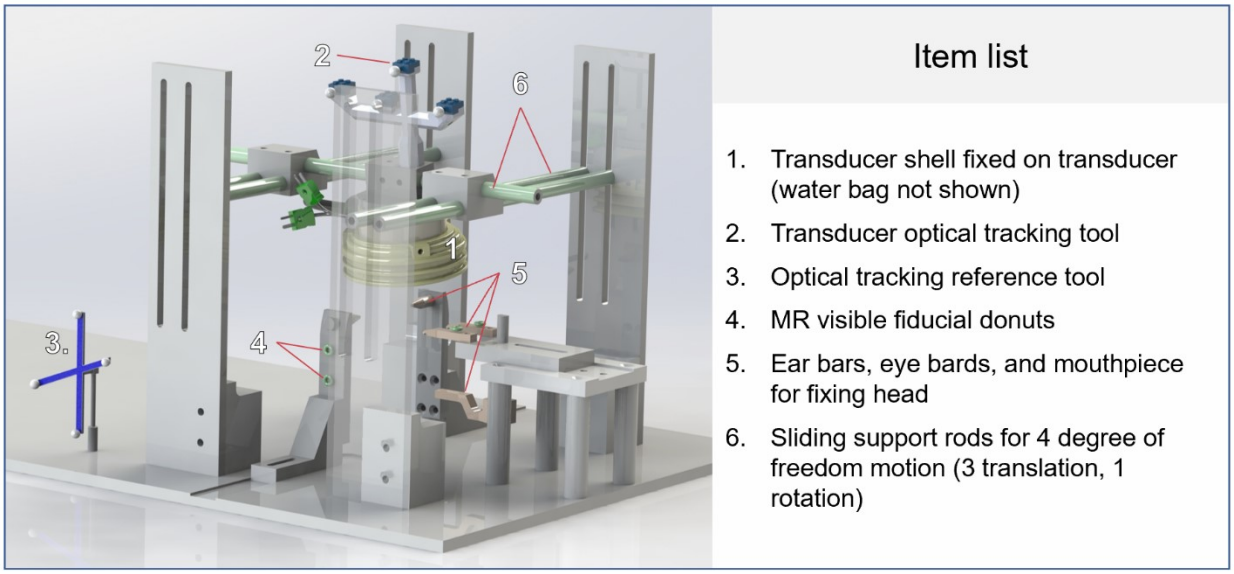

Figure 5.1. Mechanical and optical tracking setup used during in vivo BBB opening procedures (water bag for coupling not shown).

Neuronavigation

The transducer was mechanically moved with the custom stereotactic frame guided by optical tracking as described previously (Phipps et al. 2019; V. Chaplin et al. 2019). A Polaris Vicra optical tracking system (Northern Digital Inc., Ontario, CAN) was used for tracking. A magnetic resonance imaging (MRI) compatible rigid body tracker was fixed to an NHP-table which also held the stereotactic frame. The fixed tracker was used as an optical tracking global reference to track a separate tracker fixed to the transducer and a stylus used to located six multimodality fiducials (IZI Medical Products, Maryland, USA) distributed on the ear bars and eyepieces holding the monkey head. The fiducials were visible on T1-weighted images, allowing registration between MRI image-space and optical tracking space which was done with 3DSlicer's

Image Guided Therapy module (Ungi, Lasso, and Fichtinger 2016). Optical tracking was used for initial guidance of the transducer to the target by projecting a model of the focus onto the MR images. The transform used to orient the focus relative to transducer tracker was created in a water bath experiment by measuring the location of the focus relative to the transducer's rigid body tracker using an optically tracked hydrophone (T. Manuel, Phipps, and Caskey 2022). Tracking was visualized along with MR images in 3DSlicer (http://www.slicer.org/). Magnetic resonance acoustic radiation force imaging (MR-ARFI) was used to confirm the position of the focus relative to brain anatomy prior to each therapy and inform electronic steering of the focus if necessary (Nathan McDannold and Maier 2008). The MR-ARFI pulse has been previously described (Phipps et al. 2019). Therapies were performed in a 3 Tesla MRI scanner (Phillips, Elition X,Amsterdam, Netherlands).

During procedures, we first select a target on a T1-weighted image. Next we orient the transducer such that the optically tracked focus is close to the target of interest. We then move the monkey, frame, and transducer into the MRI bore and collect MR-ARFI to measure the displacement generated by the acoustic focus. If the displacement overlaps with grey matter near our target of interest, we move forward with therapy. If not, we steer the beam electronically while collecting MR-ARFI images until we displacement is measured in grey matter at our target. In several cases, particularly at cortical targets, the displacement images were insufficient for focus identification. In these cases, we acquire an additional MR-ARFI with the beam electronically steered 1 cm away from the skull. In those cases, observing displacement in regions beneath a grey matter zone at our target confirmed our positioning.

Acoustic therapy

All therapies used 10 ms, 1 MHz pulses repeated at 2 Hz for 2 minutes following the arrival of microbubbles. Injections were intentionally slowed to take between 15 and 30s to prevent bubble collapse

while traveling through the syringe needle. To achieve consistent therapy length, we terminated therapies two minutes following the completion of a saline flush designed to clear remaining bubbles from the injection port and catheter line. Therapies were performed at the foot of the MRI bed (~7 feet outside the bore) to minimize the damping effect of a strong magnetic field on bubble oscillations (Yang et al. 2021). We tested pressures spanning 0.4 to 1.4 MPa. Once hemorrhage was detected at 1.4 MPa, no pressures at or above that range were tested again.

Definity microbubbles (Lantheus Medical Imaging, North Billerica, MA, USA) were administered at 20 uL/kg diluted into 3 mL of saline. Following therapy, a T1-weighted image was collected. Gadavist (Leverkusen, North Rhine-Westphalia, Germany) was injected at a dose of 0.1 mL/kg and circulated for 5 min prior to collection of a second T1-weighted image. Susceptibility-weighted images were collected to check for extravasation of red blood cells. FLAIR images were collected to check for edema (Ho, Rojas, and Eisenberg 2012).

In situ pressure for display in figures is estimated as 27% of free field. This value is taken from simulations of this transducer in macaques which predicted a transmission of 27 ±6% through four monkey skulls at the FEF (T. Manuel, Phipps, and Caskey 2022). Also informing the transmission estimate are water tank measurements through an ex-vivo macaque skull which gave transmissions from 15% to 40% depending on skull orientation. Assigning a single transmission value is an oversimplification because transmission changes with each subject, target, and transducer orientation. However, this helps with visualization and interpretation of results. When positioning the transducer, we attempted to minimize the angle between the transducer and the skull to avoid the effects of angle on BBBO outcome (M. E. M. Karakatsani et al. 2017).

MR-Imaging Parameters

T1-weighted: 3D magnetization prepared gradient recalled, TR/TE: 9.9/4.6 ms; flip angle: 8°; in plane resolution: 1 mm^2; slice thickness: 1 mm with 0.5 mm slice overlap reconstructed to 0.5 mm isotropic voxels. Susceptibility-weighted (SWI): 3D spoiled gradient recalled, TR 31 ms; 4 TEs (7.2, 13, 20, 26 ms); flip angle: 17°; in plane resolution: 0.5 mm^2; slice thickness: 1 mm with 0.5 mm slice overlap reconstructed to 0.33 x 0.33 x 0.5 mm. FLAIR: 3D inversion recovery segmented k-space; TR/TE: 4.8/0.34 ms, inversion time: 1.65 ms; flip angle: 90°; in plane resolution: 1 mm^2; slice thickness: 1 mm with 0.5 mm slice overlap reconstructed to 0.5 mm isotropic; 2 averages.

Image processing

All pre and post gadolinium T1-weighted images were processed by FSL's BET tool (S. M. Smith 2002) for brain extraction and then by FSL's FAST segmentation algorithm (Zhang, Brady, and Smith 2001). The FAST algorithm was used for bias field correction and segmentation into tissue types. A rough crop of the head was required prior to BET for successful brain extraction. Five iterations were used for bias field correction (option -n). Following bias field correction several of the images showed histogram differences beyond what would be expected from the presence of gadolinium alone. If unadjusted, the subtraction images generated from the pre and post gadolinium injection t1-weighted images displayed whole brain differences which made quantifying opening difficult. We devised a two-step process to adjust for this. First, we balanced the images by iteratively applying a scalar offset to the post-gadolinium image while minimizing the difference of tissue type thresholds output by the Otsu threshold technique (Otsu, n.d.). Next, we used MATLABs histogram matching algorithm (imhistmatch) to match the histogram of the post gadolinium image to that of the pre gadolinium image.

Percent change images were created using the balanced and histogram matched pre and post gadolinium T1-weighted images. The percentage change images were cropped using a cylinder mask centered on the

acoustic focus of size equal to three times the free-field pressure size (full-width at half maximum) which corresponds to a cylinder height 30, diameter 9 mm, and volume 1908 mm^3. This mask was created using 3D slicer's "create model" module and placed at the location with angled orientation informed by optical tracking and MR-ARFI. Cropping the percent change image reduces off target mislabeling of BBBO at noisy regions and blood vessels in the image far enough away from the focus to rule out as BBBO. For white matter/grey matter quantification, the cropped percent change image was registered to a tissue type atlas for the corresponding therapy. Grey/White/CSF atlases were created from FSL's FAST segmentation algorithm. See figure 5.2 for a visualization of processing steps applied to the percent change image. The caudate and putamen required manual correction in several therapies where subcortical grey matter was

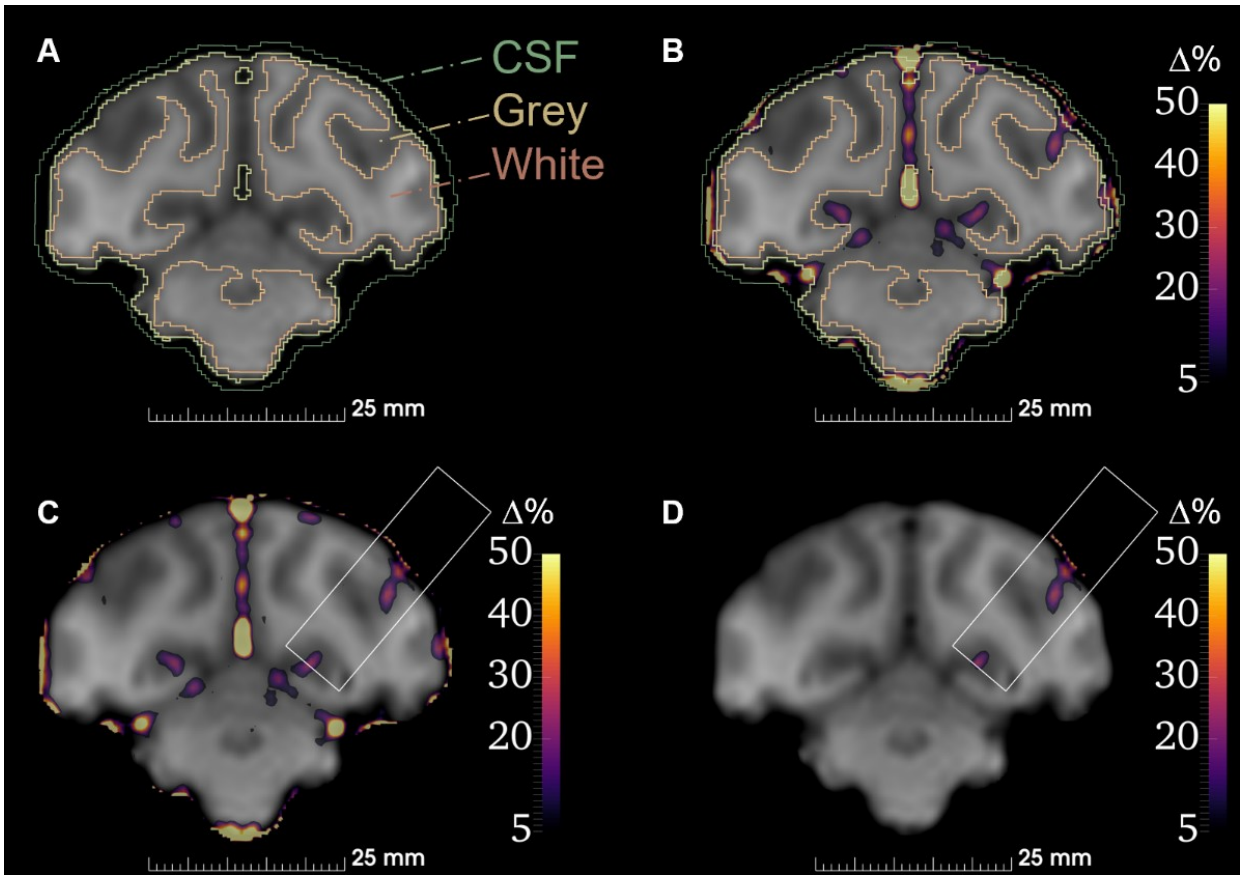

Figure 5.2. The image processing pipeline used to quantify opening volumes. A) segmentation into tissue types; B) overlay of full percentage change image onto segmentation; C) Cylinder mask used to crop around targeted region; D) Final percent change image used to quantify opening.

mislabeled as white matter. Opening volumes are reported using enhancement thresholds of 10%, 20% and 30%.

Cavitation water tank measurements

We built a flow phantom to mimic *in vivo* therapy conditions to enable benchtop testing of the cavitation monitoring system (figure 5.3). The phantom used 4 mm ID soft PVC plastic tubing at the point of the acoustic focus. We used a flow circuit powered by a 12V variable speed pump driven by a variable power supply to circulate the microbubble solution. We tuned the voltage on the power supply to achieve a 1 cm/s flow velocity. Velocity was measured by introducing a visible air bubble into circulation and timing its traversal through a known length of tubing. We matched estimated *in vivo* microbubble concentrations by converting the microbubble dose (20 µl/kg) and the average blood volume in adult macaques (60 ml/kg) which gives a ratio of 20 µl microbubble solution per 60 ml of water to use in the flow phantom (Bender 1955). For water tank measurements we used in-house manufactured microbubbles. Our microbubble fabrication process is described previously (Singh et al. 2022). Stirring was key to keep the bubble solution mixed during experiments and was achieved by placing a reservoir on a magnetic stirrer. The bubble tube was held by a 3D printed y-shaped adapter mounted to a 3-axis stage. The tube was aligned with the acoustic focus while filled with air by maximizing the amplitude of the reflection off the tube recorded at the receive element.

Water tank measurements through skull were achieved using an *ex vivo* monkey skull cap which was degassed for 24 hours at -95 kPa while submerged in a cylindrical vacuum chamber (Abbess Instruments, Holliston, MA, USA). The transmission through this skull fragment was between 15 and 40% depending on skull orientation (measured using a ceramic needle hydrophone). Therefore, to attain an estimate of transmission for the specific orientation during the flow experiment, we captured a 5-cycle pulse-echo off

the flow tube filled with air with and without the skull present by transmitting with the therapy elements and receiving with the PCD. With the skull present, the receive amplitude decreased by 87.5%. The one-way transmission loss was estimated from this two-way measurement as $T_{1way} = \text{sqrt}(T_{2way})$ or $T_{1way} = (1-0.8755)^{0.5} = 0.35$ or 35%.

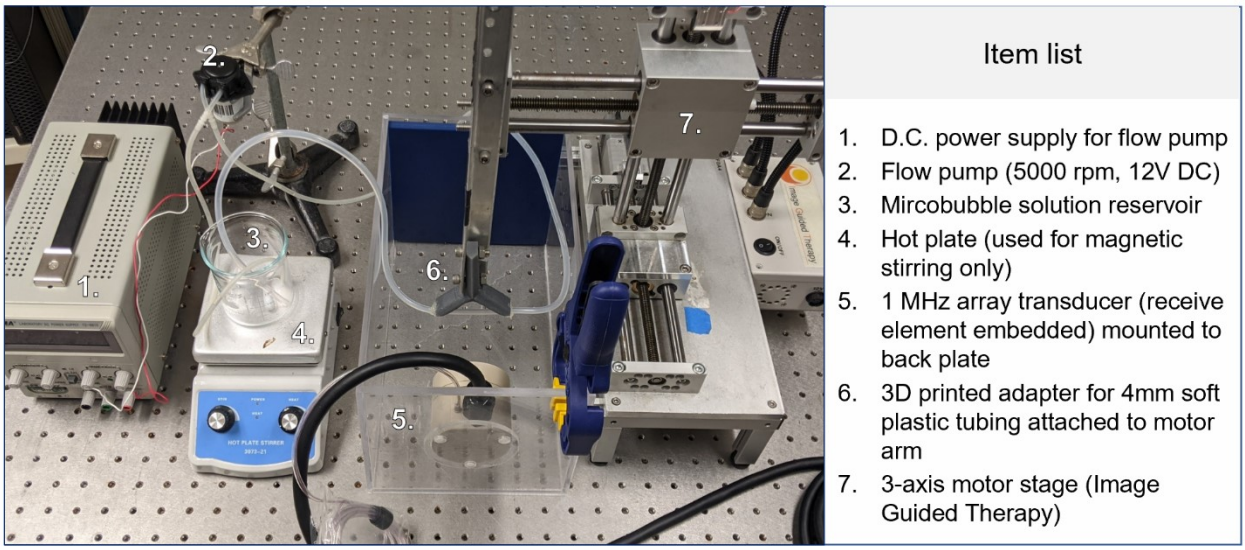

Figure 5.3. The setup used for water tank microbubble flow phantom measurements to develop and validate the cavitation monitoring system.

Cavitation monitoring software

We built a custom python application to monitor cavitation. The design of the monitoring software emphasized the ability to visualize cavitation signals in real time, change therapy amplitudes, and present metrics which inform if *in situ* pressure reaches unsafe levels. This application communicates between a Picoscope ps5000a mounted within our generator cabinet, the SDK provided by Image Guided Therapy for generator control, and user inputs given through a graphical user interface (Tkinter). The sample rate was fixed at 62.5 mega samples per second and 500 µs captures. One capture was acquired after a 50 µs delay following each therapy pulse trigger (2 Hz). Prior to therapy, the software allows the user to define a range

of candidate amplitudes and an electronic steering coordinate. Prior to bubble injection, the software acquires baseline captures for each candidate amplitude. 20 captures per baseline are acquired and averaged in the frequency domain. These baselines enable dynamic baseline subtracting i.e., subtracting the baseline which corresponds to the current therapy amplitude. This aids in decoupling effects from reflection amplitude changes and microbubble emission changes and was first adopted by Kamimura and colleagues (H. A. S. Kamimura et al. 2016).

During therapy the software displays four windows: a spectrogram; a 2D line plot of the latest spectrogram column; plots of stable cavitation and inertial cavitation metrics versus time; and a control panel to start and stop therapy, change amplitude, and save data. For each therapy pulse, a column n in the spectrogram was calculated as:

$$S(f,n) = |FFT\{p_n\,(t)\}| - |FFT\{p_{base}(t)\}| \tag{5.1}$$

where S is the spectrogram with rows in frequency space f and columns n corresponding to the pulse/acquisition number. $p_n(t)$ is the latest acquired pressure-time series and $p_{base}(t)$ is a baseline pressure-time series from a pulse with the same current transmit amplitude. FFT is the discrete fast Fourier transform.

Our PCD has a central frequency of 2 MHz and detects harmonics from 0.5 MHz to 3 MHz in water tank measurements with a flow phantom and no skull present. Using this as an assessment of effective bandwidth, we limited frequency analysis within these bounds. Stable cavitation and inertial cavitation metrics are calculated by masking relevant frequency bands in S. The stable cavitation mask, SCM,

corresponded to ±10 kHz bands surrounding 0.5, 1.5, 2, 2.5 and 3 MHz. 10 kHz bands were chosen based on prior work by Pouliopolis and colleagues (Pouliopoulos et al. 2021). The inertial cavitation mask, ICM, spanned 1.1 MHz to 2.9 MHz excluding portions overlapping with the stable cavitation mask. Inertial cavitation dose, $ICD(n)$, and stable cavitation dose, $SCD(n)$, metrics were calculated for the nth pulse by:

$$ICD(n) = \frac{S(f,n) \cdot ICM}{\sum ICM} \tag{5.2}$$

$$SCD(n) = \frac{S(f,n) \cdot SCM}{\sum SCM} \tag{5.3}$$

Here $\cdot$ represents the dot product. We divide by the sum of the masks to normalize values such that $ICD(n)$ and $SCD(n)$ are not scaled by the different number of frequency points in both. Dynamic colormap windowing was necessary to visualize the spectrogram with sufficient contrast. We calculated a new lower and upper bound for the colormap with each pulse. The lower bound was equal to the average of the latest spectrogram column. The upper bound was equal to the average plus 3 standard deviations of the spectrogram column. Rather than automate pressure changes, we manually adjusted pressure during therapies because the signal amplitudes and qualities varied greatly from target to target.

Therapies overview

We performed twelve therapies in two macaques (one male, one female) over the course of five separate days. Targets were selected to investigate both BBB opening capabilities throughout the brain as well as BBB opening capability at the frontal eye field (FEF), the target this transducer was optimized for in the design stage (T. Manuel, Phipps, and Caskey 2022). Nine of the twelve therapy targets were cortical, with

four performed at the FEF. The other three targets were subcortical (two putamen, one caudate). A range of pressures were attempted with mean *in situ* pressures ranging from 0.4 to 1.4 MPa.

5.4 Results

Opening volume

Figure 5.4 shows percent change images generated from pre and post therapy T1-weighted images overlaid on T1-weighted anatomical images for three therapies from each target subgroup (subcortical, cortical, FEF only). Subcortical therapies resulted in enhancement at several cortical regions along the path to the

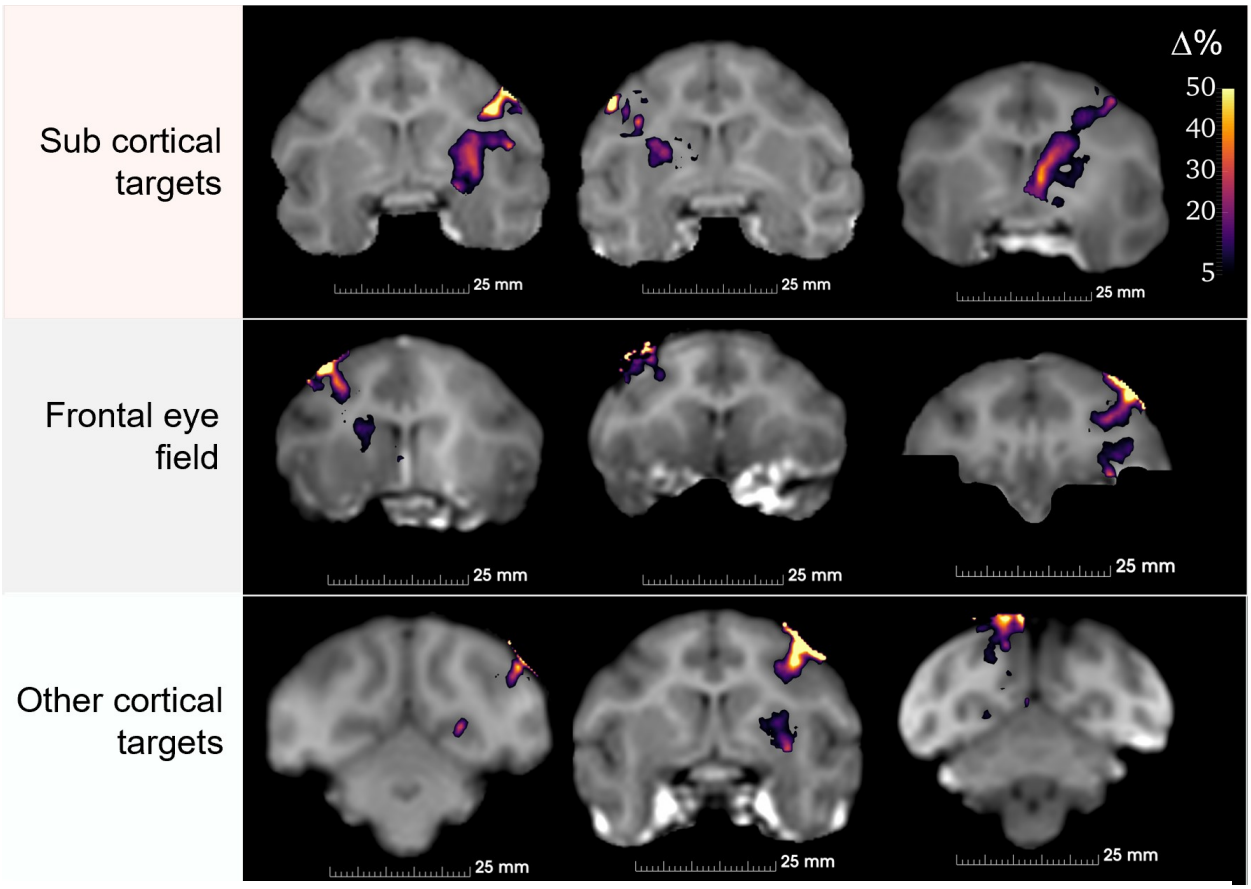

Figure 5.4. Percentage change images for nine BBB opening therapies separated into columns based on target groups. All colormaps match that shown in the top right. Subtraction images are overlaid on T1-weighted images from the same therapy.

transducer focus despite being outside the spot size of the transducer. Subcortical targets used the geometric focus of the transducer, rather than steered inward 10 mm. At the geometric focus the volume is 1.7 times larger and resulted in larger opening volumes. For some cortical targets, contrast enhancement can be seen in the subarachnoid space above the outermost grey matter as well as in grey matter regions, matching prior clinical results (Carpentier et al. 2016).

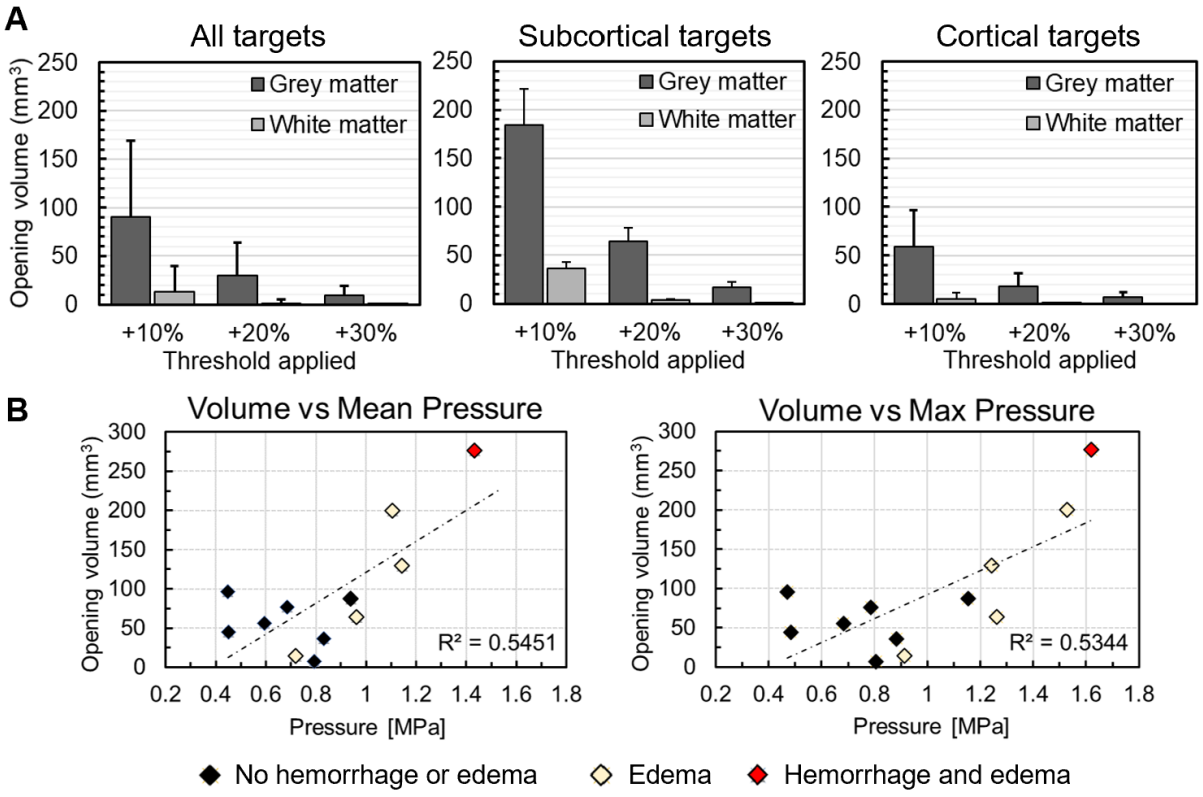

Figure 5.5. Opening volume results. A) Opening volume for all targets, subcortical targets, and cortical targets in grey and white matter. For each group opening volume is presented using a 10%, 20%, and 30% enhancement threshold. B) Opening volume compared to mean and maximum pressures used during therapies. Data points are color coded to indicate if edema or hemorrhage were detected.

The average tissue volume (grey + white matter) which experienced greater than 10% enhancement in post gadolinium T1-weighted images was 103 ± 101 mm^3. The opening volume at subcortical targets was 184

± 82 mm^3. The opening volume of cortical targets was 59 ± 37.3 mm^3. Figure 5.5 Panel A shows a breakdown of contrast enhancement between grey and white matter tissues separated into cortical and subcortical targets. 88% of opening was in grey matter when considering all targets. Figure 5.5 also displays volumetric enhancement at thresholds of 20% and 30%. The enhanced volume was 31 ± 9 mm^3 and 9 ± 10 mm^3 for 20% and 30% thresholds respectively. 97% of enhancement greater than 20% was in grey matter (excluding subarachnoid space, not included in analysis). We compared opening volumes against mean and maximum therapy pressure (Figure 5.5, Panel B). Opening volume increased with increased mean pressure (R^2 = 0.55) and increased maximum pressure (R^2 = 0.53).

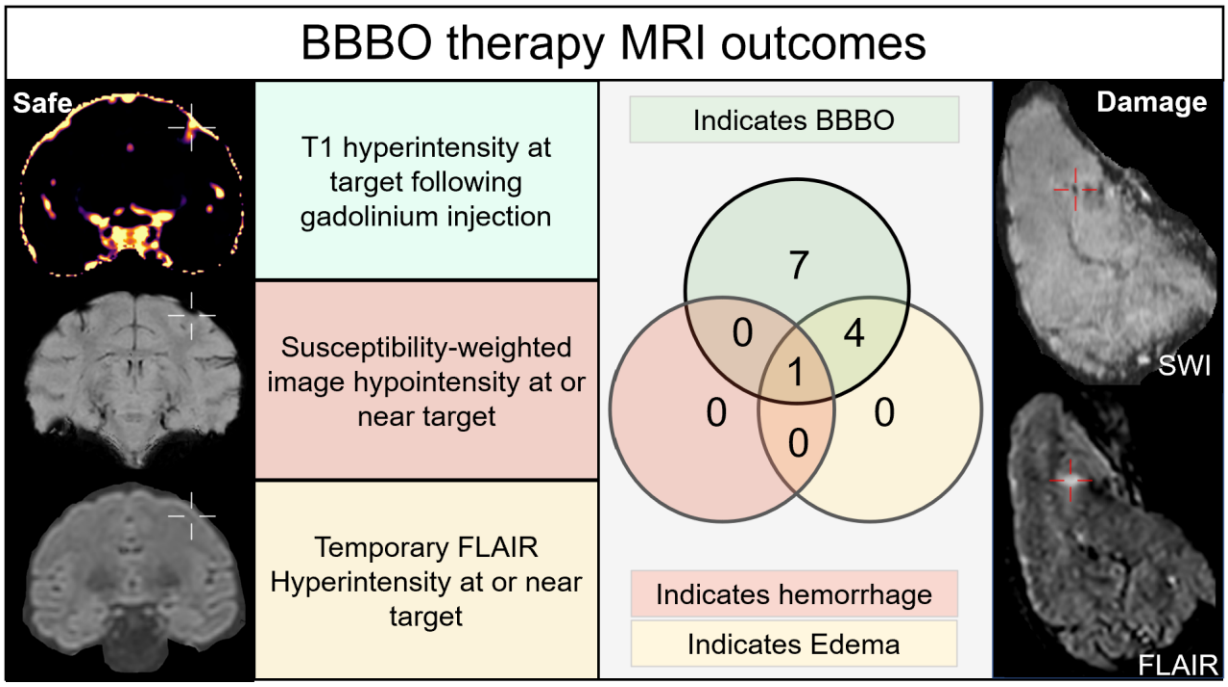

Figure 5.6. A breakdown of the MR contrasts used during therapies. T1-weighted images following gadolinium injection are sensitive to BBB opening. SWI images are sensitive to hemorrhage. FLAIR is sensitive to edema. Images on the left show one of the seven cases of opening where no SWI or FLAIR abnormalities were visible. The images on the right show the SWI and FLAIR images from the therapy which resulted in both edema and hemorrhage.

Safety evaluation

Of the twelve therapies, four exhibited temporary FLAIR hyperintensity at or near the same region as BBBO with no SWI darkening (Figure 5.6). Temporary FLAIR hyperintensity measured at short time delays following a therapy suggests edema occurred in these cases (Ho, Rojas, and Eisenberg 2012). One of the twelve therapies displayed permanent, localized SWI darkening and temporary FLAIR hyperintensity at the target indicating that both edema and extravasation of red blood cells (RBC) occurred. This case occurred in a subcortical target (caudate) at the highest pressure tested (1.4 MPa mean, 1.6 MPa max). Figure 5.5 distinguishes the datapoints corresponding to edema and/or RBC extravasation with yellow and red markers. The lowest pressure therapy which resulted in temporary edema was at a mean pressure of 0.7 MPa and a maximum pressure of 0.9 MPa. The other four cases which showed edema account for the four highest mean and maximum pressures tested (1.0 to 1.4 MPa mean, 1.3 to 1.6 MPa maximum). The SWI and FLAIR images from the high-pressure caudate therapy with both edema and RBC extravasation are displayed in Figure 5.6 with the target region highlighted by red crosshairs. All FLAIR hyperintensities were temporary with no hyperintense region persisting and displaying in the following scan. The corresponding minimum time between adjacent therapies in the same monkey was 3 weeks.

Cavitation monitoring tank measurements

The cavitation monitoring system was developed and tested in a water tank environment using a flow phantom setup with circulating microbubbles matching estimated *in vivo* bubble concentration in the blood. With no skull present, instantaneous stable cavitation dose (SCD) follows a roughly sigmoidal shape showing first increase around 0.35 MPa, rapidly increasing up to 0.7 MPa, and then leveling off at higher pressures. Inertial cavitation dose (ICD) increases starting at 0.5 MPa. Figure 5.7 (panel A) shows instantaneous cavitation doses with and without a degassed monkey skull present with pressures adjusted for skull transmission (35% transmission for this target). With the skull present, the cavitation signals are

largely attenuated. SCD levels at 0.6 MPa decrease from 22,090 in water only to 1,558 with the skull (93% decrease). An increase in SCD is observed from 0.5 to 0.8 MPa. ICD does not increase with increased pressure, despite being in pressure ranges known to produce inertial cavitation.

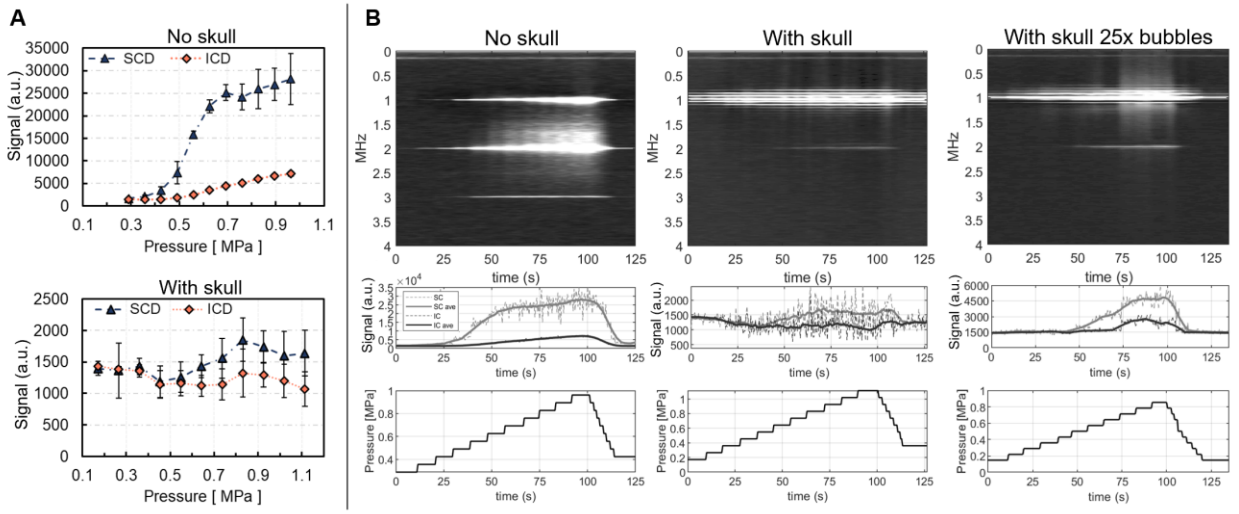

Figure 5.7. Cavitation measurements made in a microbubble flow phantom. A) Average cavitation signal plotted versus pressure for measurements made with and without a monkey skull in the beam path. B) Cavitation monitoring readouts with for no skull, with skull, and with skull + 25 times higher microbubble concentration than in vivo. The top row shows spectrograms; the middle row show plots of stable (SC) and inertial (IC) cavitation metrics vs. time; the bottom row shows pressure vs. time. Pressures through the skull fragment were adjusted based on 35% transmission.

Figure 5.7 (panel B) shows cavitation monitoring readouts for water tank measurements with no skull, with a skull, and with a skull using 25 times the estimated *in vivo* concentration of microbubbles. The top row of panel B are spectrograms showing dynamic baseline subtracted spectral content versus time. The second row shows stable cavitation and inertial cavitation metrics plotted with time. The dashed lines are the raw values, the bold lines are averaged with a ten-sample sliding window. The bottom row of panel B shows pressure versus time. Without the skull, stable cavitation is visible in the spectrogram and apparent in the

cavitation signal plot beginning at 0.35 MPa and increases with pressure. Inertial signal becomes visible in the spectrogram and cavitation dose plot beginning at 0.50 MPa and increases with pressure. With the skull, inertial cavitation signal is not visualized in the spectrogram nor apparent in the cavitation signal plots. Artifacts are visible around the fundamental frequency band. Some stable cavitation signal is apparent starting at 0.55 MPa.

Increasing the bubble concentration to 25 times the *in vivo* concentration has several effects on the cavitation readouts through the skull. The SCD amplitude increases by a factor of 3 approximately. ICD becomes clearly visible around 1.2 MHz in the spectrogram and in the cavitation signal plots starting at 0.70 MPa. The broadband ICD signal is concentrated at lower frequencies than in the no skull case likely due to frequency dependent attenuation.

Cavitation monitoring in vivo measurements

All BBBO therapies incorporated real-time cavitation monitoring facilitated by our custom software. Figure 5.8 shows a representation of the full range of data with four cases showing clear cavitation signal (Panel A) and four cases with low cavitation signal readout (Panel B) presented to display the range in signal qualities. The opening volume along with any adverse effects are shown above the accompanying data group. The main distinguishing factor between the Panel A and Panel B is that the Panel A groups show clear signal changes in the spectrogram and cavitation metric plots which temporally follow changes in applied pressure shown at the bottom of each group. In Panel B, the spectrogram and cavitation plots are unresponsive to changes in pressure. In all therapies, bubbles are slowly injected at the start of the therapy and arrive between 15 and 45 seconds. This arrival is visible in several of the spectrograms and cavitation metric plots.

In Panel A first therapy, we ramped the pressure from 0.3 to 1.1 MPa. SCD did not increase before ICD in this case. Seeing ICD increase, we reduced the pressure to 1 MPa. This therapy resulted in neither edema nor RBC extravasation. In Panel A 2nd therapy, we also ramped the pressure. As we ramped, we first noted an increase in SCD between 0.3 to 1.5 MPa. At the upper end of the pressure ramp, we noted ICD and

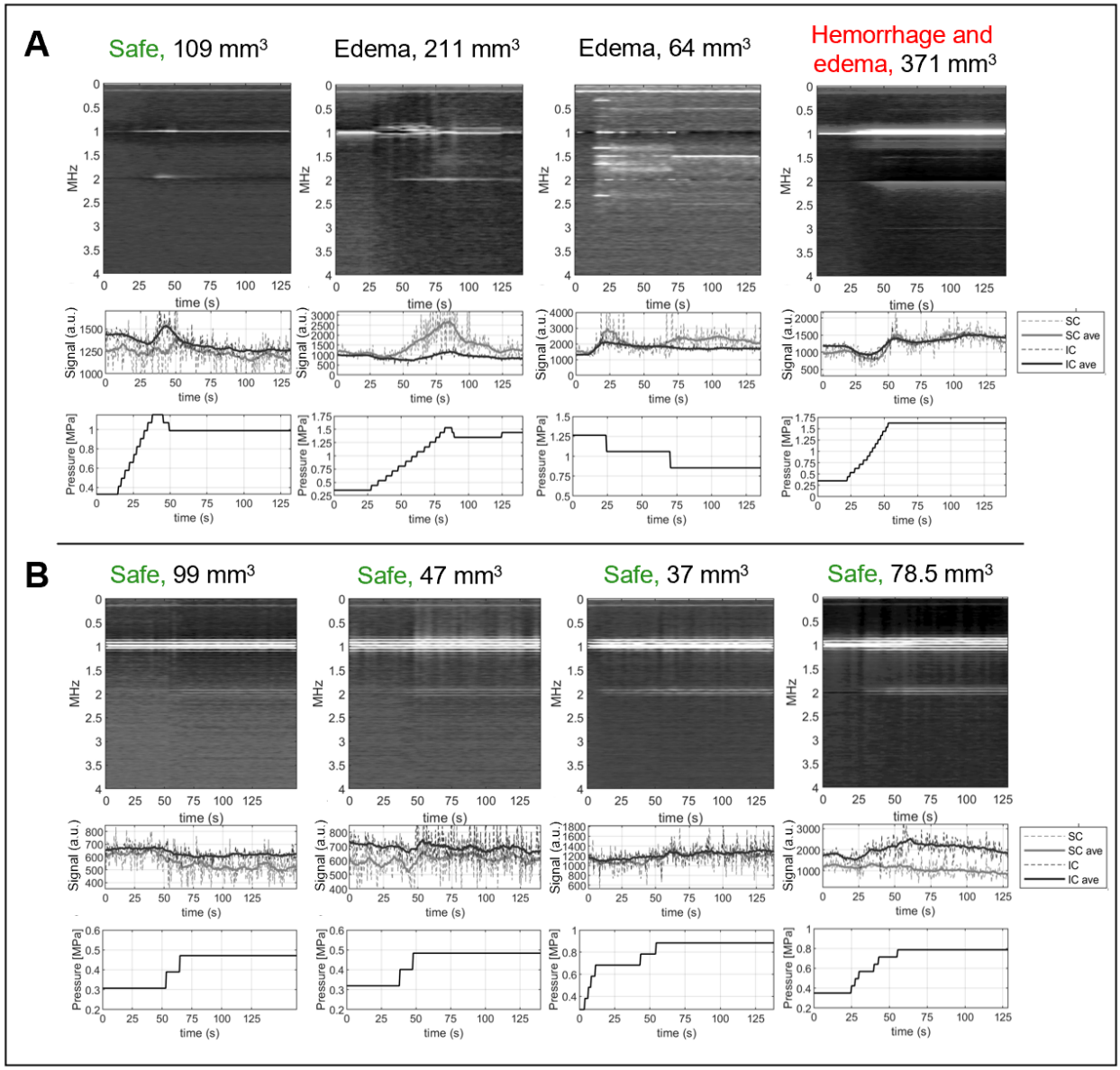

Figure 5.8. In vivo cavitation monitoring data from eight therapies. Above each therapy are outcomes based on safety scans and opening volume. A) Four therapies where cavitation signals change with pressure and help inform in situ pressure levels. B) Four lower pressure therapies where cavitation signals did not change with pressure and do not inform in situ pressure levels.

reduced the pressure. This therapy resulted in temporary edema in a small cortical region above the target (putamen, subcortical). In Panel A 3rd therapy, clear ultra-harmonics can be noted at the arrival of bubbles which occurred around 15 s into the therapy. Noting the presence increase in ICD also, we dropped the pressure until only SCD was visible. This case resulted in temporary edema. This case occurred early in experiment order and highlighted the need to ramp pressure starting at lower pressure (~0.4 MPa). For the rightmost case which generated edema and hemorrhage, we ramped the pressure from 0.4 to 1.6 MPa. ICD and SCD both increase starting at 1 MPa. The amplitude of this change was small and was not visible at the time of the therapy due to ineffective window and leveling in the spectrogram. As a result, the therapy pressure was left at a high value for the remainder of the procedure.

Panel B displays results from four lower pressure therapies with maximum pressures ranging between 0.5 MPa and 0.9 MPa. In these cases, the spectrograms and cavitation dose plots are largely unresponsive with changes in pressure. Artifacts seen in the spectrograms as horizontal lines are a product of the subtraction of baseline spectrograms combined with tight colormap windows approaching the noise floor. Despite having no discernable cavitation readout, all four of these therapies resulted in measurable gadolinium

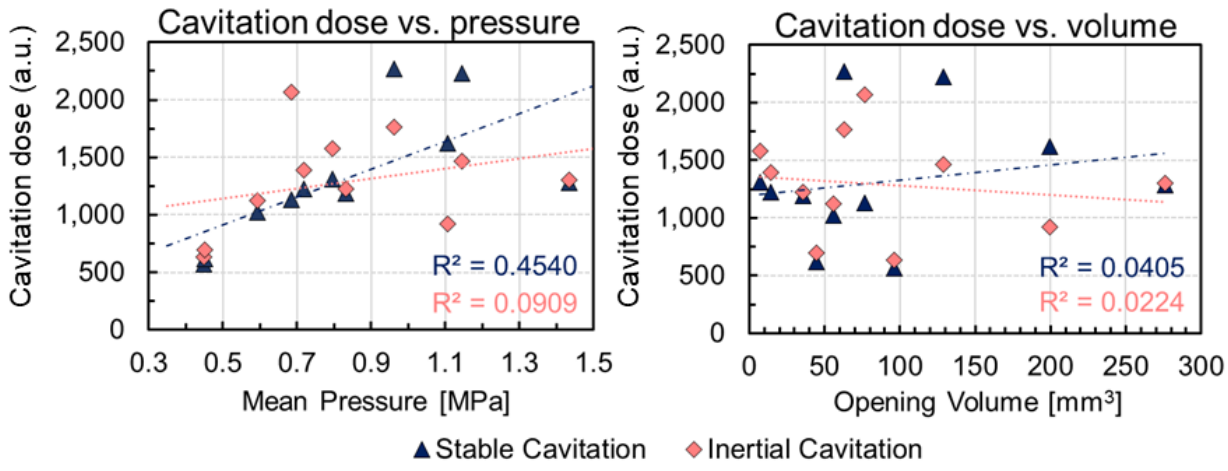

Figure 5.9. Cavitation dose compared to pressure and opening volume. Stable cavitation dose was partially correlated (R2 = .45) with pressure. All other comparisons were uncorrelated.

perfusion into regions around the target, indicating opening with no adverse effects indicated by SWI or FLAIR images. Figure 5.9 shows stable and inertial cavitation dose compared with mean therapy pressure and opening volume. Stable cavitation is correlated with mean therapy pressure ($R^2 = 0.56$). Other metrics are uncorrelated.

4.5 Discussion

FUS mediated BBB opening has emerged as a critical tool for delivery of therapeutics to the brain. Thus far studies have measured the safety of FUS BBB opening and the size and range of therapeutics able to transport across the permeabilized vasculature (Cammalleri et al. 2020; Song, Harvey, and Borden 2018). The volume of FUS BBB opening determines the extent of the therapy's effect. It is therefore desirable to achieve small focal spot sizes in applications that target small brain regions. In this work we tested a transducer optimized for small volume BBB opening in the macaque (T. Manuel, Phipps, and Caskey 2022) intended for gene therapy at the FEF to enable acoustically targeted chemogenetics (Szablowski et al. 2018). The transducer was successful in achieving small volume BBB opening with an average opening volume of 59 ±37 mm^3 and 184 ±82 mm^3 in cortical and subcortical targets respectively. Other studies in macaques report much larger opening volumes: (NHP 1 462.0± 193.4mm^3, NHP 2 605.3± 253.2mm^3 (Downs, Buch, Karakatsani, et al. 2015); 142 mm^3 to 854 mm^3 (M. E. M. Karakatsani et al. 2017); 100 to 600 mm^3 (S.-Y. Wu et al. 2018); 680 mm^3 to 1413 mm^3 (Pouliopoulos et al. 2021). By demonstrating that smaller volume opening is possible we have improved the spatial selectivity of FUS BBB opening to smaller targets.

Most measured opening occurred in grey matter with 92% of opening in grey at cortical targets and 84% at subcortical targets. Smaller increases in signal were measurable in white matter contiguous with grey matter opening sites. McDannold et al. found opening in white matter of macaques was not visible with gadolinium

imaging but was apparent with Evans blue dye (N. McDannold et al. 2012). On the other hand, (M. E. M. Karakatsani et al. 2017) found 80% of measured opening to be in grey matter and 20% in white matter. Across our results and these two studies, grey matter signal increase is brighter than white matter signal increase. This is attributed to the vascular differences in grey and white matter with grey matter being more perfused. Opening in white matter has been reported in humans in an Alzheimer's related clinical trial (Lipsman et al. 2018) and exclusively at the highest pressures studied in a glioblastoma clinical trial (Carpentier et al. 2016).

While the 1 MHz frequency allowed for a small transmit focus to be created, reception of echoes through the skull was challenging due to frequency-dependent attenuation. We identified multiple pressures where ultrasound induced BBB opening but did not generate significant increases in stable cavitation from baseline, making feedback difficult. Work by Wu et. al. investigated the effects of macaque and human skull on a cavitation monitoring system with a 500 kHz transmit frequency (S.-Y. Wu et al. 2014). They noted that the presence of skulls increased the pressure detection threshold for ultra-harmonic and inertial cavitation signals. We noted similar trends with our system in flow phantom measurements, and the effect will likely be more present with increasing frequency. Additionally, the skull produces strong reflections which impinge on the PCD during cavitation measurements. Increasing the transmit amplitude increases the amplitude of these reflections which have inherent harmonic content even in the absence of bubbles. Following methodologies proposed by Kamimura et. al we employed baseline subtractions using echoes acquired prior to microbubble administration (H. A. Kamimura et al. 2019). In the absence of baseline subtraction, ICD and SCD increase with increasing pressure even in the absence of microbubbles, presumably due to non-linear echoes from the skull. Although baseline subtraction helped isolate echoes arising from microbubbles, we were not able to detect all bubble activity.

The most similar systematic study of BBB opening parameters at 1 MHz (excluding small animals) is the work by Carpentier et. al, who quantified opening outcomes with a 1 MHz implant in humans at pressures from 0.5 to 1.1 MPa (Carpentier et al. 2016). 1 out of 11 patients demonstrated opening in grey matter at 0.8 MPa compared to 3 out of 7 at 0.95 MPa and 12 out of 14 at 1.1 MPa. We tested a pressure range which spanned these values plus additional range. Once hemorrhage was detected at an estimated mean pressure of 1.4 MPa with our system, no pressures at or above that range were tested again.

While our cavitation monitoring provided useful readouts for several therapies, when combined across trials cavitation doses did not correlate with opening volume or safety outcomes for our system. In a similar study with a 500 kHz transducer in macaques, cavitation metrics also did not correlate with opening volume (Marquet et al. 2014). In several cases shown in Figure 5.8, there are clear signatures of harmonic and broadband signals. However, the amplitude and characteristics of these features vary greatly from one therapy to another and are mostly absent at therapies which resulted in neither edema nor hemorrhage. A possible approach for therapy monitoring in future uses may be to ramp pressure up to 0.7 MPa *in situ*, at which point the therapy can progress so long as no harmonic or inertial signals are present. If either harmonic or inertial signals are present, this likely suggests higher than normal transmission and pressure should be reduced until the signals are absent. The geometric arrangement and frequency response of the cavitation monitor are known to be factors in sensitivity and could be improved upon to yield greater sensitivity

We measured temporary edema in 5 of 12 cases and hemorrhage in 1 of 12 cases. Temporary edema has been observed by others at lower pressures than hemorrhage and typically resolves within a week. Four instances of edema were measured in a safety study using 500 kHz between 200 and 400 kPa (Downs, Buch, Sierra, et al. 2015). Additionally, four instances of edema were reported at 500 kHz 300 kPa (Downs,

Buch, Karakatsani, et al. 2015). Both hemorrhage and edema were observed at 325 kPa, 500 kHz (H. A. Kamimura et al. 2019). In our case, four of the five cases of edema were observed at the four highest mean pressures applied (ranging from 1.0 to 1.4 MPa) which suggest using only lower pressures may avoid edema. However, there was a case of edema at a mean pressure of 0.7 MPa, max pressure 0.9 MPa. Rather than declare a hard threshold for edema, we note that at mean pressures below 0.9 MPa the instances of edema were 1/7 and fell to 0/4 below 0.7 MPa.

Transmission variance from target to target and subject to subject is unaccounted for in our analysis and likely contributes variance in opening volume, safety outcomes, and cavitation readouts. MR-ARFI may provide a means for accounting for this by sampling displacement prior to each therapy. Internal reflections likely give rise to complex pressure fields through the brain via standing wave formation given our long pulse length (10 ms) (Tang and Clement 2010; O'Reilly, Huang, and Hynynen 2010). Standing waves result in nodes of zero pressure and twice the pressure and may cause opening and/or damage despite low transmit amplitude. The distribution of microbubbles supplied by the vasculature is inhomogeneous in the brain which may partially decouple opening, edema, and hemorrhage from the spatial pressure field (Prada et al. 2021). For this reason, small changes in focus location alone may result in changes in opening volume and cavitation readout. Given the extent of skull attenuation on our cavitation signals, it is likely that incorporating a receive element at the half-harmonic (500 kHz) where attenuation is lower could yield better consistency of *in vivo* cavitation monitoring readouts in the presence of thick skulls. Subharmonics have been used successfully in mice for BBB opening cavitation monitoring (Burgess et al. 2014).

4.6 Conclusion

We tested a transducer optimized for small volume BBB opening in cortical targets in macaques and achieved opening at smaller volumes than previously reported. We characterized opening volume and safety outcomes across a range of pressures and targets, contributing new insight into BBB opening at 1 MHz in macaques. Cavitation monitoring with our 2 MHz receive element provided insight during some high-pressure therapies but had low SNR at lower pressure levels. This systems improves FUS BBB opening spatial specificity in macaques.

Chapter 6

Conclusion and future directions

6.1 Conclusion

The work described in this dissertation addresses challenges and questions at multiple fronts in the FUS space, particularly regarding brain applications. Here we identified several factors affecting ultrasound neuromodulation, including pulse repetition frequency and ion channel involvement. USN holds great potential as a research and therapy tool but often exhibits low magnitude, seemingly stochastic outcomes with large variance across models and studies. At the time of this work, there was cause for skepticism concerning USN given results from multiple groups demonstrating an auditory confound (Sato, Shapiro, and Tsao 2018; Guo et al. 2018) likely present in several foundational works (King et al. 2013; Tufail et al. 2010). With our neuromodulation study, we added to the body of literature demonstrating ultrasound neuromodulation in the absence of both heating and auditory confounds, fortifying the argument for a direct mechanism of action. Furthermore, our findings on increased modulation probability with certain pulse repetition frequencies have since been adopted and corroborated by several independent groups (Fomenko et al. 2020; Yu et al. 2021; Cheng et al. 2022), improving the robustness of outcomes and similarity of results across studies.

We also worked towards BBB opening capabilities of FUS. We designed a transducer for small volume blood brain barrier opening, which enables delivery of therapeutics to the brain while improving the spatial specificity of the technique. The design leveraged simulations in four macaques to incorporate transcranial evaluation of performance. Our design pushed the frequency of what has been used transcranially in large animals and used an inward steering technique to shrink the focal volume as much as possible within the

constraints of the design. We then calibrated the system, integrated it into an MRI guided workflow, and evaluated its performance *in vivo.* We built supporting software to monitor cavitation during the therapies in real-time. Comparing the performance of the monitoring in water tanks to in vivo highlighted areas for future research to improve the sensitivity and consistency of cavitation monitoring. This work brings the capabilities of ultrasound BBBO to Vanderbilt for future studies and with higher spatial selectivity than available elsewhere. This system will be used for non-invasive gene therapy in the macaque brain.

6.2 Future directions

6.2.1 Ultrasound neuromodulation

Pressing engineering problems remain with therapeutic ultrasound for neuromodulation and blood-brain barrier opening. With neuromodulation, important next steps for the field are to:

1) Corroborate and expand the growing consensus in the theory that mechanical stress leads to neuron excitation.

2) Identify the upper dose range of safe ultrasound parameters.

3) Evaluate through animal and human models the best suited applications of ultrasound neuromodulation.

1) Corroborate and expand ultrasound neuromodulation mechanism theories

A consensus is emerging on the mechanism of non-thermal ultrasound neuromodulation as being mechanical in nature but not requiring cavitation. Studies genetically knocking out mechanical ion channels in *c. elegans* (Kubanek et al. 2018), investigating specific ion channels in a single cell model (S. Yoo et al. 2022), and studying the effects of ion channel blockers (Tyler et al. 2008) all point to a mechanical link

between ultrasound, ion channel involvement, and neuron excitation. Advanced optical imaging techniques may be able to corroborate mechanical interactions with imaging readouts at higher spatiotemporal resolution in synthetic liposomes, engineered cells, or in intact brain models. It is worthwhile to continue adding to the available data surrounding this topic because ultrasound parameter designs can be informed by the underlying principles at work.

The mechanical mechanism theory for ultrasound neuromodulation can build upon physical models of acoustic radiation force and acoustic streaming mentioned in chapter 1 to describe the immediate physical link between ultrasound and cellular structures. However, the theory needs to be expanded upon in the cellular signaling space to include populations of neurons rather than single cells, specific types of nervous system cells (glial cells, astrocytes, neurons), and state-dependence (i.e. how cell history and current cell excitability play into outcomes). *In vivo,* ultrasound stimulates populations of neurons and produces a bulk effect. Observations reporting inhibition from ultrasound may be due to ultrasound stimulating circuit nodes which themselves suppress a downstream node. The differences in the signaling effects of ultrasound in different cell types remains a question which if answered would add a level of dimensionality to the ultrasound neuromodulation as a tool. The mechanisms accounting for the longer term effects like reduced somatosensory evoked potentials which lasted more than 10 minutes need to be evaluated and linked to ultrasound parameter selection (Dallapiazza et al. 2017).

2) Identify the upper dose range for safe neuromodulation

Most parametric studies point to an intensity dependence on ultrasound neuromodulation probability. From this it can be concluded that to maximize neuromodulatory effects, ultrasound dose should be applied at the highest intensity level which does not produce adverse effects (although some works which suggest inhibitory vs. excitatory effects at different ultrasound levels may refute this). Potential adverse effects

highlighted in chapter 1 include heating and cavitation related damage. The risk of cavitation has been well studied in tissue and is proportional to the mechanical index of a pulse as described in section 2.1.2.2. Pulse designs can avoid cavitation by simply keeping peak-negative pressures below the cavitation threshold of tissue. Tissue heating from ultrasound has also been well studied and can be modeled as described in section 2.1.2.1. However, avoiding thermal effects is where pulse design has several parameters to tune which may maximize neuromodulation outcomes. It has been shown by our group as well as many other (table 2.1) that pulsed ultrasound is effective for neuromodulation. Pulsed ultrasound enables lowering the pulse duty cycle which lowers the temporal-average intensity and in turn heating. It may be the case that low enough duty cycles enable using pressures right up to the cavitation threshold for long periods of stimulation without concern for heating. It would be useful to see this evaluated in an animal model with behavioral or electrophysiology measurements of efficacy coupled with histology safety measures.

3) Evaluate the best suited disease candidates for neuromodulation

Apart from using ultrasound neuromodulation as a tool for probing neural circuits, ultrasound neuromodulation may have applications in treating diseases such as chronic pain, addiction, depression, and essential tremor. Many investigations using ultrasound neuromodulation are underway (for a recent review, see (Darmani et al. 2022)). Most early studies have sought links to immediately observable effects of ultrasound like tactile sensations, fMRI BOLD signals, and visual perceptions. However, disease oriented work has begun including testing ultrasound neuromodulation in disorders of consciousness (Monti et al. 2016), pain (Badran et al. 2020), and depression (Reznik et al. 2020). The primary benefit of ultrasound over other non-invasive stimulation tools is its spatial precision and ability to reach deep targets. However, to make an impact on standard of care, the next generation of studies will need to demonstrate that ultrasound neuromodulation leads to improvements in patient outcomes. Perhaps the most exciting target to aim for is long lasting effects from ultrasound stimulation with regard to some disease symptom. Long-

lasting effects will increase the viability of the technology by reducing the number and frequency of treatments required.

6.2.2 Blood-brain barrier opening

There are several immediate future directions for the BBBO project described in this dissertation which focus on improving the safety and consistency of the BBBO system as well as using it for its intended purpose, gene therapy. First is to increase the sensitivity of our system's cavitation monitoring receive capabilities. *In vivo* and *ex vivo* skull phantom data in section 4.4 show that our cavitation signals are greatly masked by skull attenuation. This challenge is common in cavitation monitoring systems operating in humans and macaques. While we cannot easily change the receive element on the transducer, we could add a separate transducer to the procedure. Separate receive transducers are used by several groups (O'Reilly and Hynynen 2010; N. McDannold et al. 2012). The added sensitivity of an additional receiver may be enough to improve the consistency of our current cavitation monitoring approach. It may be beneficial to test a receive element centered on 500 kHz (the half-harmonic) as this lower frequency content will be less attenuated by the skull. It is also possible to dedicate several of the array transmit elements as receivers. This could improve the overall sensitivity of the system without acquiring a new transducer. The array produces an excess of power over what is needed for BBBO and could likely achieve adequate focal pressure and spot size with several central elements allocated to receiving only. Apart from directly improving our system, identifying techniques to improve cavitation monitoring sensitivity would move the field forward and improve BBB opening safety and consistency.

The performance of our cavitation monitoring may be improved by adopting a different strategy for feedback. Currently, we perform manual adjustments of pressures based on real-time signals visualized throughout therapy as was done previously (Arvanitis et al. 2012). This approach offered the most flexibility

and served well for our initial evaluation of the system. However, the *in vivo* data has revealed that at safe therapy levels where cavitation is occurring, it is often the case that no cavitation signals are detected. Several approaches to address this have been put forward by the field (McMahon, Poon, and Hynynen 2019). One approach which seems well suited to low SNR cases is to acquire an initial pressure ramp of test pulses with bubbles circulating. From the test pulses, the therapy pressure could be chosen as a fraction of the lowest pressure pulse which produced visible cavitation signals. This requires potentially subjecting the patient to a low number of unsafe pressures during test pulses, but our *in vivo* data suggests that small durations of excess pressure do not lead to adverse effects.

A third area of future work discussed in chapter 5 and common to the field is to link measurable factors to the variances opening volume outcomes. We saw a variation of ± 63% and ± 45% in cortical and subcortical BBB opening volumes. Table 2.2 illustrates that this amount of variance is common, and studies have suggested pressure, incidence angle, and microbubble concentration contribute to the variance in outcome. Using patient specific transcranial simulations of the *in vivo* procedures in chapter 5, it should be possible to estimate effects of incidence angle and delivered pressure for each procedure. Furthermore, the target location can be co-registered with segmented anatomical MRI scans to infer relative microbubble delivery based on grey matter / white matter ratio at the acoustic focus. By combining simulations and anatomical measures, we can likely account for a portion of the variation observed in our *in vivo* procedures. Accounting for this variation will be important in future efforts to improve the spatial specificity of our system for BBB opening and would contribute to the field by predicting and perhaps avoiding variation in procedural outcomes.

Finally, the system should be tested for its intended application, gene therapy. Gene therapy enabled by ultrasound BBBO is one of the more promising applications because of its non-invasive, non-destructive

yet permanent therapeutic potential. FUS BBB opening can reduce the required dose of viral vectors for adequate brain transfection by a factor of 100 which improves peripheral transfection (Noroozian et al. 2019). So far, the evaluated performance of our system and many others has been based on increased gadolinium delivery. Gene therapy requires the delivery of large (~2 kDa) molecules which will have lower perfusion at the same BBB opening parameters compared to gadolinium (H. Chen and Konofagou 2014). Because of the higher pressure required for viral vector delivery, the safety margin between adequate opening and adverse effects will be thin. Improvements in the cavitation monitoring system discussed here in future directions and in chapter 5.5 will be key to consistently hit the safe pressure window and delivery adequate viral load into the brain parenchyma.

Bibliography

Abbott, N. Joan. 2005. “Physiology of the Blood–Brain Barrier and Its Consequences for Drug Transport to the Brain.” *International Congress Series*, Drug Transport(ers) and the Diseased Brain, 1277 (April): 3–18. https://doi.org/10.1016/j.ics.2005.02.008.

Abrahao, Agessandro, Ying Meng, Maheleth Llinas, Yuexi Huang, Clement Hamani, Todd Mainprize, Isabelle Aubert, et al. 2019. “First-in-Human Trial of Blood–Brain Barrier Opening in Amyotrophic Lateral Sclerosis Using MR-Guided Focused Ultrasound.” *Nature Communications* 10 (1): 1–9.

Adams, Chris, Ryan M. Jones, Steven D. Yang, Wai Meng Kan, Kogee Leung, Yuheng Zhou, Kang Uk Lee, Yuexi Huang, and Kullervo Hynynen. 2021. “Implementation of a Skull-Conformal Phased Array for Transcranial Focused Ultrasound Therapy.” *IEEE Transactions on Biomedical Engineering* 68 (11): 3457–68. https://doi.org/10.1109/TBME.2021.3077802.

Alam, Murad, Lucile E. White, Nicolle Martin, Joslyn Witherspoon, Simon Yoo, and Dennis P. West. 2010. “Ultrasound Tightening of Facial and Neck Skin: A Rater-Blinded Prospective Cohort Study.” *Journal of the American Academy of Dermatology* 62 (2): 262–69. https://doi.org/10.1016/j.jaad.2009.06.039.

Apfel, RE. 1982. “Acoustic Cavitation: A Possible Consequence of Biomedical Uses of Ultrasound.” *The British Journal of Cancer. Supplement* 5: 140.

Armulik, Annika, Guillem Genové, Maarja Mäe, Maya H. Nisancioglu, Elisabet Wallgard, Colin Niaudet, Liqun He, et al. 2010. “Pericytes Regulate the Blood–Brain Barrier.” *Nature* 468 (7323): 557–61. https://doi.org/10.1038/nature09522.

Arvanitis, Costas D., Margaret S. Livingstone, Natalia Vykhodtseva, and Nathan McDannold. 2012. “Controlled Ultrasound-Induced Blood-Brain Barrier Disruption Using Passive Acoustic Emissions Monitoring.” *PLOS ONE* 7 (9): e45783. https://doi.org/10.1371/journal.pone.0045783.

Aslani, Pegah, Leah Drost, Yuexi Huang, Benjamin B. C. Lucht, Erin Wong, Gregory Czarnota, Caitlin Yee, et al. 2020. “Thermal Therapy With a Fully Electronically Steerable HIFU Phased Array Using Ultrasound Guidance and Local Harmonic Motion Monitoring.” *IEEE Transactions on Biomedical Engineering* 67 (7): 1854–62. https://doi.org/10.1109/TBME.2019.2949478.

Aubry, J.-F., M. Tanter, M. Pernot, J.-L. Thomas, and M. Fink. 2003. “Experimental Demonstration of Noninvasive Transskull Adaptive Focusing Based on Prior Computed Tomography Scans.” *The Journal of the Acoustical Society of America* 113 (1): 84–93. https://doi.org/10.1121/1.1529663.

Badran, Bashar W, Kevin A Caulfield, Sasha Stomberg-Firestein, Philipp M Summers, Logan T Dowdle, Matt Savoca, Xingbao Li, et al. 2020. “Sonication of the Anterior Thalamus with MRI-Guided Transcranial Focused Ultrasound (TFUS) Alters Pain Thresholds in Healthy Adults: A Double-Blind, Sham-Controlled Study.” *Brain Stimulation* 13 (6): 1805–12.

Beisteiner, Roland, Eva Matt, Christina Fan, Heike Baldysiak, Marleen Schönfeld, Tabea Philippi Novak, Ahmad Amini, et al. 2019. “Transcranial Pulse Stimulation with Ultrasound in Alzheimer’s Disease—A New Navigated Focal Brain Therapy.” *Advanced Science* n/a (n/a): 1902583. https://doi.org/10.1002/advs.201902583.

Bender, M. A. 1955. “Blood Volume of the Rhesus Monkey.” *Science* 122 (3160): 156–156. https://doi.org/10.1126/science.122.3160.156.a.

Beyer, RT. 1997. “The Parameter B/A,[in:] Nonlinear Acoustics, MF Hamilton, DT Blackstock.” *Academic Press* 25: 40.

Bing, Kristin Frinkley, Gabriel P. Howles, Yi Qi, Mark L. Palmeri, and Kathryn R. Nightingale. 2009. “Blood-Brain Barrier (BBB) Disruption Using a Diagnostic Ultrasound Scanner and Definity® in Mice.”

Ultrasound in Medicine & Biology 35 (8): 1298–1308. https://doi.org/10.1016/j.ultrasmedbio.2009.03.012.

Blackmore, Joseph, Shamit Shrivastava, Jerome Sallet, Chris R. Butler, and Robin O. Cleveland. 2019. "Ultrasound Neuromodulation: A Review of Results, Mechanisms and Safety." *Ultrasound in Medicine & Biology* 45 (7): 1509–36. https://doi.org/10.1016/j.ultrasmedbio.2018.12.015.

Bojarski, Norbert N. 1982. "The K-Space Formulation of the Scattering Problem in the Time Domain." *The Journal of the Acoustical Society of America* 72 (2): 570–84.

Brenner, Kevin, Arif Sanli Ergun, Kamyar Firouzi, Morten Fischer Rasmussen, Quintin Stedman, and Butrus (Pierre) Khuri–Yakub. 2019. "Advances in Capacitive Micromachined Ultrasonic Transducers." *Micromachines* 10 (2): 152. https://doi.org/10.3390/mi10020152.

Brody, Debra J, Laura A Pratt, and Jeffery P Hughes. 2018. "Prevalence of Depression among Adults Aged 20 and over: United States, 2013-2016."

Burgess, Alison, Sonam Dubey, Sharon Yeung, Olivia Hough, Naomi Eterman, Isabelle Aubert, and Kullervo Hynynen. 2014. "Alzheimer Disease in a Mouse Model: MR Imaging–Guided Focused Ultrasound Targeted to the Hippocampus Opens the Blood-Brain Barrier and Improves Pathologic Abnormalities and Behavior." *Radiology* 273 (3): 736–45. https://doi.org/10.1148/radiol.14140245.

Cammalleri, Amanda, Phillip Croce, Wonhye Lee, Kyungho Yoon, and Seung-Schik Yoo. 2020. "Therapeutic Potentials of Localized Blood-Brain Barrier Disruption by Non-Invasive Transcranial Focused Ultrasound: A Technical Review." *Journal of Clinical Neurophysiology : Official Publication of the American Electroencephalographic Society* 37 (2): 104–17. https://doi.org/10.1097/WNP.0000000000000488.

Carpentier, Alexandre, Michael Canney, Alexandre Vignot, Vincent Reina, Kevin Beccaria, Catherine Horodyckid, Carine Karachi, et al. 2016. "Clinical Trial of Blood-Brain Barrier Disruption by Pulsed Ultrasound." *Science Translational Medicine* 8 (343): 343re2-343re2. https://doi.org/10.1126/scitranslmed.aaf6086.

Caskey, Charles F., Shengping Qin, Paul A. Dayton, and Katherine W. Ferrara. 2009. "Microbubble Tunneling in Gel Phantoms." *The Journal of the Acoustical Society of America* 125 (5): EL183–89. https://doi.org/10.1121/1.3097679.

Caskey, Charles F., Susanne M. Stieger, Shengping Qin, Paul A. Dayton, and Katherine W. Ferrara. 2007. "Direct Observations of Ultrasound Microbubble Contrast Agent Interaction with the Microvessel Wall." *The Journal of the Acoustical Society of America* 122 (2): 1191–1200. https://doi.org/10.1121/1.2747204.

Chapelon, Jean-Yves, Dominique Cathignol, Charles Cain, Emad Ebbini, Jan-Ulco Kluiwstra, Oleg A Sapozhnikov, Gérard Fleury, Rémi Berriet, Laurent Chupin, and Jean-Luc Guey. 2000. "New Piezoelectric Transducers for Therapeutic Ultrasound." *Ultrasound in Medicine & Biology* 26 (1): 153–59. https://doi.org/10.1016/S0301-5629(99)00120-9.

Chaplin, V., M. A. Phipps, S. V. Jonathan, W. A. Grissom, P. F. Yang, L. M. Chen, and C. F. Caskey. 2019. "On the Accuracy of Optically Tracked Transducers for Image-Guided Transcranial Ultrasound." *International Journal of Computer Assisted Radiology and Surgery* 14 (8): 1317–27. https://doi.org/10.1007/s11548-019-01988-0.

Chaplin, Vandiver, Marshal A Phipps, and Charles F Caskey. 2018. "A Random Phased-Array for MR-Guided Transcranial Ultrasound Neuromodulation in Non-Human Primates." *Physics in Medicine & Biology* 63 (10): 105016. https://doi.org/10.1088/1361-6560/aabeff.

Chen, Hong, and Elisa E Konofagou. 2014. "The Size of Blood–Brain Barrier Opening Induced by Focused Ultrasound Is Dictated by the Acoustic Pressure." *Journal of Cerebral Blood Flow & Metabolism* 34 (7): 1197–1204. https://doi.org/10.1038/jcbfm.2014.71.

Chen, Ko-Ting, Ya-Jui Lin, Wen-Yen Chai, Chia-Jung Lin, Pin-Yuan Chen, Chiung-Yin Huang, John S Kuo, Hao-Li Liu, and Kuo-Chen Wei. 2020. "Neuronavigation-Guided Focused Ultrasound (NaviFUS) for Transcranial Blood-Brain Barrier Opening in Recurrent Glioblastoma Patients: Clinical Trial Protocol." *Annals of Translational Medicine* 8 (11).

Chen, L, G ter Haar, C R Hill, M Dworkin, P Carnochan, H Young, and J P M Bensted. 1993. "Effect of Blood Perfusion on the Ablation of Liver Parenchyma with High-Intensity Focused Ultrasound." *Physics in Medicine and Biology* 38 (11): 1661–73. https://doi.org/10.1088/0031-9155/38/11/011.

Chen, Tsai-Wen, Trevor J. Wardill, Yi Sun, Stefan R. Pulver, Sabine L. Renninger, Amy Baohan, Eric R. Schreiter, et al. 2013. "Ultra-Sensitive Fluorescent Proteins for Imaging Neuronal Activity." *Nature* 499 (7458): 295–300. https://doi.org/10.1038/nature12354.

Cheng, Zongyue, Chenmao Wang, Bowen Wei, Wenbiao Gan, Qifa Zhou, and Meng Cui. 2022. "High Resolution Ultrasonic Neural Modulation Observed via in Vivo Two-Photon Calcium Imaging." *Brain Stimulation* 15 (1): 190–96.

Chien, Chih-Yen, Yan Gong, Yaoheng Yang, Yimei Yue, and Hong Chen. 2021. "Reliable and Safe Blood–Brain Barrier Opening by Closed-Loop Feedback Control of Focused Ultrasound." *The Journal of the Acoustical Society of America* 150 (4): A30–A30. https://doi.org/10.1121/10.0007518.

Chiueh, CC, CL Sun, IJ Kopin, WR Fredericks, and SI Rapoport. 1978. "Entry of [3H] Norepinephrine,[125I] Albumin and Evans Blue from Blood into Brain Following Unilateral Osmotic Opening of the Blood-Brain Barrier." *Brain Research* 145 (2): 291–301.

Choi, James J., Shougang Wang, Yao-Sheng Tung, Barclay Morrison, and Elisa E. Konofagou. 2010. "Molecules of Various Pharmacologically-Relevant Sizes Can Cross the Ultrasound-Induced Blood-Brain Barrier Opening in Vivo." *Ultrasound in Medicine & Biology* 36 (1): 58–67. https://doi.org/10.1016/j.ultrasmedbio.2009.08.006.

Chopra, Rajiv, Alexandra Colquhoun, Mathieu Burtnyk, William A. N'djin, Ilya Kobelevskiy, Aaron Boyes, Kashif Siddiqui, et al. 2012. "MR Imaging–Controlled Transurethral Ultrasound Therapy for Conformal Treatment of Prostate Tissue: Initial Feasibility in Humans." *Radiology* 265 (1): 303–13. https://doi.org/10.1148/radiol.12112263.

Clement, G. T., and K. Hynynen. 2002. "A Non-Invasive Method for Focusing Ultrasound through the Human Skull." *Physics in Medicine and Biology* 47 (8): 1219–36. https://doi.org/10.1088/0031-9155/47/8/301.

Clement, G. T., Jie Sun, Tonia Giesecke, and Kullervo Hynynen. 2000. "A Hemisphere Array for Non-Invasive Ultrasound Brain Therapy and Surgery." *Physics in Medicine and Biology* 45 (12): 3707–19. https://doi.org/10.1088/0031-9155/45/12/314.

Connor, Christopher W, Greg T Clement, and Kullervo Hynynen. 2002. "A Unified Model for the Speed of Sound in Cranial Bone Based on Genetic Algorithm Optimization." *Physics in Medicine and Biology* 47 (22): 3925–44. https://doi.org/10.1088/0031-9155/47/22/302.

Constans, Charlotte, Harry Ahnine, Mathieu Santin, Stéphane Lehericy, Mickael Tanter, Pierre Pouget, and Jean-François Aubry. 2020. "Non-Invasive Ultrasonic Modulation of Visual Evoked Response by GABA Delivery through the Blood Brain Barrier." *Journal of Controlled Release* 318 (February): 223–31. https://doi.org/10.1016/j.jconrel.2019.12.006.

Costley, David, Conor Mc Ewan, Colin Fowley, Anthony P. McHale, Jordan Atchison, Nikolitsa Nomikou, and John F. Callan. 2015. "Treating Cancer with Sonodynamic Therapy: A Review." *International Journal of Hyperthermia* 31 (2): 107–17. https://doi.org/10.3109/02656736.2014.992484.

Curley, Colleen T., Natasha D. Sheybani, Timothy N. Bullock, and Richard J. Price. 2017. "Focused Ultrasound Immunotherapy for Central Nervous System Pathologies: Challenges and Opportunities." *Theranostics* 7 (15): 3608–23. https://doi.org/10.7150/thno.21225.

Dallapiazza, Robert F, Kelsie F Timbie, Stephen Holmberg, Jeremy Gatesman, M Beatriz Lopes, Richard J Price, G Wilson Miller, and W Jeffrey Elias. 2017. “Noninvasive Neuromodulation and Thalamic Mapping with Low-Intensity Focused Ultrasound.” *Journal of Neurosurgery* 128 (3): 875–84.

Darmani, G., T. O. Bergmann, K. Butts Pauly, C. F. Caskey, L. de Lecea, A. Fomenko, E. Fouragnan, et al. 2022. “Non-Invasive Transcranial Ultrasound Stimulation for Neuromodulation.” *Clinical Neurophysiology* 135 (March): 51–73. https://doi.org/10.1016/j.clinph.2021.12.010.

Deffieux, Thomas, Youliana Younan, Nicolas Wattiez, Mickael Tanter, Pierre Pouget, and Jean-François Aubry. 2013. “Low-Intensity Focused Ultrasound Modulates Monkey Visuomotor Behavior.” *Current Biology* 23 (23): 2430–33. https://doi.org/10.1016/j.cub.2013.10.029.

Deng, Lulu, Meaghan A O’Reilly, Ryan M Jones, Ran An, and Kullervo Hynynen. 2016. “A Multi-Frequency Sparse Hemispherical Ultrasound Phased Array for Microbubble-Mediated Transcranial Therapy and Simultaneous Cavitation Mapping.” *Physics in Medicine and Biology* 61 (24): 8476–8501. https://doi.org/10.1088/0031-9155/61/24/8476.

Doinikov, Alexander A., and Ayache Bouakaz. 2011. “Review of Shell Models for Contrast Agent Microbubbles.” *IEEE Transactions on Ultrasonics, Ferroelectrics, and Frequency Control* 58 (5): 981–93. https://doi.org/10.1109/TUFFC.2011.1899.

Downs, Matthew E., Amanda Buch, Maria Eleni Karakatsani, Elisa E. Konofagou, and Vincent P. Ferrera. 2015. “Blood-Brain Barrier Opening in Behaving Non-Human Primates via Focused Ultrasound with Systemically Administered Microbubbles.” *Scientific Reports* 5 (1): 15076. https://doi.org/10.1038/srep15076.

Downs, Matthew E., Amanda Buch, Carlos Sierra, Maria Eleni Karakatsani, Shangshang Chen, Elisa E. Konofagou, and Vincent P. Ferrera. 2015. “Long-Term Safety of Repeated Blood-Brain Barrier Opening via Focused Ultrasound with Microbubbles in Non-Human Primates Performing a Cognitive Task.” *PLOS ONE* 10 (5): e0125911. https://doi.org/10.1371/journal.pone.0125911.

Duck, Francis A. 2013. *Physical Properties of Tissues: A Comprehensive Reference Book*. Academic Press.

Ebbini, Emad S., Hui Yao, and Ajay Shrestha. 2006. “Dual-Mode Ultrasound Phased Arrays for Image-Guided Surgery.” *Ultrasonic Imaging* 28 (2): 65–82. https://doi.org/10.1177/016173460602800201.

Ebbini, E.S., and C.A. Cain. 1989. “Multiple-Focus Ultrasound Phased-Array Pattern Synthesis: Optimal Driving-Signal Distributions for Hyperthermia.” *IEEE Transactions on Ultrasonics, Ferroelectrics, and Frequency Control* 36 (5): 540–48. https://doi.org/10.1109/58.31798.

———. 1991. “A Spherical-Section Ultrasound Phased Array Applicator for Deep Localized Hyperthermia.” *IEEE Transactions on Biomedical Engineering* 38 (7): 634–43. https://doi.org/10.1109/10.83562.

Edmonds, Peter D, and Kenneth M Sancier. 1983. “Evidence for Free Radical Production by Ultrasonic Cavitation in Biological Media.” *Ultrasound in Medicine & Biology* 9 (6): 635–39.

Ellens, Nicholas, Aki Pulkkinen, Junho Song, and Kullervo Hynynen. 2011. “The Utility of Sparse 2D Fully Electronically Steerable Focused Ultrasound Phased Arrays for Thermal Surgery: A Simulation Study.” *Physics in Medicine and Biology* 56 (15): 4913–32. https://doi.org/10.1088/0031-9155/56/15/017.

Faria, Paula, Mark Hallett, and Pedro Cavaleiro Miranda. 2011. “A Finite Element Analysis of the Effect of Electrode Area and Inter-Electrode Distance on the Spatial Distribution of the Current Density in TDCS.” *Journal of Neural Engineering* 8 (6): 066017.

Ferraris, Chiara, Roberta Cavalli, Pier Paolo Panciani, and Luigi Battaglia. 2020. “Overcoming the Blood–Brain Barrier: Successes and Challenges in Developing Nanoparticle-Mediated Drug Delivery Systems for the Treatment of Brain Tumours.” *International Journal of Nanomedicine* Volume 15 (April): 2999–3022. https://doi.org/10.2147/IJN.S231479.

Fisher, Jonathan AN, and Iryna Gumenchuk. 2018. “Low-Intensity Focused Ultrasound Alters the Latency and Spatial Patterns of Sensory-Evoked Cortical Responses in Vivo.” *Journal of Neural Engineering* 15 (3): 035004.

Fitzpatrick, J.M., J.B. West, and C.R. Maurer. 1998. “Predicting Error in Rigid-Body Point-Based Registration.” *IEEE Transactions on Medical Imaging* 17 (5): 694–702. https://doi.org/10.1109/42.736021.

Folloni, Davide, Lennart Verhagen, Rogier B. Mars, Elsa Fouragnan, Charlotte Constans, Jean-François Aubry, Matthew F. S. Rushworth, and Jérôme Sallet. 2019. “Manipulation of Subcortical and Deep Cortical Activity in the Primate Brain Using Transcranial Focused Ultrasound Stimulation.” *Neuron* 101 (6): 1109-1116.e5. https://doi.org/10.1016/j.neuron.2019.01.019.

Fomenko, Anton, Kai-Hsiang Stanley Chen, Jean-François Nankoo, James Saravanamuttu, Yanqiu Wang, Mazen El-Baba, Xue Xia, et al. 2020. “Systematic Examination of Low-Intensity Ultrasound Parameters on Human Motor Cortex Excitability and Behavior.” *Elife* 9: e54497.

Foster, F.S., K.A. Harasiewicz, and M.D. Sherar. 2000. “A History of Medical and Biological Imaging with Polyvinylidene Fluoride (PVDF) Transducers.” *IEEE Transactions on Ultrasonics, Ferroelectrics, and Frequency Control* 47 (6): 1363–71. https://doi.org/10.1109/58.883525.

Fry, F. J., H. W. Ades, and W. J. Fry. 1958. “Production of Reversible Changes in the Central Nervous System by Ultrasound.” *Science* 127 (3289): 83–84.

Gaub, Benjamin M., Krishna Chaitanya Kasuba, Emilie Mace, Tobias Strittmatter, Pawel R. Laskowski, Sydney A. Geissler, Andreas Hierlemann, Martin Fussenegger, Botond Roska, and Daniel J. Müller. 2020. “Neurons Differentiate Magnitude and Location of Mechanical Stimuli.” *Proceedings of the National Academy of Sciences* 117 (2): 848–56. https://doi.org/10.1073/pnas.1909933117.

Greenwood, J, PJ Luthert, OE Pratt, and PL Lantos. 1988. “Hyperosmolar Opening of the Blood-Brain Barrier in the Energy-Depleted Rat Brain. Part 1. Permeability Studies.” *Journal of Cerebral Blood Flow & Metabolism* 8 (1): 9–15.

Gulick, Daniel W., Tao Li, Jeffrey A. Kleim, and Bruce C. Towe. 2017. “Comparison of Electrical and Ultrasound Neurostimulation in Rat Motor Cortex.” *Ultrasound in Medicine & Biology* 43 (12): 2824–33. https://doi.org/10.1016/j.ultrasmedbio.2017.08.937.

Guo, Hongsun, Mark Hamilton, Sarah J. Offutt, Cory D. Gloeckner, Tianqi Li, Yohan Kim, Wynn Legon, Jamu K. Alford, and Hubert H. Lim. 2018. “Ultrasound Produces Extensive Brain Activation via a Cochlear Pathway.” *Neuron* 98 (5): 1020-1030.e4. https://doi.org/10.1016/j.neuron.2018.04.036.

Haacke, E. Mark, Yingbiao Xu, Yu-Chung N. Cheng, and Jürgen R. Reichenbach. 2004. “Susceptibility Weighted Imaging (SWI).” *Magnetic Resonance in Medicine* 52 (3): 612–18. https://doi.org/10.1002/mrm.20198.

Haar, Gail ter. 2009. “Safety and Bio-Effects of Ultrasound Contrast Agents.” *Medical & Biological Engineering & Computing* 47 (8): 893–900. https://doi.org/10.1007/s11517-009-0507-3.

Hajnal, Joseph V, David J Bryant, Larry Kasuboski, Pradip M Pattany, Beatrice De Coene, Paul D Lewis, Jacqueline M Pennock, et al. 1992. “Use of Fluid Attenuated Inversion Recovery (FLAIR) Pulse Sequences in MRI of the Brain.” *Journal of Computer Assisted Tomography* 16: 841–841.

Hameroff, Stuart, Michael Trakas, Chris Duffield, Emil Annabi, M. Bagambhrini Gerace, Patrick Boyle, Anthony Lucas, Quinlan Amos, Annemarie Buadu, and John J. Badal. 2013. “Transcranial Ultrasound (TUS) Effects on Mental States: A Pilot Study.” *Brain Stimulation* 6 (3): 409–15. https://doi.org/10.1016/j.brs.2012.05.002.

Han, Sungmin, Minkyung Kim, Hyungmin Kim, Hyunjoon Shin, and Inchan Youn. 2018. “Ketamine Inhibits Ultrasound Stimulation-Induced Neuromodulation by Blocking Cortical Neuron Activity.”

Ultrasound in Medicine & Biology 44 (3): 635–46. https://doi.org/10.1016/j.ultrasmedbio.2017.11.008.

Harnof, Sagi, Zion Zibly, Lilach Shay, Osnat Dogadkin, Arik Hanannel, Yael Inbar, Itay Goor-Aryeh, and Israel Caspi. 2014. "Magnetic Resonance-Guided Focused Ultrasound Treatment of Facet Joint Pain: Summary of Preclinical Phase." *Journal of Therapeutic Ultrasound* 2 (1): 1–10. https://doi.org/10.1186/2050-5736-2-9.

Hindley, Jonathan, Wladyslaw M. Gedroyc, Lesley Regan, Elizabeth Stewart, Clare Tempany, Kullervo Hynnen, Nathan Macdanold, et al. 2004. "**MRI Guidance of Focused Ultrasound Therapy of Uterine Fibroids:** Early Results." *American Journal of Roentgenology* 183 (6): 1713–19. https://doi.org/10.2214/ajr.183.6.01831713.

Ho, Mai-Lan, Rafael Rojas, and Ronald L. Eisenberg. 2012. "Cerebral Edema." *American Journal of Roentgenology* 199 (3): W258–73. https://doi.org/10.2214/AJR.11.8081.

Holland, Christy K., and Robert E. Apfel. 1990. "Thresholds for Transient Cavitation Produced by Pulsed Ultrasound in a Controlled Nuclei Environment." *The Journal of the Acoustical Society of America* 88 (5): 2059–69. https://doi.org/10.1121/1.400102.

Hynynen, Kullervo, Nathan McDannold, Natalia Vykhodtseva, and Ferenc A. Jolesz. 2001. "Noninvasive MR Imaging–Guided Focal Opening of the Blood-Brain Barrier in Rabbits." *Radiology* 220 (3): 640–46. https://doi.org/10.1148/radiol.2202001804.

Idbaih, Ahmed, Michael Canney, Lisa Belin, Carole Desseaux, Alexandre Vignot, Guillaume Bouchoux, Nicolas Asquier, et al. 2019. "Safety and Feasibility of Repeated and Transient Blood–Brain Barrier Disruption by Pulsed Ultrasound in Patients with Recurrent Glioblastoma." *Clinical Cancer Research* 25 (13): 3793–3801. https://doi.org/10.1158/1078-0432.CCR-18-3643.

Ilovitsh, Tali, Asaf Ilovitsh, Josquin Foiret, Charles F. Caskey, Jiro Kusunose, Brett Z. Fite, Hua Zhang, et al. 2018. "Enhanced Microbubble Contrast Agent Oscillation Following 250 KHz Insonation." *Scientific Reports* 8 (November). https://doi.org/10.1038/s41598-018-34494-5.

Jensen, Jo/rgen Arendt. 1991. "A Model for the Propagation and Scattering of Ultrasound in Tissue." *The Journal of the Acoustical Society of America* 89 (1): 182–90. https://doi.org/10.1121/1.400497.

Jiménez-Gambín, Sergio, Noé Jiménez, José María Benlloch, and Francisco Camarena. 2019. "Holograms to Focus Arbitrary Ultrasonic Fields through the Skull." *Physical Review Applied* 12 (1): 014016. https://doi.org/10.1103/PhysRevApplied.12.014016.

Jones, Rebecca M., Charles F. Caskey, Paul A. Dayton, Ömer Oralkan, and Gianmarco F. Pinton. 2022. "Transcranial Neuromodulation Array With Imaging Aperture for Simultaneous Multifocus Stimulation in Nonhuman Primates." *IEEE Transactions on Ultrasonics, Ferroelectrics, and Frequency Control* 69 (1): 261–72. https://doi.org/10.1109/TUFFC.2021.3108448.

Jones, Ryan M., Lulu Deng, Kogee Leung, Dallan McMahon, Meaghan A. O'Reilly, and Kullervo Hynynen. 2018. "Three-Dimensional Transcranial Microbubble Imaging for Guiding Volumetric Ultrasound-Mediated Blood-Brain Barrier Opening." *Theranostics* 8 (11): 2909–26. https://doi.org/10.7150/thno.24911.

Jones, Ryan M, and Kullervo Hynynen. 2016. "Comparison of Analytical and Numerical Approaches for CT-Based Aberration Correction in Transcranial Passive Acoustic Imaging." *Physics in Medicine and Biology* 61 (1): 23–36. https://doi.org/10.1088/0031-9155/61/1/23.

Jones, Ryan M, Meaghan A O'Reilly, and Kullervo Hynynen. 2013. "Transcranial Passive Acoustic Mapping with Hemispherical Sparse Arrays Using CT-Based Skull-Specific Aberration Corrections: A Simulation Study." *Physics in Medicine and Biology* 58 (14): 4981–5005. https://doi.org/10.1088/0031-9155/58/14/4981.

Jung, Benjamin, Paul A. Taylor, Jakob Seidlitz, Caleb Sponheim, Pierce Perkins, Leslie G. Ungerleider, Daniel Glen, and Adam Messinger. 2021. "A Comprehensive Macaque FMRI Pipeline and

Hierarchical Atlas." *NeuroImage* 235 (July): 117997. https://doi.org/10.1016/j.neuroimage.2021.117997.

Kamimura, Hermes A. S., Shutao Wang, Hong Chen, Qi Wang, Christian Aurup, Camilo Acosta, Antonio A. O. Carneiro, and Elisa E. Konofagou. 2016. "Focused Ultrasound Neuromodulation of Cortical and Subcortical Brain Structures Using 1.9 MHz." *Medical Physics* 43 (10): 5730–35. https://doi.org/10.1118/1.4963208.

Kamimura, Hermes AS, Julien Flament, Julien Valette, Andrea Cafarelli, Romina Aron Badin, Philippe Hantraye, and Benoît Larrat. 2019. "Feedback Control of Microbubble Cavitation for Ultrasound-Mediated Blood–Brain Barrier Disruption in Non-Human Primates under Magnetic Resonance Guidance." *Journal of Cerebral Blood Flow & Metabolism* 39 (7): 1191–1203. https://doi.org/10.1177/0271678X17753514.

Karakatsani, Maria Eleni Marilena, Gesthimani Mania Samiotaki, Matthew E. Downs, Vincent P. Ferrera, and Elisa E. Konofagou. 2017. "Targeting Effects on the Volume of the Focused Ultrasound-Induced Blood–Brain Barrier Opening in Nonhuman Primates In Vivo." *IEEE Transactions on Ultrasonics, Ferroelectrics, and Frequency Control* 64 (5): 798–810. https://doi.org/10.1109/TUFFC.2017.2681695.

Karakatsani, Maria Eleni, Antonios N. Pouliopoulos, Michael Liu, Sachin R. Jambawalikar, and Elisa E. Konofagou. 2021. "Contrast-Free Detection of Focused Ultrasound-Induced Blood-Brain Barrier Opening Using Diffusion Tensor Imaging." *IEEE Transactions on Biomedical Engineering* 68 (8): 2499–2508. https://doi.org/10.1109/TBME.2020.3047575.

Kim, Hyungmin, Alan Chiu, Stephanie D. Lee, Krisztina Fischer, and Seung-Schik Yoo. 2014. "Focused Ultrasound-Mediated Non-Invasive Brain Stimulation: Examination of Sonication Parameters." *Brain Stimulation* 7 (5): 748–56. https://doi.org/10.1016/j.brs.2014.06.011.

Kim, Hyungmin, Alan Chiu, Shinsuk Park, and Seung-Schik Yoo. 2012. "Image-Guided Navigation of Single-Element Focused Ultrasound Transducer." *International Journal of Imaging Systems and Technology* 22 (3): 177–84. https://doi.org/10.1002/ima.22020.

Kim, Y., A. D. Maxwell, T. L. Hall, Z. Xu, K. Lin, and C. A. Cain. 2014. "Rapid Prototyping Fabrication of Focused Ultrasound Transducers." *IEEE Transactions on Ultrasonics, Ferroelectrics, and Frequency Control* 61 (9): 1559–74. https://doi.org/10.1109/TUFFC.2014.3070.

King, Randy L., Julian R. Brown, William T. Newsome, and Kim Butts Pauly. 2013. "Effective Parameters for Ultrasound-Induced In Vivo Neurostimulation." *Ultrasound in Medicine & Biology* 39 (2): 312–31. https://doi.org/10.1016/j.ultrasmedbio.2012.09.009.

Kinoshita, Manabu, Nathan McDannold, Ferenc A. Jolesz, and Kullervo Hynynen. 2006. "Targeted Delivery of Antibodies through the Blood–Brain Barrier by MRI-Guided Focused Ultrasound." *Biochemical and Biophysical Research Communications* 340 (4): 1085–90. https://doi.org/10.1016/j.bbrc.2005.12.112.

Krasovitski, Boris, Victor Frenkel, Shy Shoham, and Eitan Kimmel. 2011. "Intramembrane Cavitation as a Unifying Mechanism for Ultrasound-Induced Bioeffects." *Proceedings of the National Academy of Sciences* 108 (8): 3258–63. https://doi.org/10.1073/pnas.1015771108.

Krishna, Vibhor, Francesco Sammartino, Punit Agrawal, Barbara K Changizi, Eric Bourekas, Michael V Knopp, and Ali Rezai. 2019. "Prospective Tractography-Based Targeting for Improved Safety of Focused Ultrasound Thalamotomy." *Neurosurgery* 84 (1): 160–68.

Kubanek, Jan, Jingyi Shi, Jon Marsh, Di Chen, Cheri Deng, and Jianmin Cui. 2016. "Ultrasound Modulates Ion Channel Currents." *Scientific Reports* 6 (April): 24170. https://doi.org/10.1038/srep24170.

Kubanek, Jan, Poojan Shukla, Alakananda Das, Stephen A. Baccus, and Miriam B. Goodman. 2018. "Ultrasound Elicits Behavioral Responses through Mechanical Effects on Neurons and Ion Channels in a Simple Nervous System." *Journal of Neuroscience* 38 (12): 3081–91. https://doi.org/10.1523/JNEUROSCI.1458-17.2018.

Kusunose, Jiro, William Rodriguez, Huiwen Luo, Thomas Manuel, M. Anthony Phipps, William Grissom, Peter E. Konrad, Benoit M. Dawant, and Charles Caskey. 2021. “Patient-Specific Stereotactic Frame for Transcranial Ultrasound Therapy.” In *2021 IEEE International Ultrasonics Symposium (IUS)*, 1–4. https://doi.org/10.1109/IUS52206.2021.9593641.

Ladabaum, I., Xuecheng Jin, H.T. Soh, A. Atalar, and B.t. Khuri-Yakub. 1998. “Surface Micromachined Capacitive Ultrasonic Transducers.” *IEEE Transactions on Ultrasonics, Ferroelectrics, and Frequency Control* 45 (3): 678–90. https://doi.org/10.1109/58.677612.

Lajoie, Jason M, and Eric V Shusta. 2015. “Targeting Receptor-Mediated Transport for Delivery of Biologics across the Blood-Brain Barrier.” *Annual Review of Pharmacology and Toxicology* 55: 613–31.

Lee, Jungpyo, Kyungmin Ko, Hyogeun Shin, Soo-Jin Oh, C. Justin Lee, Namsun Chou, Nakwon Choi, et al. 2019. “A MEMS Ultrasound Stimulation System for Modulation of Neural Circuits with High Spatial Resolution in Vitro.” *Microsystems & Nanoengineering* 5 (1): 28. https://doi.org/10.1038/s41378-019-0070-5.

Lee, Wonhye, Phillip Croce, Ryan W. Margolin, Amanda Cammalleri, Kyungho Yoon, and Seung-Schik Yoo. 2018. “Transcranial Focused Ultrasound Stimulation of Motor Cortical Areas in Freely-Moving Awake Rats.” *BMC Neuroscience* 19 (1): 57. https://doi.org/10.1186/s12868-018-0459-3.

Lee, Wonhye, Hyungmin Kim, Yujin Jung, In-Uk Song, Yong An Chung, and Seung-Schik Yoo. 2015. “Image-Guided Transcranial Focused Ultrasound Stimulates Human Primary Somatosensory Cortex.” *Scientific Reports* 5 (March): 8743. https://doi.org/10.1038/srep08743.

Lee, Wonhye, Hyungmin Kim, Sungon Lee, Seung-Schik Yoo, and Yong An Chung. 2014. “Creation of Various Skin Sensations Using Pulsed Focused Ultrasound: Evidence for Functional Neuromodulation.” *International Journal of Imaging Systems and Technology* 24 (2): 167–74. https://doi.org/10.1002/ima.22091.

Lee, Wonhye, Stephanie D. Lee, Michael Y. Park, Lori Foley, Erin Purcell-Estabrook, Hyungmin Kim, Krisztina Fischer, Lee-So Maeng, and Seung-Schik Yoo. 2016. “Image-Guided Focused Ultrasound-Mediated Regional Brain Stimulation in Sheep.” *Ultrasound in Medicine & Biology* 42 (2): 459–70. https://doi.org/10.1016/j.ultrasmedbio.2015.10.001.

Legon, Wynn, Leo Ai, Priya Bansal, and Jerel K. Mueller. 2018. “Neuromodulation with Single-Element Transcranial Focused Ultrasound in Human Thalamus.” *Human Brain Mapping* 39 (5): 1995–2006. https://doi.org/10.1002/hbm.23981.

Legon, Wynn, Priya Bansal, Roman Tyshynsky, Leo Ai, and Jerel K. Mueller. 2018. “Transcranial Focused Ultrasound Neuromodulation of the Human Primary Motor Cortex.” *Scientific Reports* 8 (1): 10007. https://doi.org/10.1038/s41598-018-28320-1.

Legon, Wynn, Abby Rowlands, Alexander Opitz, Tomokazu F. Sato, and William J. Tyler. 2012. “Pulsed Ultrasound Differentially Stimulates Somatosensory Circuits in Humans as Indicated by EEG and FMRI.” *PLOS ONE* 7 (12): e51177. https://doi.org/10.1371/journal.pone.0051177.

Legon, Wynn, Tomokazu F. Sato, Alexander Opitz, Jerel Mueller, Aaron Barbour, Amanda Williams, and William J. Tyler. 2014. “Transcranial Focused Ultrasound Modulates the Activity of Primary Somatosensory Cortex in Humans.” *Nature Neuroscience* 17 (2): 322–29. https://doi.org/10.1038/nn.3620.

Leighton, T. 2012. *The Acoustic Bubble*. Academic Press.

Leung, Steven A., David Moore, Taylor D. Webb, John Snell, Pejman Ghanouni, and Kim Butts Pauly. 2021. “Transcranial Focused Ultrasound Phase Correction Using the Hybrid Angular Spectrum Method.” *Scientific Reports* 11 (1): 6532. https://doi.org/10.1038/s41598-021-85535-5.

Leung, Steven A., Taylor D. Webb, Rachelle R. Bitton, Pejman Ghanouni, and Kim Butts Pauly. 2019. “A Rapid Beam Simulation Framework for Transcranial Focused Ultrasound.” *Scientific Reports* 9 (1): 1–11. https://doi.org/10.1038/s41598-019-43775-6.

Li, Guo-Feng, Hui-Xia Zhao, Hui Zhou, Fei Yan, Jing-Yao Wang, Chang-Xi Xu, Cong-Zhi Wang, et al. 2016. "Improved Anatomical Specificity of Non-Invasive Neuro-Stimulation by High Frequency (5 MHz) Ultrasound." *Scientific Reports* 6 (1): 24738. https://doi.org/10.1038/srep24738.

Li, Hongyi, John E. Heath, James S. Trippett, Mikhail G. Shapiro, and Jerzy O. Szablowski. 2021. "Engineering Viral Vectors for Acoustically Targeted Gene Delivery." Preprint. Bioengineering. https://doi.org/10.1101/2021.07.26.453904.

Liberman, Boaz, David Gianfelice, Yael Inbar, Alexander Beck, Tatiana Rabin, Noga Shabshin, Gupta Chander, et al. 2009. "Pain Palliation in Patients with Bone Metastases Using MR-Guided Focused Ultrasound Surgery: A Multicenter Study." *Annals of Surgical Oncology* 16 (1): 140–46. https://doi.org/10.1245/s10434-008-0011-2.

Lin, Chung-Yin, Han-Yi Hsieh, Chiung-Mei Chen, Shang-Rung Wu, Chih-Hung Tsai, Chiung-Yin Huang, Mu-Yi Hua, Kuo-Chen Wei, Chih-Kuang Yeh, and Hao-Li Liu. 2016. "Non-Invasive, Neuron-Specific Gene Therapy by Focused Ultrasound-Induced Blood-Brain Barrier Opening in Parkinson's Disease Mouse Model." *Journal of Controlled Release* 235 (August): 72–81. https://doi.org/10.1016/j.jconrel.2016.05.052.

Lin, Zhengrong, Wei Zhou, Xiaowei Huang, Kaiyue Wang, Jie Tang, Lili Niu, Long Meng, and Hairong Zheng. 2018. "On-Chip Ultrasound Modulation of Pyramidal Neuronal Activity in Hippocampal Slices." *Advanced Biosystems* 2 (8): 1800041. https://doi.org/10.1002/adbi.201800041.

Lipsman, Nir, Ying Meng, Allison J. Bethune, Yuexi Huang, Benjamin Lam, Mario Masellis, Nathan Herrmann, et al. 2018. "Blood–Brain Barrier Opening in Alzheimer's Disease Using MR-Guided Focused Ultrasound." *Nature Communications* 9 (1): 2336. https://doi.org/10.1038/s41467-018-04529-6.

Lipsman, Nir, Michael L Schwartz, Yuexi Huang, Liesly Lee, Tejas Sankar, Martin Chapman, Kullervo Hynynen, and Andres M Lozano. 2013. "MR-Guided Focused Ultrasound Thalamotomy for Essential Tremor: A Proof-of-Concept Study." *The Lancet Neurology* 12 (5): 462–68. https://doi.org/10.1016/S1474-4422(13)70048-6.

Liu, Hao-Li, Heng-Wen Chen, Zhen-Hao Kuo, and Wen-Cheng Huang. 2008. "Design and Experimental Evaluations of a Low-Frequency Hemispherical Ultrasound Phased-Array System for Transcranial Blood–Brain Barrier Disruption." *IEEE Transactions on Biomedical Engineering* 55 (10): 2407–16. https://doi.org/10.1109/TBME.2008.925697.

Liu, Hao-Li, Chen-Kai Jan, Po-Chun Chu, Jhong-Cing Hong, Pei-Yun Lee, Jyh-Duen Hsu, Chung-Chih Lin, Chiung-Ying Huang, Pin-Yuan Chen, and Kuo-Chen Wei. 2014. "Design and Experimental Evaluation of a 256-Channel Dual-Frequency Ultrasound Phased-Array System for Transcranial Blood–Brain Barrier Opening and Brain Drug Delivery." *IEEE Transactions on Biomedical Engineering* 61 (4): 1350–60. https://doi.org/10.1109/TBME.2014.2305723.

Madersbacher, Stephan, Markus Pedevilla, Lorri Vingers, Martin Susani, and Michael Marberger. 1995. "Effect of High-Intensity Focused Ultrasound on Human Prostate Cancer in Vivo." *Cancer Research* 55 (15): 3346–51.

Maimbourg, Guillaume, Alexandre Houdouin, Thomas Deffieux, Mickaël Tanter, and Jean-François Aubry. 2018. "3D-Printed Adaptive Acoustic Lens as a Disruptive Technology for Transcranial Ultrasound Therapy Using Single-Element Transducers." *Physics in Medicine and Biology* 63 (2): 025026. https://doi.org/10.1088/1361-6560/aaa037.

Mainprize, Todd, Nir Lipsman, Yuexi Huang, Ying Meng, Allison Bethune, Sarah Ironside, Chinthaka Heyn, et al. 2019. "Blood-Brain Barrier Opening in Primary Brain Tumors with Non-Invasive MR-Guided Focused Ultrasound: A Clinical Safety and Feasibility Study." *Scientific Reports* 9 (1): 1–7.

Manuel, Thomas J., Jiro Kusunose, Xiaoyan Zhan, Xiaohui Lv, Ellison Kang, Aaron Yang, Zixiu Xiang, and Charles F. Caskey. 2020. "Ultrasound Neuromodulation Depends on Pulse Repetition Frequency

and Can Modulate Inhibitory Effects of TTX." *Scientific Reports* 10 (1): 15347. https://doi.org/10.1038/s41598-020-72189-y.

Manuel, Thomas, M. Anthony Phipps, and Charles Caskey. 2022. "Design of a Therapeutic Ultrasound Array for Small Volume Blood-Brain Barrier Opening in Macaques." TechRxiv. https://doi.org/10.36227/techrxiv.20427975.v1.

Marquet, Fabrice, Tobias Teichert, Shih-Ying Wu, Yao-Sheng Tung, Matthew Downs, Shutao Wang, Cherry Chen, Vincent Ferrera, and Elisa E. Konofagou. 2014. "Real-Time, Transcranial Monitoring of Safe Blood-Brain Barrier Opening in Non-Human Primates." Edited by Stefan Liebner. *PLoS ONE* 9 (2): e84310. https://doi.org/10.1371/journal.pone.0084310.

Marquet, Fabrice, Yao-Sheng Tung, Tobias Teichert, Vincent P. Ferrera, and Elisa E. Konofagou. 2011. "Noninvasive, Transient and Selective Blood-Brain Barrier Opening in Non-Human Primates In Vivo." Edited by Martin W. Brechbiel. *PLoS ONE* 6 (7): e22598. https://doi.org/10.1371/journal.pone.0022598.

Marsac, L., D. Chauvet, B. Larrat, M. Pernot, B. Robert, M. Fink, A. L. Boch, J. F. Aubry, and M. Tanter. 2012. "MR-Guided Adaptive Focusing of Therapeutic Ultrasound Beams in the Human Head." *Medical Physics* 39 (2): 1141–49. https://doi.org/10.1118/1.3678988.

Martin, Eleanor, Jiri Jaros, and Bradley E. Treeby. 2020. "Experimental Validation of K-Wave: Nonlinear Wave Propagation in Layered, Absorbing Fluid Media." *IEEE Transactions on Ultrasonics, Ferroelectrics, and Frequency Control* 67 (1): 81–91. https://doi.org/10.1109/TUFFC.2019.2941795.

Martin, Eleanor, Morgan Roberts, and Bradley Treeby. 2021. "Measurement and Simulation of Steered Acoustic Fields Generated by a Multielement Array for Therapeutic Ultrasound." *JASA Express Letters* 1 (1): 012001. https://doi.org/10.1121/10.0003210.

Marty, Benjamin, Benoit Larrat, Maxime Van Landeghem, Caroline Robic, Philippe Robert, Marc Port, Denis Le Bihan, et al. 2012. "Dynamic Study of Blood–Brain Barrier Closure after Its Disruption Using Ultrasound: A Quantitative Analysis." *Journal of Cerebral Blood Flow & Metabolism* 32 (10): 1948–58. https://doi.org/10.1038/jcbfm.2012.100.

McDannold, N., C. D. Arvanitis, N. Vykhodtseva, and M. S. Livingstone. 2012. "Temporary Disruption of the Blood-Brain Barrier by Use of Ultrasound and Microbubbles: Safety and Efficacy Evaluation in Rhesus Macaques." *Cancer Research* 72 (14): 3652–63. https://doi.org/10.1158/0008-5472.CAN-12-0128.

McDannold, N, N Vykhodtseva, and K Hynynen. 2006. "Targeted Disruption of the Blood–Brain Barrier with Focused Ultrasound: Association with Cavitation Activity." *Physics in Medicine and Biology* 51 (4): 793–807. https://doi.org/10.1088/0031-9155/51/4/003.

McDannold, Nathan, and Stephan E. Maier. 2008. "Magnetic Resonance Acoustic Radiation Force Imaging." *Medical Physics* 35 (8): 3748–58. https://doi.org/10.1118/1.2956712.

McDannold, Nathan, Natalia Vykhodtseva, and Kullervo Hynynen. 2008a. "Blood-Brain Barrier Disruption Induced by Focused Ultrasound and Circulating Preformed Microbubbles Appears to Be Characterized by the Mechanical Index." *Ultrasound in Medicine & Biology* 34 (5): 834–40. https://doi.org/10.1016/j.ultrasmedbio.2007.10.016.

———. 2008b. "Effects of Acoustic Parameters and Ultrasound Contrast Agent Dose on Focused-Ultrasound Induced Blood-Brain Barrier Disruption." *Ultrasound in Medicine & Biology* 34 (6): 930–37. https://doi.org/10.1016/j.ultrasmedbio.2007.11.009.

McMahon, Dallan, Charissa Poon, and Kullervo Hynynen. 2019. "Evaluating the Safety Profile of Focused Ultrasound and Microbubble-Mediated Treatments to Increase Blood-Brain Barrier Permeability." *Expert Opinion on Drug Delivery* 16 (2): 129–42. https://doi.org/10.1080/17425247.2019.1567490.

Menz, Mike D., Patrick Ye, Kamyar Firouzi, Amin Nikoozadeh, Kim Butts Pauly, Pierre Khuri-Yakub, and Stephen A. Baccus. 2019. “Radiation Force as a Physical Mechanism for Ultrasonic Neurostimulation of the Ex Vivo Retina.” *Journal of Neuroscience* 39 (32): 6251–64. https://doi.org/10.1523/JNEUROSCI.2394-18.2019.

Meynier, Cyril, Yalcin Yanamer, Michael Canney, An Nguyen-Dinh, Alexandre Carpentier, and Jean-Yves Chapelon. 2012. “Performance Assessment Of CMUTs in Dual Modality Imaging/HIFU Applications.” In *2012 IEEE International Ultrasonics Symposium*, 81–84. https://doi.org/10.1109/ULTSYM.2012.0020.

Mihran, Richard T., Frank S. Barnes, and Howard Wachtel. 1990. “Temporally-Specific Modification of Myelinated Axon Excitability in Vitro Following a Single Ultrasound Pulse.” *Ultrasound in Medicine & Biology* 16 (3): 297–309. https://doi.org/10.1016/0301-5629(90)90008-Z.

Miller, Greg. 2002. “Breaking down Barriers.” American Association for the Advancement of Science.

Mohammadjavadi, Morteza, Patrick Peiyong Ye, Anping Xia, Julian Brown, Gerald Popelka, and Kim Butts Pauly. 2019. “Elimination of Peripheral Auditory Pathway Activation Does Not Affect Motor Responses from Ultrasound Neuromodulation.” *Brain Stimulation* 12 (4): 901–10. https://doi.org/10.1016/j.brs.2019.03.005.

Monti, Martin M., Caroline Schnakers, Alexander S. Korb, Alexander Bystritsky, and Paul M. Vespa. 2016. “Non-Invasive Ultrasonic Thalamic Stimulation in Disorders of Consciousness after Severe Brain Injury: A First-in-Man Report.” *Brain Stimulation* 9 (6): 940–41. https://doi.org/10.1016/j.brs.2016.07.008.

Morris, Catherine E., and Peter F. Juranka. 2007. “Nav Channel Mechanosensitivity: Activation and Inactivation Accelerate Reversibly with Stretch.” *Biophysical Journal* 93 (3): 822–33. https://doi.org/10.1529/biophysj.106.101246.

Morris, Hugh, Ian Rivens, Adam Shaw, and Gail ter Haar. 2008. “Investigation of the Viscous Heating Artefact Arising from the Use of Thermocouples in a Focused Ultrasound Field.” *Physics in Medicine and Biology* 53 (17): 4759–76. https://doi.org/10.1088/0031-9155/53/17/020.

Morse, Sophie V, Antonios N Pouliopoulos, Tiffany G Chan, Matthew J Copping, Julien Lin, Nicholas J Long, and James J Choi. 2019. “Rapid Short-Pulse Ultrasound Delivers Drugs Uniformly across the Murine Blood-Brain Barrier with Negligible Disruption.” *Radiology* 291 (2): 459.

Mullin, Lee, Ryan Gessner, James Kwan, Mehmet Kaya, Mark Borden, and Paul Dayton. 2011. “Effect of Anesthesia Carrier Gas on in Vivo Circulation Times of Ultrasound Microbubble Contrast Agents in Rats.” *Contrast Media and Molecular Imaging*, no. 6 (January): 126–31. https://doi.org/10.1002/cmmi.414.

Nightingale, Kathy. 2011. “Acoustic Radiation Force Impulse (ARFI) Imaging: A Review.” *Current Medical Imaging Reviews* 7 (4): 328–39. https://doi.org/10.2174/157340511798038657.

Nikolaev, Yury A., Peter J. Dosen, Derek R. Laver, Dirk F. van Helden, and Owen P. Hamill. 2015. “Single Mechanically-Gated Cation Channel Currents Can Trigger Action Potentials in Neocortical and Hippocampal Pyramidal Neurons.” *Brain Research* 1608 (May): 1–13. https://doi.org/10.1016/j.brainres.2015.02.051.

Noroozian, Zeinab, Kristiana Xhima, Yuexi Huang, Brian K. Kaspar, Sebastian Kügler, Kullervo Hynynen, and Isabelle Aubert. 2019. “MRI-Guided Focused Ultrasound for Targeted Delivery of RAAV to the Brain.” *Methods in Molecular Biology (Clifton, N.J.)* 1950: 177–97. https://doi.org/10.1007/978-1-4939-9139-6_10.

Novell, A., H. a. S. Kamimura, A. Cafarelli, M. Gerstenmayer, J. Flament, J. Valette, P. Agou, et al. 2020. “A New Safety Index Based on Intrapulse Monitoring of Ultra-Harmonic Cavitation during Ultrasound-Induced Blood-Brain Barrier Opening Procedures.” *Scientific Reports* 10 (1): 10088. https://doi.org/10.1038/s41598-020-66994-8.

Nyborg, Wesley L. 1981. “Heat Generation by Ultrasound in a Relaxing Medium.” *The Journal of the Acoustical Society of America* 70 (2): 310–12. https://doi.org/10.1121/1.386778.

O’Brien, William D. 2007. “Ultrasound–Biophysics Mechanisms.” *Progress in Biophysics and Molecular Biology*, Effects of ultrasound and infrasound relevant to human health, 93 (1): 212–55. https://doi.org/10.1016/j.pbiomolbio.2006.07.010.

Odéen, Henrik, Joshua de Bever, Scott Almquist, Alexis Farrer, Nick Todd, Allison Payne, John W. Snell, Douglas A. Christensen, and Dennis L. Parker. 2014. “Treatment Envelope Evaluation in Transcranial Magnetic Resonance-Guided Focused Ultrasound Utilizing 3D MR Thermometry.” *Journal of Therapeutic Ultrasound* 2 (1): 19. https://doi.org/10.1186/2050-5736-2-19.

Ogawa, Seiji, Tso-Ming Lee, Alan R Kay, and David W Tank. 1990. “Brain Magnetic Resonance Imaging with Contrast Dependent on Blood Oxygenation.” *Proceedings of the National Academy of Sciences* 87 (24): 9868–72.

Ohl, Siew-Wan, Evert Klaseboer, and Boo Cheong Khoo. 2015. “Bubbles with Shock Waves and Ultrasound: A Review.” *Interface Focus* 5 (5): 20150019. https://doi.org/10.1098/rsfs.2015.0019.

Ohta, Seiichi, Emi Kikuchi, Ayumu Ishijima, Takashi Azuma, Ichiro Sakuma, and Taichi Ito. 2020. “Investigating the Optimum Size of Nanoparticles for Their Delivery into the Brain Assisted by Focused Ultrasound-Induced Blood–Brain Barrier Opening.” *Scientific Reports* 10 (1): 18220. https://doi.org/10.1038/s41598-020-75253-9.

O’Reilly, Meaghan A, Yuexi Huang, and Kullervo Hynynen. 2010. “The Impact of Standing Wave Effects on Transcranial Focused Ultrasound Disruption of the Blood–Brain Barrier in a Rat Model.” *Physics in Medicine and Biology* 55 (18): 5251–67. https://doi.org/10.1088/0031-9155/55/18/001.

O’Reilly, Meaghan A., and Kullervo Hynynen. 2010. “A PVDF Receiver for Ultrasound Monitoring of Transcranial Focused Ultrasound Therapy.” *IEEE Transactions on Biomedical Engineering* 57 (9): 2286–94. https://doi.org/10.1109/TBME.2010.2050483.

———. 2012. “Blood-Brain Barrier: Real-Time Feedback-Controlled Focused Ultrasound Disruption by Using an Acoustic Emissions–Based Controller.” *Radiology* 263 (1): 96–106. https://doi.org/10.1148/radiol.11111417.

Otsu, Nobuyuki. n.d. “A Tlreshold Selection Method from Gray-Level Histograms,” 5.

Pacia, Christopher P., Jinyun Yuan, Yimei Yue, Lu Xu, Arash Nazeri, Rupen Desai, H. Michael Gach, et al. 2022. “Sonobiopsy for Minimally Invasive, Spatiotemporally-Controlled, and Sensitive Detection of Glioblastoma-Derived Circulating Tumor DNA.” *Theranostics* 12 (1): 362–78. https://doi.org/10.7150/thno.65597.

Pardridge, William M. 2005. “The Blood-Brain Barrier: Bottleneck in Brain Drug Development.” *NeuroRx: The Journal of the American Society for Experimental NeuroTherapeutics* 2 (1): 3–14. https://doi.org/10.1602/neurorx.2.1.3.

Pardridge, William M. 2006. “Molecular Trojan Horses for Blood–Brain Barrier Drug Delivery.” *Current Opinion in Pharmacology*, Anti-infectives/New Technologies, 6 (5): 494–500. https://doi.org/10.1016/j.coph.2006.06.001.

———. 2012. “Drug Transport across the Blood–Brain Barrier.” *Journal of Cerebral Blood Flow & Metabolism* 32 (11): 1959–72. https://doi.org/10.1038/jcbfm.2012.126.

Pascal, Aurea, Ningrui Li, Kendra J Lechtenberg, Jarrett Rosenberg, Raag D Airan, Donna M Bouley, and Kim Butts Pauly. 2020. “Histologic Evaluation of Activation of Acute Inflammatory Response in a Mouse Model Following Ultrasound- Mediated Blood-Brain Barrier Using Different Acoustic Pressures and Microbubble Doses” 4: 14.

Patel, Mayur M., Bhoomika R. Goyal, Shraddha V. Bhadada, Jay S. Bhatt, and Avani F. Amin. 2009. “Getting into the Brain.” *CNS Drugs* 23 (1): 35–58. https://doi.org/10.2165/0023210-200923010-00003.

Payne, Allison, Robb Merrill, Emilee Minalga, J Rock Hadley, Henrik Odéen, Lorne W Hofstetter, Sara Johnson, et al. 2020. “A Breast-Specific MR Guided Focused Ultrasound Platform and Treatment Protocol: First-in-Human Technical Evaluation.” *IEEE Transactions on Biomedical Engineering* 68 (3): 893–904.

Payne, Allison, Urvi Vyas, Nick Todd, Joshua de Bever, Douglas A. Christensen, and Dennis L. Parker. 2011. “The Effect of Electronically Steering a Phased Array Ultrasound Transducer on Near-Field Tissue Heating.” *Medical Physics* 38 (9): 4971–81. https://doi.org/10.1118/1.3618729.

Pennes, Harry H. 1945. “Analysis of Tissue and Arterid Blood Temperatwes.” *Ultrasound in Medicine & Biology* 1: 369–76.

Pernot, Mathieu, Jean-François Aubry, Mickaël Tanter, Jean-Louis Thomas, and Mathias Fink. 2003. “High Power Transcranial Beam Steering for Ultrasonic Brain Therapy.” *Physics in Medicine and Biology* 48 (16): 2577–89. https://doi.org/10.1109/TMI.2010.2076829.

Phipps, M. Anthony, Sumeeth V. Jonathan, Pai-Feng Yang, Vandiver Chaplin, Li Min Chen, William A. Grissom, and Charles F. Caskey. 2019. “Considerations for Ultrasound Exposure during Transcranial MR Acoustic Radiation Force Imaging.” *Scientific Reports* 9 (1): 1–11. https://doi.org/10.1038/s41598-019-52443-8.

Pichardo, Samuel, Vivian W Sin, and Kullervo Hynynen. 2011. “Multi-Frequency Characterization of the Speed of Sound and Attenuation Coefficient for Longitudinal Transmission of Freshly Excised Human Skulls.” *Physics in Medicine and Biology* 56 (1): 219–50. https://doi.org/10.1088/0031-9155/56/1/014.

Pierce, Allan D., and Robert T. Beyer. 1990. “*Acoustics: An Introduction to Its Physical Principles and Applications. 1989 Edition*.” *The Journal of the Acoustical Society of America* 87 (4): 1826–27. https://doi.org/10.1121/1.399390.

Pinton, Gianmarco, Jean-Francois Aubry, Emmanuel Bossy, Marie Muller, Mathieu Pernot, and Mickael Tanter. 2012. “Attenuation, Scattering, and Absorption of Ultrasound in the Skull Bone.” *Medical Physics* 39 (1): 299–307. https://doi.org/10.1118/1.3668316.

Plaksin, Michael, Eitan Kimmel, and Shy Shoham. 2016. “Cell-Type-Selective Effects of Intramembrane Cavitation as a Unifying Theoretical Framework for Ultrasonic Neuromodulation.” *ENeuro* 3 (3). https://doi.org/10.1523/ENEURO.0136-15.2016.

Pouliopoulos, Antonios N., Nancy Kwon, Greg Jensen, Anna Meaney, Yusuke Niimi, Mark T. Burgess, Robin Ji, et al. 2021. “Safety Evaluation of a Clinical Focused Ultrasound System for Neuronavigation Guided Blood-Brain Barrier Opening in Non-Human Primates.” *Scientific Reports* 11 (1): 15043. https://doi.org/10.1038/s41598-021-94188-3.

Pouliopoulos, Antonios N., Shih-Ying Wu, Mark T. Burgess, Maria Eleni Karakatsani, Hermes A. S. Kamimura, and Elisa E. Konofagou. 2020. “A Clinical System for Non-Invasive Blood–Brain Barrier Opening Using a Neuronavigation-Guided Single-Element Focused Ultrasound Transducer.” *Ultrasound in Medicine & Biology* 46 (1): 73–89. https://doi.org/10.1016/j.ultrasmedbio.2019.09.010.

Prada, Francesco, Antonio G. Gennari, Ian M. Linville, Michael E. Mutersbaugh, Zhihang Chen, Natasha Sheybani, Francesco DiMeco, Frederic Padilla, and John A. Hossack. 2021. “Quantitative Analysis of In-Vivo Microbubble Distribution in the Human Brain.” *Scientific Reports* 11 (1): 11797. https://doi.org/10.1038/s41598-021-91252-w.

Prieto, Martin Loynaz, Kamyar Firouzi, Butrus T. Khuri-Yakub, and Merritt Maduke. 2018. “Activation of Piezo1 but Not NaV1.2 Channels by Ultrasound at 43 MHz.” *Ultrasound in Medicine & Biology* 44 (6): 1217–32. https://doi.org/10.1016/j.ultrasmedbio.2017.12.020.

Prieto, Martin Loynaz, Ömer Oralkan, Butrus T. Khuri-Yakub, and Merritt C. Maduke. 2013. “Dynamic Response of Model Lipid Membranes to Ultrasonic Radiation Force.” *PLOS ONE* 8 (10): e77115. https://doi.org/10.1371/journal.pone.0077115.

Qin, Shengping, and Katherine W. Ferrara. 2010. “A Model for the Dynamics of Ultrasound Contrast Agents in Vivo.” *The Journal of the Acoustical Society of America* 128 (3): 1511. https://doi.org/10.1121/1.3409476.

Ramaekers, P, M de Greef, R Berriet, C T W Moonen, and M Ries. 2017. “Evaluation of a Novel Therapeutic Focused Ultrasound Transducer Based on Fermat’s Spiral.” *Physics in Medicine and Biology* 62 (12): 5021–45. https://doi.org/10.1088/1361-6560/aa716c.

Rapoport, Stanley I. 2000. “Osmotic Opening of the Blood–Brain Barrier: Principles, Mechanism, and Therapeutic Applications,” 14.

Raspagliesi, Luca, Antonio D’Ammando, Matteo Gionso, Natasha D. Sheybani, Maria-Beatriz Lopes, David Moore, Steven Allen, et al. 2021. “Intracranial Sonodynamic Therapy With 5-Aminolevulinic Acid and Sodium Fluorescein: Safety Study in a Porcine Model.” *Frontiers in Oncology* 11. https://www.frontiersin.org/articles/10.3389/fonc.2021.679989.

Reznik, Samantha J., Joseph L. Sanguinetti, William J. Tyler, Chris Daft, and John J. B. Allen. 2020. “A Double-Blind Pilot Study of Transcranial Ultrasound (TUS) as a Five-Day Intervention: TUS Mitigates Worry among Depressed Participants.” *Neurology, Psychiatry and Brain Research* 37 (September): 60–66. https://doi.org/10.1016/j.npbr.2020.06.004.

Rieke, Viola, and Kim Butts Pauly. 2008. “MR Thermometry.” *Journal of Magnetic Resonance Imaging : JMRI* 27 (2): 376–90. https://doi.org/10.1002/jmri.21265.

Roberts, Jill W., Lauren Powlovich, Natasha Sheybani, and Suzanne LeBlang. 2022. “Focused Ultrasound for the Treatment of Glioblastoma.” *Journal of Neuro-Oncology* 157 (2): 237–47. https://doi.org/10.1007/s11060-022-03974-0.

Roberts, William W., Timothy L. Hall, Kimberly Ives, J. Stuart Wolf, J. Brian Fowlkes, and Charles A. Cain. 2006. “Pulsed Cavitational Ultrasound: A Noninvasive Technology for Controlled Tissue Ablation (Histotripsy) in the Rabbit Kidney.” *Journal of Urology* 175 (2): 734–38. https://doi.org/10.1016/S0022-5347(05)00141-2.

Robertson, James L. B., Ben T. Cox, J. Jaros, and Bradley E. Treeby. 2017. “Accurate Simulation of Transcranial Ultrasound Propagation for Ultrasonic Neuromodulation and Stimulation.” *The Journal of the Acoustical Society of America* 141 (3): 1726–38. https://doi.org/10.1121/1.4976339.

Ryken, Timothy Charles, Nafi Aygun, Johnathan Morris, Marin Schweizer, Rajeshwari Nair, Cassandra Spracklen, Steven N Kalkanis, and Jeffrey J Olson. 2014. “The Role of Imaging in the Management of Progressive Glioblastoma.” *Journal of Neuro-Oncology* 118 (3): 435–60.

Samiotaki, Gesthimani, Camilo Acosta, Shutao Wang, and Elisa E Konofagou. 2015. “Enhanced Delivery and Bioactivity of the Neurturin Neurotrophic Factor through Focused Ultrasound—Mediated Blood—Brain Barrier Opening in Vivo.” *Journal of Cerebral Blood Flow & Metabolism* 35 (4): 611–22. https://doi.org/10.1038/jcbfm.2014.236.

Samiotaki, Gesthimani, Maria Eleni Karakatsani, Amanda Buch, Stephanos Papadopoulos, Shih Ying Wu, Sachin Jambawalikar, and Elisa E. Konofagou. 2017. “Pharmacokinetic Analysis and Drug Delivery Efficiency of the Focused Ultrasound-Induced Blood-Brain Barrier Opening in Non-Human Primates.” *Magnetic Resonance Imaging* 37 (April): 273–81. https://doi.org/10.1016/j.mri.2016.11.023.

Sarvazyan, Armen P., Oleg V. Rudenko, and Wesley L. Nyborg. 2010. “Biomedical Applications of Radiation Force of Ultrasound: Historical Roots and Physical Basis.” *Ultrasound in Medicine & Biology* 36 (9): 1379–94. https://doi.org/10.1016/j.ultrasmedbio.2010.05.015.

Sato, Tomokazu, Mikhail G. Shapiro, and Doris Y. Tsao. 2018. “Ultrasonic Neuromodulation Causes Widespread Cortical Activation via an Indirect Auditory Mechanism.” *Neuron* 98 (5): 1031-1041.e5. https://doi.org/10.1016/j.neuron.2018.05.009.

Schmitz, A. C., D. Gianfelice, B. L. Daniel, W. P. Th M. Mali, and M. a. a. J. van den Bosch. 2008. "Image-Guided Focused Ultrasound Ablation of Breast Cancer: Current Status, Challenges, and Future Directions." *European Radiology* 18 (7): 1431–41. https://doi.org/10.1007/s00330-008-0906-0.

Schneider, Caroline A., Wayne S. Rasband, and Kevin W. Eliceiri. 2012. "NIH Image to ImageJ: 25 Years of Image Analysis." *Nature Methods* 9 (7): 671–75. https://doi.org/10.1038/nmeth.2089.

Selzo, M. R., and C. M. Gallippi. 2013. "Viscoelastic Response (VisR) Imaging for Assessment of Viscoelasticity in Voigt Materials." *IEEE Transactions on Ultrasonics, Ferroelectrics, and Frequency Control* 60 (12): 2488–2500. https://doi.org/10.1109/TUFFC.2013.2848.

Shapiro, Mikhail G., Kazuaki Homma, Sebastian Villarreal, Claus-Peter Richter, and Francisco Bezanilla. 2012. "Infrared Light Excites Cells by Changing Their Electrical Capacitance." *Nature Communications* 3 (1): 1–11. https://doi.org/10.1038/ncomms1742.

Sheikov, Nickolai, Nathan McDannold, Natalia Vykhodtseva, Ferenc Jolesz, and Kullervo Hynynen. 2004. "Cellular Mechanisms of the Blood-Brain Barrier Opening Induced by Ultrasound in Presence of Microbubbles." *Ultrasound in Medicine & Biology* 30 (7): 979–89. https://doi.org/10.1016/j.ultrasmedbio.2004.04.010.

Sigrist, Rosa M.S., Joy Liau, Ahmed El Kaffas, Maria Cristina Chammas, and Juergen K. Willmann. 2017. "Ultrasound Elastography: Review of Techniques and Clinical Applications." *Theranostics* 7 (5): 1303–29. https://doi.org/10.7150/thno.18650.

Singh, Aparna, Jiro Kusunose, M. Anthony Phipps, Feng Wang, Li Min Chen, and Charles F. Caskey. 2022. "Guiding and Monitoring Focused Ultrasound Mediated Blood–Brain Barrier Opening in Rats Using Power Doppler Imaging and Passive Acoustic Mapping." *Scientific Reports* 12 (1): 14758. https://doi.org/10.1038/s41598-022-18328-z.

Smith, Stephen M. 2002. "Fast Robust Automated Brain Extraction." *Human Brain Mapping* 17 (3): 143–55. https://doi.org/10.1002/hbm.10062.

Smith, Wallace Arden, and Bertram A Auld. 1991. "Modeling 1-3 Composite Piezoelectrics: Thickness-Mode Oscillations." *IEEE Transactions on Ultrasonics, Ferroelectrics, and Frequency Control* 38 (1): 40–47.

Song, Kang-Ho, Brandon K. Harvey, and Mark A. Borden. 2018. "State-of-the-Art of Microbubble-Assisted Blood-Brain Barrier Disruption." *Theranostics* 8 (16): 4393–4408. https://doi.org/10.7150/thno.26869.

Stephens, Douglas N., Dustin E. Kruse, Shengping Qin, and Katherine W. Ferrara. 2011. "Design Aspects of Focal Beams from High-Intensity Arrays." *IEEE Transactions on Ultrasonics, Ferroelectrics, and Frequency Control* 58 (8): 1590–1602. https://doi.org/10.1109/TUFFC.2011.1986.

Sun, Jie, and Kullervo Hynynen. 1998. "Focusing of Therapeutic Ultrasound through a Human Skull: A Numerical Study." *The Journal of the Acoustical Society of America* 104 (3): 1705–15. https://doi.org/10.1121/1.424383.

Sun, Tao, Yongzhi Zhang, Chanikarn Power, Phillip M. Alexander, Jonathan T. Sutton, Muna Aryal, Natalia Vykhodtseva, Eric L. Miller, and Nathan J. McDannold. 2017. "Closed-Loop Control of Targeted Ultrasound Drug Delivery across the Blood–Brain/Tumor Barriers in a Rat Glioma Model." *Proceedings of the National Academy of Sciences* 114 (48). https://doi.org/10.1073/pnas.1713328114.

Sweeney, Melanie D., Zhen Zhao, Axel Montagne, Amy R. Nelson, and Berislav V. Zlokovic. 2019. "Blood-Brain Barrier: From Physiology to Disease and Back." *Physiological Reviews* 99 (1): 21–78. https://doi.org/10.1152/physrev.00050.2017.

Szablowski, Jerzy O., Audrey Lee-Gosselin, Brian Lue, Dina Malounda, and Mikhail G. Shapiro. 2018. "Acoustically Targeted Chemogenetics for the Non-Invasive Control of Neural Circuits." *Nature Biomedical Engineering* 2 (7): 475–84. https://doi.org/10.1038/s41551-018-0258-2.

Szabo, Thomas L. 2004. *Diagnostic Ultrasound Imaging: Inside Out*. Academic Press.

———. 2022. “Acoustic Radiation Forces at the Crossroads of Ultrasound Exposimetry, HIFU and Elastography.” *IEEE Transactions on Ultrasonics, Ferroelectrics, and Frequency Control*, 1–1. https://doi.org/10.1109/TUFFC.2022.3213021.

Tang, Sai Chun, and Gregory T. Clement. 2010. “Standing-Wave Suppression for Transcranial Ultrasound by Random Modulation.” *IEEE Transactions on Bio-Medical Engineering* 57 (1): 203–5. https://doi.org/10.1109/TBME.2009.2028653.

Terranova, Carmen, Vincenzo Rizzo, Alberto Cacciola, Gaetana Chillemi, Alessandro Calamuneri, Demetrio Milardi, and Angelo Quartarone. 2019. “Is There a Future for Non-Invasive Brain Stimulation as a Therapeutic Tool?” *Frontiers in Neurology* 9. https://www.frontiersin.org/articles/10.3389/fneur.2018.01146.

Thévenot, Emmanuel, Jessica F. Jordão, Meaghan A. O’Reilly, Kelly Markham, Ying-Qi Weng, Kevin D. Foust, Brian K. Kaspar, Kullervo Hynynen, and Isabelle Aubert. 2012. “Targeted Delivery of Self-Complementary Adeno-Associated Virus Serotype 9 to the Brain, Using Magnetic Resonance Imaging-Guided Focused Ultrasound.” *Human Gene Therapy* 23 (11): 1144–55. https://doi.org/10.1089/hum.2012.013.

Tran, B.C., Jongbum Seo, T.L. Hall, J.B. Fowlkes, and C.A. Cain. 2003. “Microbubble-Enhanced Cavitation for Noninvasive Ultrasound Surgery.” *IEEE Transactions on Ultrasonics, Ferroelectrics, and Frequency Control* 50 (10): 1296–1304. https://doi.org/10.1109/TUFFC.2003.1244746.

Treat, Lisa H., Nathan McDannold, Yongzhi Zhang, Natalia Vykhodtseva, and Kullervo Hynynen. 2012. “Improved Anti-Tumor Effect of Liposomal Doxorubicin After Targeted Blood-Brain Barrier Disruption by MRI-Guided Focused Ultrasound in Rat Glioma.” *Ultrasound in Medicine & Biology* 38 (10): 1716–25. https://doi.org/10.1016/j.ultrasmedbio.2012.04.015.

Treeby, Bradley E., and Benjamin T. Cox. 2010. “K-Wave: MATLAB Toolbox for the Simulation and Reconstruction of Photoacoustic Wave Fields.” *Journal of Biomedical Optics* 15 (2): 021314. https://doi.org/10.1117/1.3360308.

Tufail, Yusuf, Alexei Matyushov, Nathan Baldwin, Monica L. Tauchmann, Joseph Georges, Anna Yoshihiro, Stephen I. Helms Tillery, and William J. Tyler. 2010. “Transcranial Pulsed Ultrasound Stimulates Intact Brain Circuits.” *Neuron* 66 (5): 681–94. https://doi.org/10.1016/j.neuron.2010.05.008.

Tufail, Yusuf, Anna Yoshihiro, Sandipan Pati, Monica M. Li, and William J. Tyler. 2011. “Ultrasonic Neuromodulation by Brain Stimulation with Transcranial Ultrasound.” *Nature Protocols* 6 (9): 1453–70. https://doi.org/10.1038/nprot.2011.371.

Tung, Yao-Sheng, Fotios Vlachos, Jameel A. Feshitan, Mark A. Borden, and Elisa E. Konofagou. 2011. “The Mechanism of Interaction between Focused Ultrasound and Microbubbles in Blood-Brain Barrier Opening in Mice.” *The Journal of the Acoustical Society of America* 130 (5): 3059–67. https://doi.org/10.1121/1.3646905.

Tyler, William J., Yusuf Tufail, Michael Finsterwald, Monica L. Tauchmann, Emily J. Olson, and Cassondra Majestic. 2008. “Remote Excitation of Neuronal Circuits Using Low-Intensity, Low-Frequency Ultrasound.” *PLOS ONE* 3 (10): e3511. https://doi.org/10.1371/journal.pone.0003511.

Ungi, Tamas, Andras Lasso, and Gabor Fichtinger. 2016. “Open-Source Platforms for Navigated Image-Guided Interventions.” *Medical Image Analysis*, 20th anniversary of the Medical Image Analysis journal (MedIA), 33 (October): 181–86. https://doi.org/10.1016/j.media.2016.06.011.

VanBaren, P., J.-U. Kluiwstra, R. Seip, Y. Zhang, E.S. Ebbini, and C.A. Cain. 1995. “2D Large Aperture Ultrasound Phased Arrays for Hyperthermia Cancer Therapy: Design, Fabrication and Experimental Results.” In *1995 IEEE Ultrasonics Symposium. Proceedings. An International Symposium*, 2:1269–72 vol.2. https://doi.org/10.1109/ULTSYM.1995.495788.

Vernet, Marine, Romain Quentin, Lorena Chanes, Andres Mitsumasu, and Antoni Valero-Cabré. 2014. “Frontal Eye Field, Where Art Thou? Anatomy, Function, and Non-Invasive Manipulation of

Frontal Regions Involved in Eye Movements and Associated Cognitive Operations." *Frontiers in Integrative Neuroscience* 8. https://www.frontiersin.org/article/10.3389/fnint.2014.00066.

Vlaisavljevich, Eli, Yohan Kim, Steven Allen, Gabe Owens, Shawn Pelletier, Charles Cain, Kimberly Ives, and Zhen Xu. 2013. "Image-Guided Non-Invasive Ultrasound Liver Ablation Using Histotripsy: Feasibility Study in an In Vivo Porcine Model." *Ultrasound in Medicine & Biology* 39 (8): 1398–1409. https://doi.org/10.1016/j.ultrasmedbio.2013.02.005.

Volkow, Nora, Helene Benveniste, and A. Thomas McLellan. 2018. "Use and Misuse of Opioids in Chronic Pain." *Annual Review of Medicine* 69 (1): 451–65. https://doi.org/10.1146/annurev-med-011817-044739.

Vyas, Urvi, and Douglas Christensen. 2012. "Ultrasound Beam Simulations in Inhomogeneous Tissue Geometries Using the Hybrid Angular Spectrum Method." *IEEE Transactions on Ultrasonics, Ferroelectrics, and Frequency Control* 59 (6): 1093–1100. https://doi.org/10.1109/TUFFC.2012.2300.

Vykhodtseva, NI, K Hynynen, and C Damianou. 1995. "Histologic Effects of High Intensity Pulsed Ultrasound Exposure with Subharmonic Emission in Rabbit Brain in Vivo." *Ultrasound in Medicine & Biology* 21 (7): 969–79.

Walsh, Vincent, and Alan Cowey. 2000. "Transcranial Magnetic Stimulation and Cognitive Neuroscience." *Nature Reviews Neuroscience* 1 (1): 73–80.

Waterbeemd, Han van de, Gian Camenisch, Gerd Folkers, Jacques R. Chretien, and Oleg A. Raevsky. 1998. "Estimation of Blood-Brain Barrier Crossing of Drugs Using Molecular Size and Shape, and H-Bonding Descriptors." *Journal of Drug Targeting* 6 (2): 151–65. https://doi.org/10.3109/10611869808997889.

Wattiez, Nicolas, Charlotte Constans, Thomas Deffieux, Pierre M. Daye, Mickael Tanter, Jean-François Aubry, and Pierre Pouget. 2017. "Transcranial Ultrasonic Stimulation Modulates Single-Neuron Discharge in Macaques Performing an Antisaccade Task." *Brain Stimulation* 10 (6): 1024–31. https://doi.org/10.1016/j.brs.2017.07.007.

Wei, K-C, H-C Tsai, Y-J Lu, H-W Yang, M-Y Hua, M-F Wu, P-Y Chen, C-Y Huang, T-C Yen, and H-L Liu. 2013. "Neuronavigation-Guided Focused Ultrasound-Induced Blood-Brain Barrier Opening: A Preliminary Study in Swine." *American Journal of Neuroradiology* 34 (1): 115–20.

Wells, Jonathon, Chris Kao, Peter Konrad, Tom Milner, Jihoon Kim, Anita Mahadevan-Jansen, and E. Duco Jansen. 2007. "Biophysical Mechanisms of Transient Optical Stimulation of Peripheral Nerve." *Biophysical Journal* 93 (7): 2567–80. https://doi.org/10.1529/biophysj.107.104786.

Wells, P.N.T. 1975. "Absorption and Dispersion of Ultrasound in Biological Tissue." *Ultrasound in Medicine & Biology* 1 (4): 369–76. https://doi.org/10.1016/0301-5629(75)90124-6.

White, P. J., G. T. Clement, and K. Hynynen. 2006. "Longitudinal and Shear Mode Ultrasound Propagation in Human Skull Bone." *Ultrasound in Medicine & Biology* 32 (7): 1085–96. https://doi.org/10.1016/j.ultrasmedbio.2006.03.015.

Wilm, Mikaël, Sylvain Ballandras, Vincent Laude, and Thomas Pastureaud. 2002. "A Full 3D Plane-Wave-Expansion Model for 1-3 Piezoelectric Composite Structures." *The Journal of the Acoustical Society of America* 112 (3): 943–52. https://doi.org/10.1121/1.1496081.

Worlikar, Tejaswi, Eli Vlaisavljevich, Tyler Gerhardson, Joan Greve, Shanshan Wan, Sibu Kuruvilla, Jonathan Lundt, et al. 2018. "Histotripsy for Non-Invasive Ablation of Hepatocellular Carcinoma (HCC) Tumor in a Subcutaneous Xenograft Murine Model." In *2018 40th Annual International Conference of the IEEE Engineering in Medicine and Biology Society (EMBC)*, 6064–67. https://doi.org/10.1109/EMBC.2018.8513650.

Wu, FENG, ZHI-BIAO Wang, WEN-ZHI Chen, JIN Bai, HUI Zhu, and TIAN-YU Qiao. 2003. "Preliminary Experience Using High Intensity Focused Ultrasound for the Treatment of Patients With

Advanced Stage Renal Malignancy." *The Journal of Urology*, Part 1 of 2, 170 (6, Part 1): 2237–40. https://doi.org/10.1097/01.ju.0000097123.34790.70.

Wu, Shih-Ying, Christian Aurup, Carlos Sierra Sanchez, Julien Grondin, Wenlan Zheng, Hermes Kamimura, Vincent P. Ferrera, and Elisa E. Konofagou. 2018. "Efficient Blood-Brain Barrier Opening in Primates with Neuronavigation-Guided Ultrasound and Real-Time Acoustic Mapping." *Scientific Reports* 8 (1): 7978. https://doi.org/10.1038/s41598-018-25904-9.

Wu, Shih-Ying, Yao-Sheng Tung, Fabrice Marquet, Matthew Eric Downs, Carlos Sierra Sanchez, Cherry Chen Chen, Vincent Ferrera, and Elisa Konofagou. 2014. "Transcranial Cavitation Detection in Primates during Blood-Brain Barrier Opening-a Performance Assessment Study." *IEEE Transactions on Ultrasonics, Ferroelectrics, and Frequency Control* 61 (6): 966–78. https://doi.org/10.1109/TUFFC.2014.2992.

Yang, Feng-Yi, Tai-Tong Wong, Ming-Che Teng, Ren-Shyan Liu, Maggie Lu, Hsiang-Fa Liang, and Ming-Cheng Wei. 2012. "Focused Ultrasound and Interleukin-4 Receptor-Targeted Liposomal Doxorubicin for Enhanced Targeted Drug Delivery and Antitumor Effect in Glioblastoma Multiforme." *Journal of Controlled Release* 160 (3): 652–58. https://doi.org/10.1016/j.jconrel.2012.02.023.

Yang, Pai-Feng, M. Anthony Phipps, Allen T. Newton, Vandiver Chaplin, John C. Gore, Charles F. Caskey, and Li Min Chen. 2018. "Neuromodulation of Sensory Networks in Monkey Brain by Focused Ultrasound with MRI Guidance and Detection." *Scientific Reports* 8 (1): 7993. https://doi.org/10.1038/s41598-018-26287-7.

Ye, Patrick Peiyong, Julian R. Brown, and Kim Butts Pauly. 2016. "Frequency Dependence of Ultrasound Neurostimulation in the Mouse Brain." *Ultrasound in Medicine & Biology* 42 (7): 1512–30. https://doi.org/10.1016/j.ultrasmedbio.2016.02.012.

Yoo, Sangjin, David R. Mittelstein, Robert C. Hurt, Jerome Lacroix, and Mikhail G. Shapiro. 2022. "Focused Ultrasound Excites Cortical Neurons via Mechanosensitive Calcium Accumulation and Ion Channel Amplification." *Nature Communications* 13 (1): 493. https://doi.org/10.1038/s41467-022-28040-1.

Yoo, Seung-Schik, Alexander Bystritsky, Jong-Hwan Lee, Yongzhi Zhang, Krisztina Fischer, Byoung-Kyong Min, Nathan J. McDannold, Alvaro Pascual-Leone, and Ferenc A. Jolesz. 2011. "Focused Ultrasound Modulates Region-Specific Brain Activity." *NeuroImage* 56 (3): 1267–75. https://doi.org/10.1016/j.neuroimage.2011.02.058.

Yoon, Kyungho, Wonhye Lee, Ji Eun Lee, Linda Xu, Phillip Croce, Lori Foley, and Seung-Schik Yoo. 2019. "Effects of Sonication Parameters on Transcranial Focused Ultrasound Brain Stimulation in an Ovine Model." Edited by Robert Chen. *PLOS ONE* 14 (10): e0224311. https://doi.org/10.1371/journal.pone.0224311.

Yu, Kai, Xiaodan Niu, Esther Krook-Magnuson, and Bin He. 2021. "Intrinsic Functional Neuron-Type Selectivity of Transcranial Focused Ultrasound Neuromodulation." *Nature Communications* 12 (1): 2519. https://doi.org/10.1038/s41467-021-22743-7.

Zhang, Y., M. Brady, and S. Smith. 2001. "Segmentation of Brain MR Images through a Hidden Markov Random Field Model and the Expectation-Maximization Algorithm." *IEEE Transactions on Medical Imaging* 20 (1): 45–57. https://doi.org/10.1109/42.906424.

Zhou, Hui, Yang Liu, Xiaojing Long, Yangzi Qiao, Jo Lee, Xin Liu, Hairong Zheng, and Chao Zou. 2021. "MR-Guided Blood-Brain Barrier Opening Induced by Rapid Short-Pulse Ultrasound in Non-Human Primates." *Quantitative Imaging in Medicine and Surgery* 11 (6): 2415–27. https://doi.org/10.21037/qims-20-1047.

Zhou, Hui, Yang Liu, Xiaojing Long, Yangzi Qiao, Jo Lee, Hao Peng, Xin Liu, Chao Zou, and Hairong Zheng. 2022. "Feasibility of Ultrasound-Induced Blood-Brain Barrier Disruption with a Single-Element Transducer under Three Different Frequencies in Two Non-Human Primates in Vivo: Case

Report.” *Journal of Neuroscience Methods* 365 (January): 109383. https://doi.org/10.1016/j.jneumeth.2021.109383.